LOW COST SOLUTION-BASED MATERIALS PROCESSING METHODS FOR LARGE AREA OLEDs AND OFETs

by

Jonghwa Jeong

A dissertation submitted to the faculty of
The University of Utah
in partial fulfillment of the requirements for the degree of

Doctor of Philosophy

Department of Materials Science and Engineering
The University of Utah
May 2012

The University of Utah Graduate School

STATEMENT OF DISSERTATION APPROVAL

The dissertation of **Jonghwa Jeong**

has been approved by the following supervisory committee members:

Steven M. Blair, Chair	3/7/12	Date Approved
Feng Liu, Member	3/7/12	Date Approved
Anil V. Virkar, Member	3/15/12	Date Approved
Valy Vardeny, Member	3/7/12	Date Approved
Agnes Ostafin, Member	3/7/12	Date Approved

and by **Steven M. Blair**, Chair of

the Department of **Electrical and Computer Engineering**

and by Charles A. Wight, Dean of The Graduate School.

ABSTRACT

In Part 1, we demonstrate the fabrication of organic light-emitting devices (OLEDs) with precisely patterned pixels by the spin-casting of Alq3 and rubrene thin films with dimensions as small as 10 μm. The solution-based patterning technique produces pixels via the segregation of organic molecules into microfabricated channels or wells. Segregation is controlled by a combination of weak adsorbing characteristics of aliphatic terminated self-assembled monolayers (SAMs) and by centrifugal force, which directs the organic solution into the channel or well. This novel patterning technique may resolve the limitations of pixel resolution in the method of thermal evaporation using shadow masks, and is applicable to the fabrication of large area displays. Furthermore, the patterning technique has the potential to produce pixel sizes down to the limitation of photolithography and micromachining techniques, thereby enabling the fabrication of high-resolution microdisplays. The patterned OLEDs, based upon a confined structure with low refractive index of SiO_2, exhibited higher current density than an unpatterned OLED, which results in higher electroluminescence intensity and eventually more efficient device operation at low applied voltages. We discuss the patterning method and device fabrication, and characterize the morphological, optical, and electrical properties of the organic pixels.

In part 2, we demonstrate a new growth technique for organic single crystals based on solvent vapor assisted recrystallization. We show that, by controlling the polarity of the solvent vapor and the exposure time in a closed system, we obtain rubrene in orthorhombic to monoclinic crystal structures. This novel technique for growing single crystals can induce phase shifting and alteration of crystal structure and lattice parameters. The organic molecules showed structural change from orthorhombic to monoclinic, which also provided additional optical transition of hypsochromic shift from that of the

orthorhombic form. An intermediate form of the crystal exhibits an optical transition to the lowest vibrational energy level that is otherwise disallowed in the single-crystal orthorhombic form. The monoclinic form exhibits entirely new optical transitions and showed a possible structural rearrangement for increasing charge carrier mobility, making it promising for organic devices. These phenomena can be explained and proved by the chemical structure and molecular packing of the monoclinic form, transformed from orthorhombic crystalline structure.

To

My fiancee and parents, who made all this possible

TABLE OF CONTENTS

LIST OF FIGURES

ACKNOWLEDGEMENTS

Many people have assisted and supported me along this long journey, and I think I could not have finished my final thesis without their generous help. Firstly, I have to mention that it is great luck to work with my advisor, Dr.Steven M. Blair. He gave me good support and guidance whenever I have met an obstacle in my research.

Also, the entire job would not have been completed if it were not for the guidance of my committee members: Dr.Feng Liu, Dr.Anil V. Virkar, Dr.Valy Vardeny, and Dr.Agnes Ostafin.

I would like to thank to our Photonics research group members (Jeremy, Xiaojin, Mohit), Microfab staff (Brian, Paul, Tonny), Opto-electronics Lab. members (Yang, Fujiang), Dixon laser institute members (Randy), Materials characterization lab Members (David).

I sincerely appreciate my friends, Hanwelm, Oleg, Xiaojin, Jeremy, Ashley and special thanks to Sarang. They always helped me my research and offered countless favors as a friend and fellow worker whenever I felt a hardship in my life and research.

I also appreciate the support of National Science Foundation (NSF) and Corning Inc. for my research.

Most of all, I would like to mention my parents, Jaeboon and Hanho Jeong, who made me what I am. Even though they were far away, they always took care of me and encouraged my getting over difficulties.

CHAPTER 1

INTRODUCTION

1.1 Overview

The basic outline of this chapter is as follows. In part 1, the motivation, hypothesis, and specific aims are presented. This research employs a novel solution-based patterning technique to fabricate high resolution organic light emitting devices (OLEDs). In the background section, both the fundamental theory of OLEDs and advanced processing methods for patterning OLED pixels are discussed. In the experimental section, the device design, fabrication, and experimental methods are presented. The novel patterning technique and device fabrication will be described in detail in the experimental section. In the result and discussion section, the optoelectric performance of the OLEDs is discussed. The result will be summarized and future work to improve device performance using this technique is discussed.

The basic outline of part 2 is as follows. In part 2, the motivation, hypothesis, and specific aims to pursue this study are presented. This research employs a novel solvent vapor assisted recyrstallization technique to grow single crystal for application of organic semiconductor devices. In the background section, both the fundamental theory of single crystal of organic semiconductor and organic field effect transistors (OFETs) are discussed. In the experimental section, sample preparation, crystallization, and characterization methods are presented. This solvent vapor recrystallization technique

and its characterization proving crystalline structure will be described in detail in the experimental section. In the results and discussion section, the optoelectronic performances of single crystal are discussed. The result will be summarized and future work to understand physical mechanisms and improve device performance using this technique is discussed.

1.2 Motivation

Recent progress in organic electronics open new perspectives as an alternative to traditional inorganic based semiconductor devices. Organic materials have been studied widely to develop the materials into active electronic and optoelectronic devices, including light emitting diodes (OLED),[1] lasers,[2] photodetectors,[3] optical modulators[4], and field effect transistors (OFET).[5]

1.2.1 High Resolution Patterning for Organic Light Emitting Devices

The market for flat panel displays has grown dramatically, due primarily to their demand in portable electronic devices and large displays, reaching $130 billion in 2009, and the flat panel display market is predicted to increase to over $137 billion by 2012 (Figure 1.1).[6] Presently, the dominant display technology is liquid crystal (LCD). However, organic light emitting devices (OLEDs) promise to be a new generation in the flat panel display market since organic displays can be fabricated on flexible substrates and hold the potential for reduced manufacturing cost, positioning them to be the dominant alternative to LCDs and conventional lighting devices. In addition, OLEDs have advantages over LCDs such as wider viewing angles, better emission quality, higher color contrast, and lower power consumption.[7]

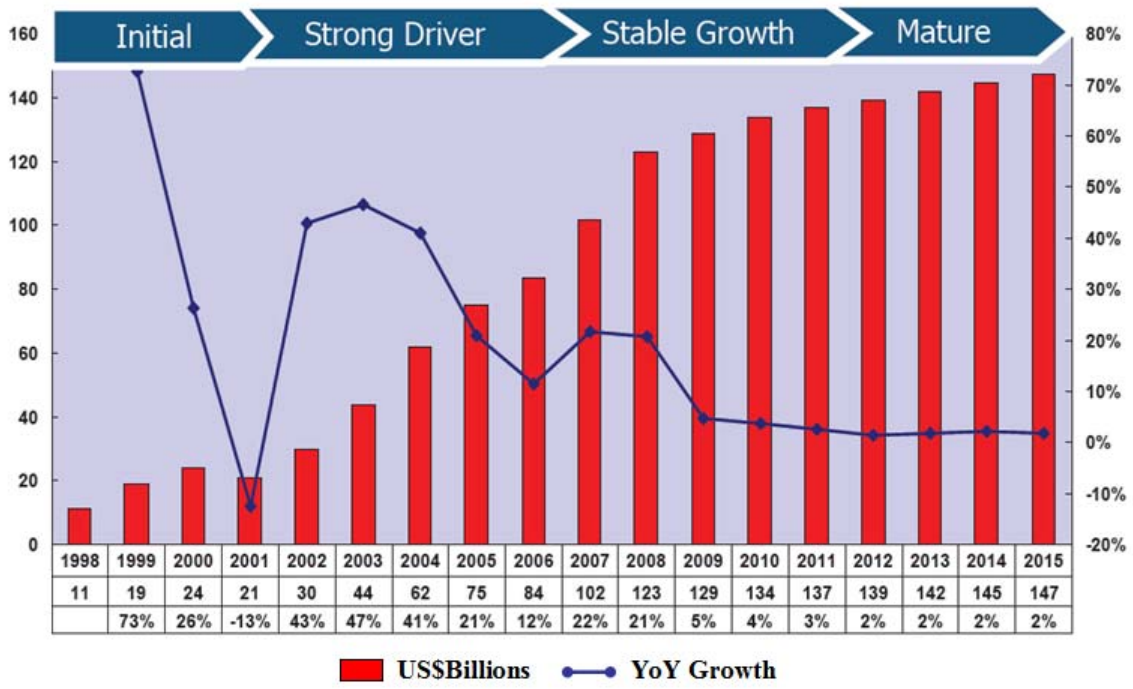

Figure 1.1. Outlook of the overall flat panel display market.[6]

Alternatively, OLEDs are attractive as low cost alternatives for numerous applications, including full color displays and microdisplays.[8] The revenue of OLED is expected to increase to up to three billion dollars by 2012. The main applications of OLEDs are portable devices including portable multimedia players (PMPs) and mobile phones. Figure 1.2 shows that demands of PDPs and mobile phones are gradually increasing and occupying a large portion of the display market. This chart also interestingly indicates that there is an increasing demand for microdisplays (subdisplay near the eye) even though that portion of the market is smaller than for portable devices.[6] OLEDs promise to usher in a new generation of high resolution micro- and nanodisplays since they operate with high efficiency at low drive voltage, and theoretically the maximum electroluminescence (EL) efficiency may exceed over 15%. One of the major concerns in the field of flat panel OLEDs is the precise patterning of high -

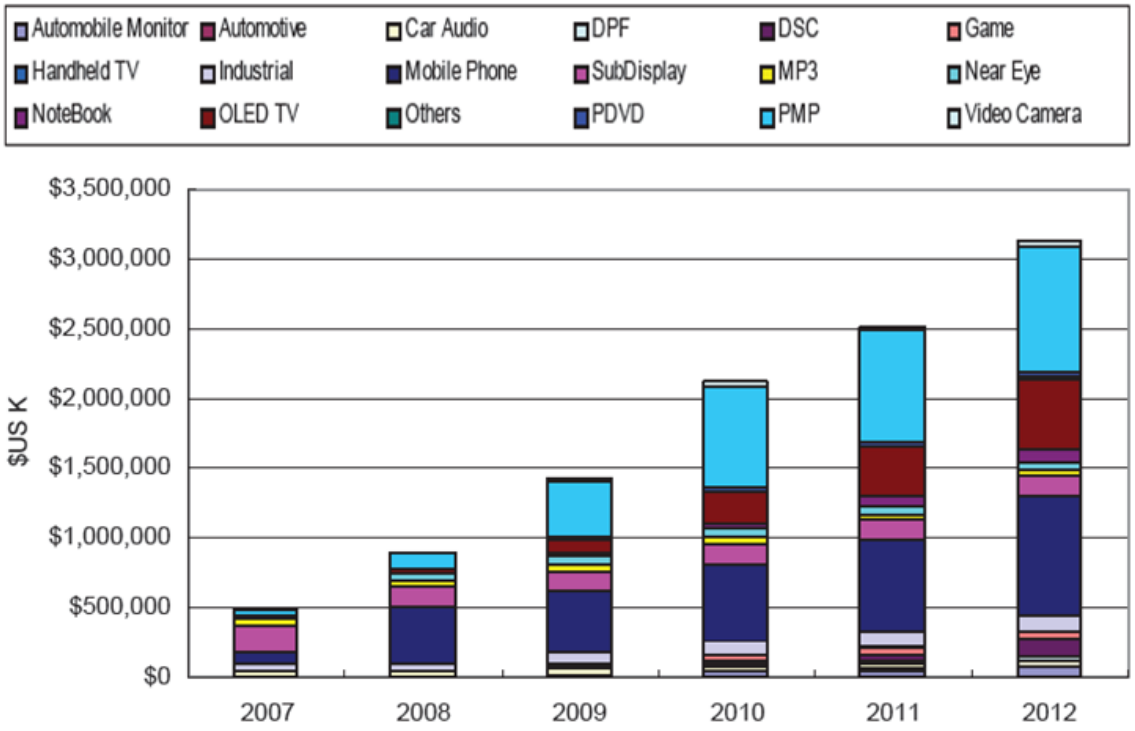

Figure 1.2. Outlook of OLEDs in applications for flat panel displays.[6]

resolution pixelated displays with the retention of optimal materials properties.[9] Accordingly, the development of low cost and large area patterning techniques with high resolution is desired.

1.2.2 Properties of Organic Single Crystal for Optoelectronic Devices

In particular, OFETs are being pursued as low cost alternatives for numerous electronic applications such as digital circuits, RFID, and flat panel displays due to their unique advantages such as large area coverage, structural flexibility, low temperature processing, and potentially low fabrication cost. The silicon chip requires the use of complex and expensive processes (e.g., photolithography and vacuum deposition) that are often carried out at high temperatures, must be performed in an ultraclean environment,

and are limited in size to 12 inch silicon wafers. Although the performance of the organic transistor is much inferior to inorganic transistor, the OFET can be properly operated on switching devices for active matrix flat panel displays (AMFPDs), active matrix organic light emitting devices (AMOLEDs) ,[10] electronic paper displays,[11] field effect type sensors,[12] low end smart cards, and radio frequency identification tags (RFIDs)[13] and these advantages are unimaginable to attain with inorganic semiconductor materials.

OFETs require a high charge carrier mobility which determines how fast RGB pixels turn on and off, which can reduce the after image in display operations.[14] The most important property of thin film transistor (TFT) is charge carrier transport among organic semiconductor molecules since this current flow between source and drain electrodes is modulated by charge carrier accumulation at the semiconductor/insulator interface resulting from an applied gate voltage. Therefore, pure crystallinity is a decisive factor in the performance of OFET devices since crystalline structure eliminates grain boundaries and the concentration of charge traps in the device with impurities.[15] However, presently, OFETs operate at low switching rates due to the low charge carrier mobility in organic materials, which is primarily caused by poor molecular ordering.

Due to their high solubility in volatile solvents, conjugated polymer films can be deposited at room temperature by simple solution-based methods such as drop or spin casting. Further, direct printing techniques, such as inkjet or imprinting, can be used to create pixelated devices. By contrast, small molecule semiconductors (e.g., Alq3 and polycyclic aromatic hydrocarbons such as pentacene, anthracene, and rubrene) are deposited by thermal evaporation through shadow masks, which results in a polycrystalline thin film.[16] High purity single crystalline rubrene, for example, is prepared by a physical vapor transport technique (PVT).[17] Even though this technique

can produce large bulk crystals and can be adapted for arrayed devices, mobility is relatively low.[18] Nevertheless, small molecules generally exhibit better optoelectronic performance in devices; therefore, solution-based crystallization and patterning techniques enabling direct placement of small molecule single crystals onto a specified position are desirable.

As one possible approach, some organic semiconductor materials transform from amorphous thin films into crystalline structures upon solvent vapor annealing. A tetrathiafulvalene (TTF) single crystal OFET was fabricated directly on the channel between source and drain from saturated solution,[19] but the crystal structure is not controllable. Solvent vapor annealing has also been used to improve the electrical properties of solution processable triethylsilylethynyl anthradithiophene (TESADT). Solvent annealing transformed the amorphous film into a large grain polycrystalline structure, which improved mobility.[20]

The motivation for this research is building high performance organic field effect transistors (OFETs). The structural phase shifting drives the rubrene crystal to improve charge carrier mobility. We demonstrate a novel crystal growing technique via the solvent vapor recrystallization (SVR) technique. The SVR technique takes advantage of the tendency of amorphous organic semiconductor thin films to crystallize during exposure to solvent vapor. While we have achieved growth of Alq3 and rubrene crystals at room temperature on silicon substrates, we focus our attention on rubrene, which undergoes dramatic structural variation (from the common orthorhombic to the monoclinic form) leading to new blue-shifted optical transitions and improved charge carrier mobility. We discuss the interfacial interactions between solvent vapor polarity and the organic semiconductor, which cause crystallization and phase change.

1.3 Background

1.3.1 Advantages of OLEDs

Recently, society has expressed large demand for portable devices and flat panel displays. The main factors to evaluate the display performances are light weight (slim design), natural color generation, flexibility with high brightness, contrast, and resolution with wide viewing angle, and fast pixel responses with low power consumption and low manufacturing cost. The advantages of OLED compared to LCD in display performance are listed in Table 1.1. Currently, LCD and LED flat panel displays dominate the display market, but the need for OLED is gradually increasing.

We can categorize the two main display types by the need for an external light source. LCDs require back lighting to illuminate display pixels, but LED and OLED function without an external light source because these devices serve as intrinsically -

Table 1.1. Advantages of OLED display performance compared to LCD[21]

	advantages
slim	• No backlight • Enough space for additional device and battery capacity • Remove malfunction of thinner display
natural	• Self-light-emitting material → produce multiple and 100 % true color • Low energy consumption and long lifetime • Sufficient brightness for operation in bright environments
free	• 360° viewing at all angles with clear and true color • No change of brightness, contrast, and color at all angles
fast	• Fast display speed (limited only by speed of light) • No afterimage • No eye fatigue

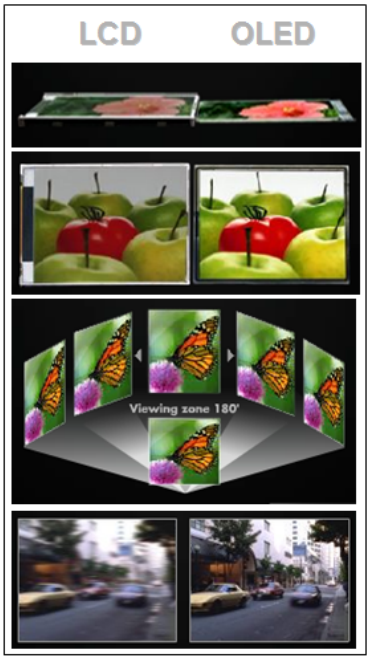

emissive pixels. The LCD is mainly used for its advantages of low power consumption and thin display structure. However, LCDs have poor viewing angle and offer non-reliable color performance, and are relatively expensive to manufacture.

1.3.2 Fundamental Operation of Organic Light Emitting Devices

Figure 1.3 describes the fundamental operation of LCD and OLED displays. LCDs utilize the properties of liquid crystals, which lie in an intermediate state between disordered form in a liquid and the ordered form of a solid crystalline. The LCD operates with the liquid crystal modulating the polarization angle of the back light.

The OLED operates by organic electroluminescence (EL), which is electrically driven emission of light from luminescent organic semiconductor materials. The simplest OLED device is basically composed of two active layers, a hole transport -

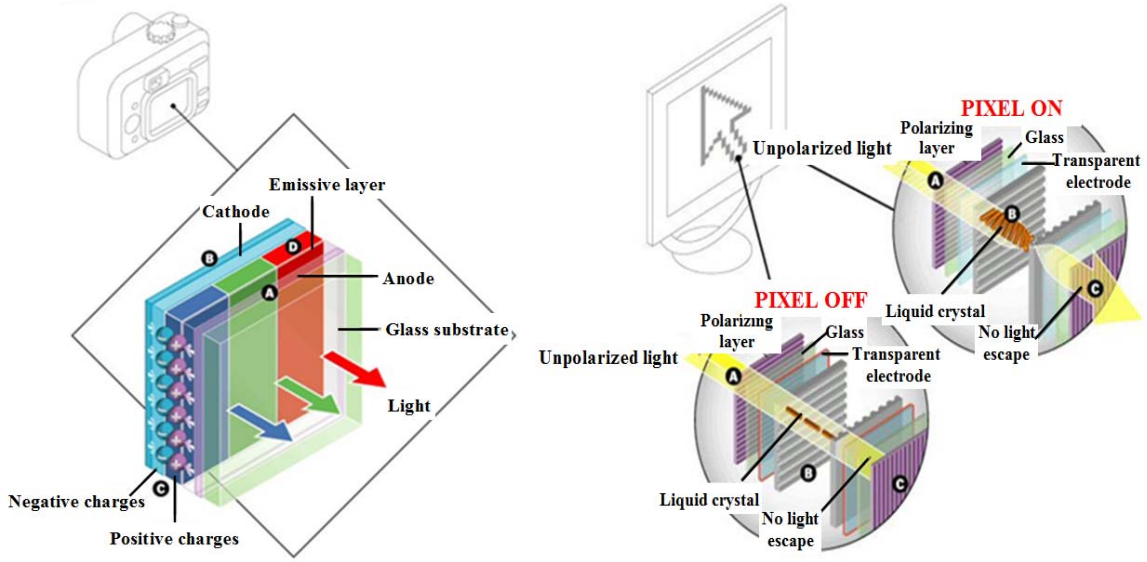

Figure 1.3. Schematics of the device structures of OLED (left) and LCD (right) displays.[22]

layer (HTL) and an electron transport layer (ETL), sandwiched between a high work function anode to inject holes into the HTL and a low work function cathode to inject electrons into the ETL as illustrated in Figure 1.4 (left). The inorganic LED is composed of a simple p- and n-type junction structure, comparative to the organic LED in Figure 1.4 (right). Even though inorganic LEDs and organic LEDs have similar structures, the fundamental behaviors of inorganic and organic LEDs are actually quite different in electronic and optical properties. These main differences originate from carrier injection (space charge limited current) and molecular excitons.

In the fundamental OLED mechanism, the energy band reaches the equilibrium state when the p- (HTL) and n- (ETL) type materials are combined. In the basic operation of the OLED, electrons are injected from the cathode (low work function metal) and holes from the anode (high work function metal) when an electrical potential difference is applied across the device. The energy bands of HTL and ETL are lowered by applying forward bias so that electrons and holes can transport through the layers. The carriers are transported into the desired luminescent layer (electron transport layer, ETL in Figure 1.5). This design of the hetero-junction OLED is based on light emission from the electron transport layer. Thus the electrons are blocked by the higher energy barrier of the HTL, but holes easily reach the ETL via the lower energy barrier. After forming excitons to lower the energy, the holes and electrons recombine to generate light via photon emission.

OLED performance can be improved by adding an additional hole injection layer (HIL) and/or an electron injection layer (EIL), which makes better quantum efficiency.

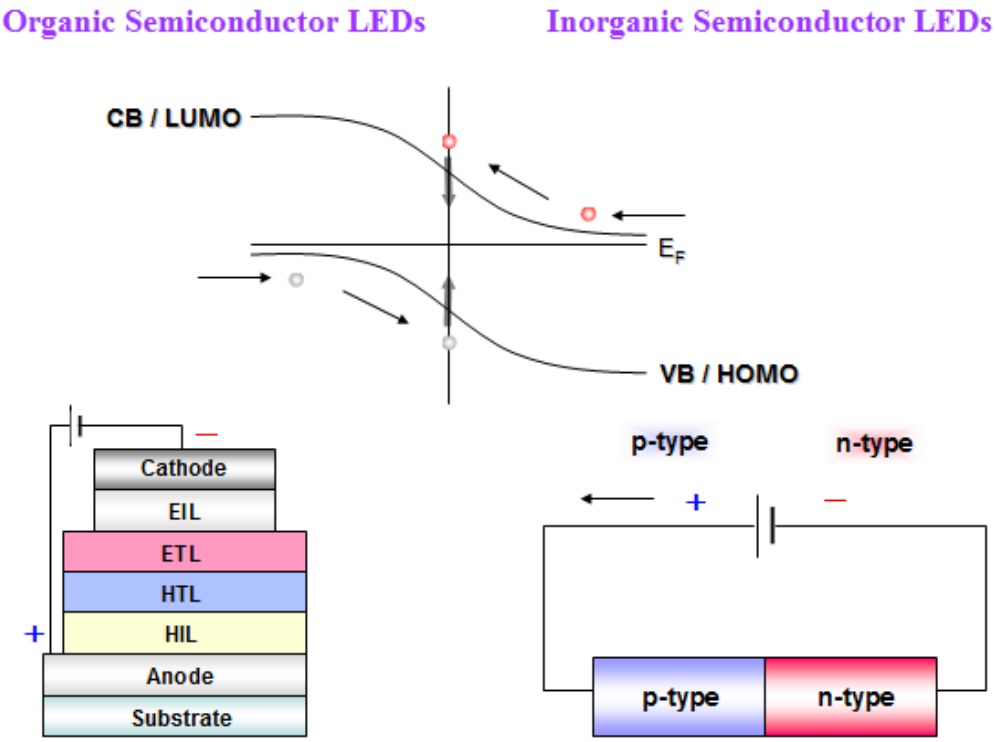

Figure 1.4. Schematics of energy band and device structure: OLED vs. Inorganic LED.

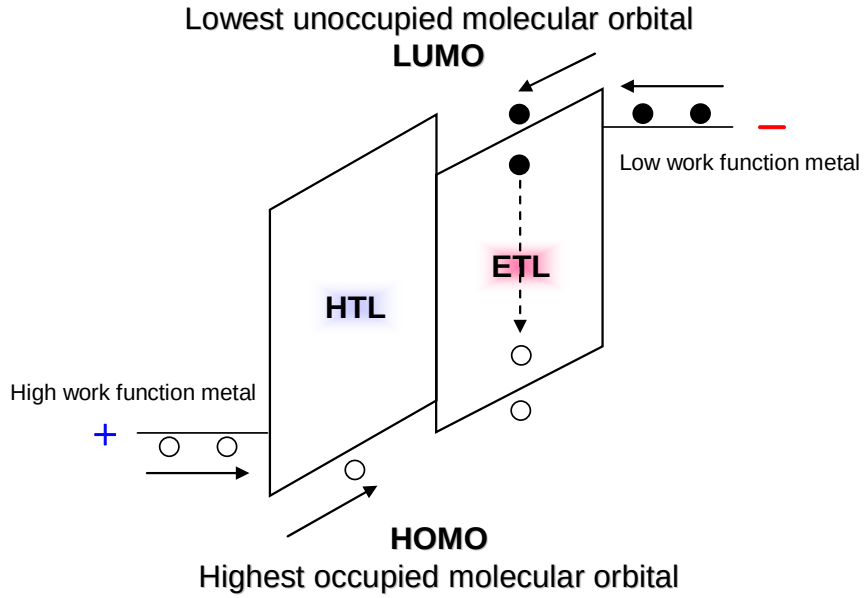

Figure 1.5. Typical thin film organic light emitting device (OLED) structure and energy diagram.[23]

The luminescent layer can be either the ETL or HTL according to the design of the energy levels. The organic materials are chosen by considering their properties of mobility and bandgap.

1.3.3. Design of High Performance OLED Structure

The basic of design of the multilayer OLED is based on the confinement of charge carriers within the electroluminescent layer through balanced carrier injection and transport. High performance OLEDs mostly are composed of several organic layers and carrier recombination occurs at ETL since the ETL has the ability to accept hole injection from the HTL due to the lower energy band. The multilayer can consist of a blocking layer of unipolar HTL or ETL. The unipolar layers block the passage of hole or electron carriers which eventually result in increased carrier recombination probability. The recombination occurs near the HTL/ETL interface and the recombination is restricted in a very narrow region, less than 10 nm. Moreover, efficient design of the multilayer can keep the energy of molecular excitons from dissipating into the metal electrodes; excitons within 20 nm of a metal electrode can decay nonradiatively into the metal. Therefore, the thickness of HTL and ETL around 50 to 70 nm is required to prevent this quenching process.

1.3.4 Organic Light Emitting Materials and Their Requirements

In this research, three small molecule materials are used that exhibit dewetting behaviors in the presence of a hydrophobic interface, shown in Figure 1.6. N-type tris(8-hydroxyquinoline) aluminum (Alq3) is one of the main organic semiconductor -

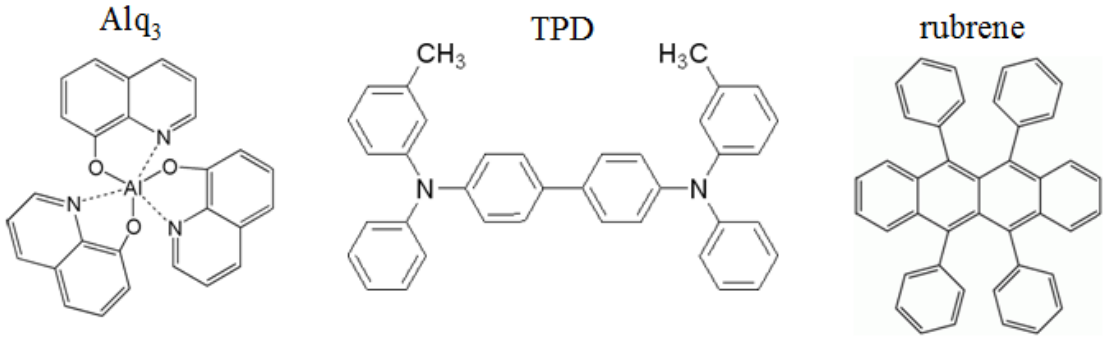

Figure 1.6. Molecular structure of the organic materials used for self-patterning organics in HTL and ETL.[24]

materials in high luminescence OLEDs, which is commonly used as the electron transport and emissive material with p-type N,N′-Bis(3-methylphenyl)-N,N′-diphenylbenzidine (TPD) as the hole transport material, yielding typical green electroluminescence around 530 nm. Alq3 is the most widely used electron transport and host emitting material in OLED applications since the molecule is thermally and chemically stable and can be evaporated on a substrate as a uniform thin film. Also, this molecule can be easily synthesized and purified, and the molecular structure prefers to avoid exciplex formation. The electron mobility of Alq3 strongly depends on electric field with a value of approximately 10^{-6} $cm^2/(V\ s)$ at 4×10^5 V/cm. The emission light can be tuned by doping a small amount of specific guest molecules in Alq3 or by choosing different organic fluorescent materials as emitters.

5,6,11,12-tetraphenylnaphthacene (rubrene) is a yellow light emitting p-type organic semiconductor material with wavelength 560 nm. Rubrene has been used as an electroluminescent, hole transport layer and as a dopant material, which means that rubrene can function as host, transport, or dopant material in OLEDs.[25]

The emission of rubrene can be tuned to the red with dopants. Rubrene is also used in white OLEDs (WOLEDs) as a chromaticity tuning layer in hetero junction interfaces.[26] Rubrene has been used as a dopant and emitting assist dopant in Alq3[27] electron transport layers to improve operating efficiency (low propagation loss, luminance efficiency, and power efficiency) and to tune the color by controlling rubrene concentration, and in NPB[28] and TPD[29] hole transport layers.

Besides precise patterning, uniform film deposition is required over large areas and the organic materials must function properly in the display. Organic materials have to conserve their uniform amorphous state during the fabrication process since the performance of organic thin film devices strongly depends on the morphological and structural properties of the film, affecting color purity, device efficiency, and device lifetime.[30] OLEDs require balanced electron and hole current transport to generate efficient electroluminescence. Electron transport materials (e.g., Alq3) are chemically and environmentally sensitive to their processing and operating conditions. Humidity during processing also can cause crystallization of molecules.[31] Any morphological transformation such as cluster formation or crystallization with overlap of π-molecular orbitals, which promotes formation of excimers or ground state complexes which negatively impacts OLED function in that the emission light is red-shifted and quantum efficiency decreases due to an increase of nonradiative recombination pathways, eventually resulting in failure of the OLED.[32] Therefore, proper fabrication techniques and materials properties will be necessary to minimize imperfections so as to achieve effectively functioning devices.[33]

1.3.5 Patterning and Deposition Methods

1.3.5.1 Dry Processing

Deposition and patterning of organic semiconductors are performed by either dry processing or wet processing methods. Organic small molecules are most often deposited by thermal evaporation (thermal vacuum evaporation) in a vacuum of ~10^{6} torr through shadow masks, offering the advantages of source purity, ease of thickness control, and multiple layer deposition (Figure 1.7, left).[34] However, shadow masking limits the patterning resolution and precision because of the difficulty in making small features (e.g., 50 μm) and in aligning the shadow mask (tolerance of ~5 μm).[35] The polymer and small molecules can be patterned by thermal imaging dry transfer technique, also called laser induced thermal imaging (LITI), which utilizes ablation of materials of active organic semiconductor materials with using localized heat source forming pixel (Figure 1.7, right).[36]

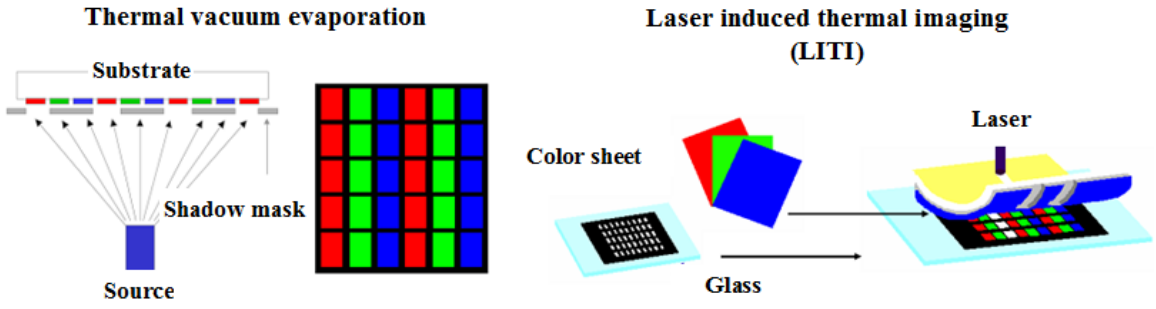

Figure 1.7. Dry processing: Thermal vacuum evaporation (Left), Laser induced thermal imaging (LITI), (Right).[37]

1.3.5.2 Wet Processing

Wet processing techniques enable the organic electronic devices to be fabricated in a simple process at low cost. Solution based spin-on or spray-on techniques are commonly used to deposit polymer films due to their high solubility in various solvents; the long polymer chains facilitate uniform film formation across the entire substrate.

Recent advances in film deposition and patterning techniques have enabled the fabrication of micro-OLEDs with fine pixel sizes. Micropixels are commonly prepared by patterning the anode or cathode using photolithography, and blocking the electrode contacting area with insulating materials. Organic small molecules can also be deposited with solution-based techniques if the small molecule is soluble in an organic solvent. Techniques such as an ink-jet printing,[38] roll to roll processing,[39] or screen printing[40] have been demonstrated, but these techniques have limited resolution due to large droplet size and spreading of the solution (Figure 1.8).

For smaller pixels (submicrons), electron beam lithography (EBL) has been used to produce submicron patterning, with the smallest nanoscale OLED of 60 nm based on silicon nitride holes. Most nanodevices are fabricated by blocking the ITO contacting -

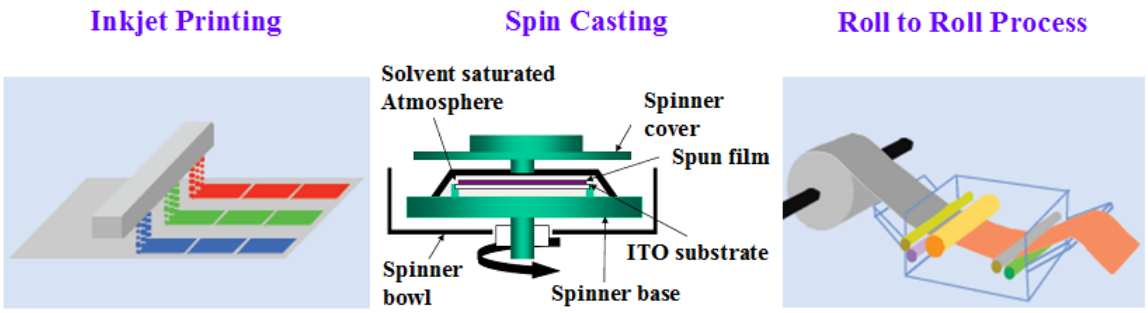

Figure 1.8. Wet processing: Inkjet printing spin casting, roll to roll process.[41]

area and depositing both the organic materials and cathode through holes in the polymer, SiO_2 or Si_3N_4 insulators.[42] A micro/nanocontact printing technique has been developed as a substitute for traditional fabrication techniques utilizing solution-processible characteristics, which is nondestructive and reversible for fragile and sensitive organic layers.[43] In spite of the advantages to high resolution patterning, these techniques are only applicable to a small area in laboratory devices.

Small molecules also can be deposited by the wet processing methods, and we have recently demonstrated the deposition of uniform amorphous films of small molecules by spin casting. Unfortunately, there is no straightforward way to pattern organic materials by spin casting. In general, small molecules exhibit better electrical and optical properties than polymers; therefore, development of solution-based patterning techniques for small molecule devices is of great interest.[44]

1.3.6 Potential Applications of High Resolution OLEDs

A potential application of the spin-on patterning technique is in microdisplays, as shown in Figure 1.9. The microdisplay can be used for personal displays such as personal glasses and military applications, which require high density of pixels. A microdisplay is defined as a display having a diagonal typically less than 1.5 inch with at least 75,000 pixel electrodes and an active area of less than 158 mm^2, placed closer than 10 inch (25.4 cm) to the eyes. Preferable array sizes are 320×240, 640×480, or higher. The desirable pixel pitch for the microdisplay is in the range of 5-30 μm, and 18 μm is possible in current industrial techniques.[45] In this research, high resolution displays are designed over an active area 6×6 mm^2. This patterning technique can make it feasible

to fit required pixel sizes in microdisplays. The higher resolution displays are more defect tolerant and viewable at close range, which allow production of microdisplays.[46]

This patterning technique is also scalable to nanodevices. For an example, in a 500 nm pixel device, the pixel density will dramatically increase up to 6.5×10^{8}/inch^2. The detailed pixel dimensions of micro- and nano-OLEDs are presented in Table 1.2. Nanoscale OLEDs can offer higher device densities per unit area, which enables the fabrication of higher resolution displays.

Figure 1.9. Potential applications of high resolution OLEDs; Microdisplays.[47]

Table 1.2. Pixel array, density, and total pixel area according to pixel sizes

Pixel size	Pixel array (μm×μm)	Pixel density (pixel NO/inch^2)	Girth/Area (μm/μm^2)	Total pixel area (μm^2)
100 μm	50×50	16,129	1/25	25,000,000
50 μm	100×100	64,516	2/25	25,000,000
10 μm	500×500	1,612,900	2/5	25,000,000
1 μm	5000×5000	161,290,000	4/1	25,000,000
500 nm	10000×10000	645,160,000	8/1	25,000,000

The nanoscale OLEDs can be used as subwavelength light sources for high resolution sensing and imaging techniques, and for nanooptical lithography.[48] Also, nanoscale devices have a potential in near field scanning optical microscopy, nanoscale assay systems, near field optical communication (quantum communication), storage devices and single photon sources for nanoscale photo-patterning.[49,50] The smallest possible light source is a single fluorescent molecule or single quantum dot (QD) turning on an individual pixel by using scanning tunneling microscope (STM)[51] or atomic force microscope (AFM)[52(c)], but this light source is not practically applicable for a device. The single light sources can be applied into quantum communication, near field scanning optical microscopy, and nanoscale photopatterning.[52] These single light sources around million molecules congregate and compose nanoscale OLEDs.

1.3.7 Organic Field Effect Transistors (OFETs)

The organic transistor can be produced by two main categories of materials such as polymers and small molecules. The polymer device can be fabricated at room temperature by using spin casting, and printing technology utilizing ink jets or printing press methods due to highly soluble characteristic in various solvents, while the small molecule device require the use of thermal evaporation using shadow mask. Well known organic semiconductor materials such as Alq3 for organic light emitting device (OLED) and pentacene for organic field effect transistor (OFET) have been deposited by thermal evaporation.[53] Even though small molecule devices have a difficulty of fabrication rather than polymer field effect transistor (PFET), the devices show higher mobility and performance than PFET. Therefore, new technology to overcome the difficulties is desired in the small molecule fabrication process because the thermal

evaporation technique not only increases fabrication cost, but also damages the fragile organic thin film layer.

The OFET can be fabricated with three main structures: top-contact, bottom contact, and top gate structures as shown in Figure 1.10. The organic field effect transistor is composed of either a molecular or polymeric channel connecting source and drain electrodes. In traditional fabrication technique, the gate is deposited on silicon or flexible substrate, followed by deposition of either organic or inorganic dielectric film, and then source and drain electrodes are thermally deposited onto organic layer or dielectric layer depending on preferable structure. The device is damaged during the traditional processing of electrode deposition and etching in the top contact OFET. The source and drain metal electrodes are regularly deposited by thermal evaporation, but this technique is not appropriate for high resolution with shadow masking and deforms the organic semiconductor layer.

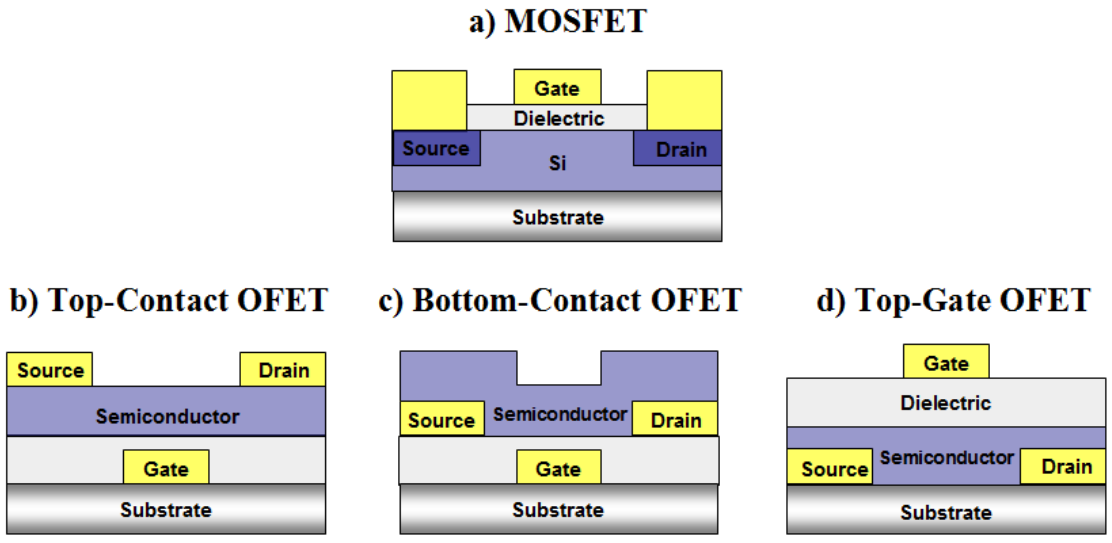

Figure 1.10. Schematics of organic field effect transistor structures: a) MOSFET, b) Top-contact OFET, c) Bottom-contact OFET, d) Top-gate OFET.

The bottom contact OFET generally yields poor device performance rather than top contact OFET in that the bottom contact OFET shows nonohmic behavior in the linear regime or low-effective mobility. The poor characteristics can be elucidated by the interrupted crystal growth at the triple interface among organic semiconductor, dielectric and source/drain electrodes.[54] The alternative way to avoid those damages is the fabrication of the top gate structure since the operation is same as other structure and the metal electrodes are deposited on the substrate. Even though the bottom contact structure possesses poorer electrical performance, the structure provides a better way to fabricate a device without any deformation.

Screen printing and inkjet printing have been introduced as an alternative to the vacuum deposition and photolithographic pattering. Screen printing has a low resolution of 100 μm, which is not applicable to pattern source and drain electrode with high resolution.[55] Inkjet printing have been developed with the resolution up to 10 μm.[56] For the higher resolution and precise patterning, microcontact printing technique has been developed as a substitute of traditional fabrication technique utilizing solution-processible characteristics.[57] Micromolding in capillaries (MIMIC) generates pattern by contacting a microchannel stamp onto a surface, which is caused by capillary force.[58] In another variation, patterned stamp is filled with a prepolymer material and then cured on the substrate to create precise patterning.[59] A nanometer size patterning can be fabricated by nanoimprint lithography (NIL), which is prepared by physical deformation of the polymer with pressing the material to a hard stamp.[60] Another technique is liquid embossing which embosses a liquid polymer layer on the surface to reproduce the recess pattern of the stamp.[61] The gold drain and source electrode have been fabricated with

patterned stamp. The stamp is used to deposit thiols as an etch resist onto gold surface and the patterns are completed by good etching.[62]

Various attempts have been made to improve the mobility of organic semiconductors and increase capacitance of suitable gate dielectrics. One approach is reduction of device dimensions such as channel length that increases current output capability and their switching speed, and the decreased channel length can increase the effective mobility by reducing the number of grain boundaries in the channel.[63] The performance of organic thin film devices strongly depends on the morphology of the thin film, which can be improved by deposition technique and fabrication technique. The traditional fabrication techniques used to produce OFET structure could cause harmful deficiencies to device performance, which deform molecular order and chemical bonding in organic semiconductor layer. Moreover, those fabrication techniques also create interfacial trapping sties and barriers to charge injection.[64] The optimal fabrication technique and conditions result in high performance of OFET. The improvement of structural and morphological defects in the thin film and development of new fabrication technique can improve performance as a device, which make possible to rival with traditional field effect transistor based on inorganic materials.[65] Thus, a nondestructive and reversible method is required to fabricate single crystal OFET to avoid processing defects.

1.3.8 Optoelectronic Properties of Organic Single Crystal

Organic semiconductors are conjugated materials bound by weak van der Waals force in which charge transport is enabled by the π-orbital overlap between neighboring molecules. The π-π interaction is therefore influenced by molecular distance and

ordering; charge carrier mobilities are typically orders of magnitude lower for amorphous and polycrystalline thin films. Charge transport efficiency is limited even in well-ordered polycrystalline films due to large grain boundaries between misoriented crystallites that impede carrier flow.[66] The detrimental effect of grain boundaries can be minimized by optimizing the thin film growth conditions and substrate surface properties. The mobilities can be improved by forming single crystal which provides good overlapping of the π-π orbital with S-S interactions and an intermolecular electronic transfer yielding their transport properties. Reduction of structural and morphological defects in thin films or single crystals through the development of new fabrication techniques may improve the performance of OFETs to rival that of traditional a-Si TFTs.[67]

Most widely used organic materials such as thiophene oligomers, polyacenes have reached to their theoretical limitation in their electronic performance and it is still unclear what influences charge carrier mobility.[68] However, it has been reported that orientation of packing molecules parallel without any defects or offset improves charge carrier transport mobility. Most potential small molecule materials for high charge carrier moblities are polyacenes and their derivatives, which are basically composed with polycyclic aromatic hydrocarbons. The crystalline structure and phase depends on chemical structure and molecular packing, which vary inter-molecular van der Waals interactions and eventually change optical and electronic properties due to extension of delocalized electrons. The crystalline transitions of polyacenes have been reported that crystalline structure changes from monoclinic to triclinic by adding phenyl rings from naphthalene to hexacene.[69] The naphthalene and anthracene[70] form monoclinc, and

tetracene[71] and pentacene[72] form triclinic. The four different structural transitions of pentacene were also observed by Matteus.[72]

CHAPTER 2

PRECISE PIXEL PATTERNING AND FABRICATION OF HIGH RESOLUTION ORGANIC LIGHT EMITTING DEVICES BY SPIN CASTING

2.1 Hypothesis and Specific Aims

The development of micro- and nanoscale patterning techniques for organic materials remains a significant research challenge. Advanced patterning techniques for submicron pixels may enable exceptional OLED performance in high resolution micro- and nanodisplays. The main research goals within this chapter are focused firstly on patterning techniques and secondly on device performance.

The purpose of this research is to implement a new pixel pattering technique for high resolution and inexpensive organic micro- and nanodisplays. Here, we invented a novel pattering technique using solution-based deposition for small molecules. Small molecules are uniformly absorbed on the entire predefined pixels by spin casing. Using these techniques, pixels can be addressed row-by-row by contacting a single patterned ITO anode line. This directed patterning technique will overcome the technical limitations of patterning high resolution pixels in current displays. Preliminary work suggests that this technique could produce submicron pixels, which would make it possible to manufacture nanodisplays in a simple patterning technique.

The goals of this research are to:

1) demonstrate deposition of uniform amorphous small molecule luminescent film by spin casting
2) study morphological and optoelectronic properties of the thin film
3) demonstrate a novel high resolution patterning technique based on the dewetting of organic materials in the presence of predefined pixel region
4) investigate the physical mechanisms of surface interactions in the dewetting system, which drive directed self-assembly of organic small molecules
5) utilize the directed self-assembly technique in the fabrication of active bottom-emitting OLED by spin-casting technique
6) study electrical efficiencies and optical confinement effects as the physical pixel sizes are reduced and confined by dielectric materials

This research follows the "Project Roadmap" shown in Figure 2.1.

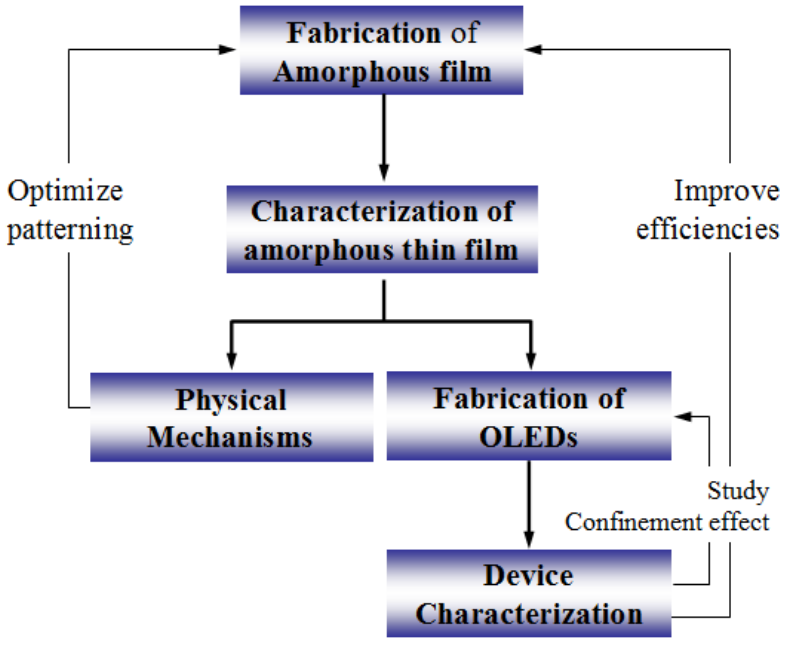

Figure 2.1. Project roadmap.

The research begins by demonstrating the formation of an amorphous small molecule thin film followed by characterizing the material properties of the thin film. The experimental results provide information regarding the physical mechanisms for forming the amorphous thin film and the properties serve as a base to evaluate device performance. This physical understanding guides the selection of optimal experimental conditions for future iterations of the device structure. Additionally, once suitable optoelectronic and morphological properties are achieved, the amorphous thin film is incorporated into the directed patterning technique to fabricate and characterize micro scale OLEDs. Following device characterization, the results may then direct further research into material properties in order to improve device efficiency by modifying the self-assembly conditions. Finally, physical, optical, and electrical confinement effects are investigated as the pixel size is reduced and confined environmentally by dielectric materials.

2.2 Experimental Procedures

2.2.1 Materials

tris(8-hydroxyquinoline) aluminum (Alq3) (Aldrich) was purified by sublimation and N,N′-Bis(3-methylphenyl)-N,N′-diphenylbenzidine (TPD) (Aldrich) was used as received. 5,6,11,12-tetraphenylnaphthacene (Rubrene) (sublimed, Aldrich) was used as received. Poly(3,4-ethylendioxythiophene)-poly(styrenesulfonate) (PEDOT) (2.8 wt % dispersion in H_2O, low-conductivity grade) was diluted with 1:1 ratio in DI water and sonificated before deposition. Octadecyl-trichlorosilane (OTS) (GELEST, INC.) was used as received. Chloroform (ACS grade) was used as received without further purification. ITO/glass was purchased from Delta technology (ITO thickness: 100 nm,

substrate thickness: 0.7 mm, sheet resistance, R_s: 15 – 25 Ω, nominal optical transmittance: > 78%).

2.2.2 Thin Film Fabrication

P-type Silicon wafers [100] (1 – 10 Ω·cm) were used as substrates to prepare Alq3 films for morphology scanning of atomic force microscopy (AFM), X-ray diffraction (XRD), photoluminescence (PL) intensity vs. wavelength. The wafer was diced in rectangular pieces and sonicated for 10 min at room temperature and rinsed with DI water, and then cleaned with a hot 'piranha solution' (25% concentrated hydrogen peroxide, 75% concentrated sulfuric acid, hazardous solution!) for 1 hr to remove organic contaminants and strip original thin silicon oxide surface layer. Finally, the treated substrates were sonicated and thoroughly rinsed with DI water and dried under dry nitrogen flow. This treatment results in a fresh silicon oxide layer of 1.0-1.2 nm with a high density of silanol (Si-OH) groups. The Alq3 solution was prepared with concentration of 0.5 wt. % in chloroform. The solutions were prepared in UV and short wavelength filtered clean room lighting in order to prevent from pre-photo-oxidation in solution state. The Alq3 solution was then spin-cast at 3000 rpm for 30 seconds on the cleaned Si substrate, which results in 50 nm uniform Alq3 thin films.

2.2.3. Thin Film Characterization

The thickness of organic films was measured by surface profilometry and optical ellipsometry. The amorphous Alq3 films were characterized by using AFM, X-ray diffraction (XRD), and photoluminescence to study film properties. The morphology of the thin films was observed by atomic force microscopy (AFM) with intermittent-contact

mode with low spring force constant (40 N/m) and resonance frequency (325 kHz). The quality of the film was determined by the roughness measurement (RMS roughness). XRD investigation was carried out with a Cu K-alpha standard radiation source (λ = 1.54060Å) with an acceleration voltage of 45 kV and a current flow of 40 mA. The PL intensity vs. wavelength was measured by a SPEX fluorolog **(**HORIBA Jobin Yvon Inc.) at excitation wavelength 365nm. The excitation source is a xenon lamp which is passed through a monochromator. The excitation bandwidth is approximately 15 nm (-5/+10). Collection is done with a second monochromator and detection with a photomultiplier tube.

2.2.4. Pixel Patterning

Microchannel or square well arrays with widths ranging from 100 μm down to 10 μm and depths from 0.1 to 1 μm in the active area of 6 × 6 mm^2 were fabricated in silicon using standard microfabrication techniques. Prepatterned wells were fabricated by KOH wet etching. The 500 nm silicon dioxide layer was grown by thermal oxidation as a wet etching mask. The SiO_2/Si wafers were cleaned via standard cleaning recipe as follows: sequential ultrasonic rinse in acetone, methanol, isopropyl alcohol, DI water, and baked at 200 °C prior to deposition of photoresist. The microchannels or wells were patterned by photolithography using Shipley 1813 positive photoresist and then developed with Shipley 352 developer to open etching areas. The photoresist-patterned wafer was baked on hot plate at 120°C for 5 min to harden the photoresist to acid. The wafer was etched with BOE to define the following KOH etching region. The patterned wafer was etched for 0.1 ~ 1 μm with 60 wt. % KOH at 60°C with high speed stirring to remove formation of vapor on the Si surface, and then the SiO_2 mask was removed with BOE.

This special etching procedure leaves a smooth Si surface. The wafer was diced into squares, 13 × 13 mm^2. The diced substrates were oxidized by oxygen plasma for one minute to build a silicon dioxide layer. The substrates were treated with solution method in 1mM octadecyltrichlorosilane (OTS)/toluene solution for 1hr. The substrates were rinsed thoroughly with toluene and chloroform in ultrasonic bath for 10 min each, which removes residues of OTS clusters or dust from the surface and leaves a smooth nanolayer with thickness 1 to 2 nm. The OTS treated substrates were hydrophobic with contact angle of > 90°. The 0.5 ~ 1 wt. % Alq3 solutions in chloroform were drop-cast through 0.4 μm pore size filter on the spinning hydrophobic microchannels and wells patterned substrates at 3000 rpm for 30 seconds. All the patterning procedures were performed in UV and short wavelength filtered clean room lighting. The segregation of Alq3 in the microchannels and wells were investigated with optical microscopy and fluorescence microscopy.

2.2.5. Micropixel OLED Fabrication

ITO/glass plate was diced in squares, 13 × 13 mm^2 with active area, 6 × 6 mm^2 to fit in the shadow mask. The ITO/glass substrates were cleaned via standard cleaning recipes as follows: sequential rinse with acetone, methanol, isopropyl alcohol, and DI water in untrasonic bath for 10 min each. Insulating microwalls were fabricated in SiO_2/ITO/glass as described follows. The SiO_2 was deposited onto ITO/glass (bottom-emitting structure) substrates by plasma enhanced chemical vapor deposition (PECVD) (Oxford Plasmalab 80) with deposition rate, 15 ~ 20 nm/min. The thickness of SiO_2 layer was from 150 to 300 nm, determined by ellipsometry (Spectroscopic ellipsometer) and profiler (Tencor P-10 Profilometer). The substrates were cleaned in an ultrasonic

bath with DI water and the wells were patterned by photolithography as described above. The micro insulating wells range in width from 100 μm down to 10 μm. The patterned substrates were dry-etched by PECVD (Oxford Plasmalab 80) using CF_4 with etching rate, 35 ~ 37 nm in depths from 150 nm to 300 nm because wet-etching rate of PECVD SiO_2 is too fast to control and dry etching provides vertically precise walls. The substrates were treated with 1mM OTS as described in pixel-patterning section. The diluted PEDOT was filtered through 0.4 μm pore size filter and spin-cast at 3000 rpm for 1min, yielding ~ 50 nm film. The PEDOT film was cured in oven at 120°C for 1hr to remove the leftover water and improve adhesion of film, and taped off to remove the residue layers on the top of prepatterned wells. The Alq3/TPD mixture was dissolved with 1wt. % in chloroform in ultrasonic bath for 10 min. The mixture was drop-cast through 0.4 μm pore size filter on spinning substrate. The segregation of Alq3/TPD layers in the microwells was investigated with optical microscopy and fluorescence microscopy. In the case of device fabrication for electrical test, the patterned substrates were protected from light until loading in thermal evaporation system and the observation with optical microscopy and fluorescence microscopy were passed over. All the fabrication procedures were done in nitrogen ambient grove box to prevent from photo-oxidation of the organic films. After patterning the Alq3/TPD pixels, LiF/Al (bottom-emitting structure) were deposited as the electron injection and the cathode in high vacuum thermal evaporation system with a base pressure less than 10^{-6} Torr and deposition rate, 0.5 ~ 1 Å/s. The devices were completed by packaging using optical adhesive (Norland Product Inc.), covered by thin glass slide under long wavelength UV.

2.2.6. OLED Characterizations

EL spectra (EL intensity vs. wavelength) were measured by a multichannel spectrometer. Luminance-current-voltage characteristics (L-I-V) were measured by using a radiometer and a digital voltmeter (computer controlled Keithley 236 source) until the curves saturate. The completed OLEDs were mounted onto the surface of a silicon photodiode module (PIN-10D, OSI optoelectronics) in the forward emission direction. All the tests were done in air because the ultimate goal of this report is a processing technique using mixed active organic layer, which will reduce the efficiencies, and to prove that practical device can be made by spin-on patterning technique.

2.3 Results and Discussion

2.3.1. Characterization of Spin-Cast Films

In this patterning technique, obtaining an amorphous film with uniform surface coverage within the prepatterned grids is the main concern because emission color and local current density with applied voltage strongly depend on film quality.[73] The morphological and structural properties were investigated by atomic force microscopy (AFM) and X-ray diffraction (XRD). AFM scanning of spin-cast Alq3 showed smooth and uniform films with no obvious cracks or pinholes, with 2.9 Å RMS surface roughness, as indicated in Figure 2.2. Interestingly, spin-casting produced a smoother surface than thermal evaporation (RMS roughness 3.7 Å).

XRD scans indicated that Alq3 films prepared by both thermal evaporation and spin-casting are in the glassy amorphous state. An amorphous film without morphological imperfections exhibits isotropic properties due to the absence of a grain -

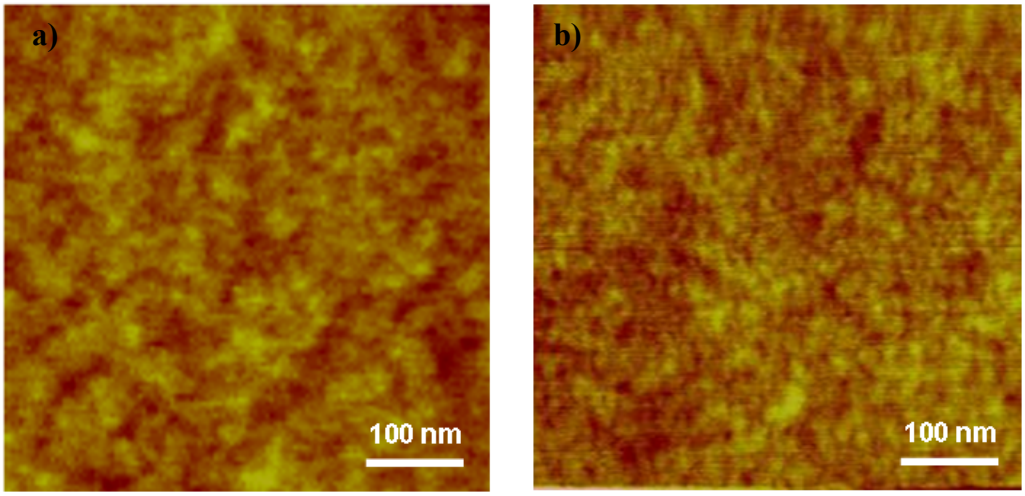

Figure 2.2. AFM topographic scans obtained using intermittent-contact mode; scan sizes are 500 nm × 500 nm. A) thermally evaporated film (thickness: 50nm, RMS roughness: 3.7 Å) and B) spin-cast film (thickness: 50nm, RMS roughness: 2.9Å).

boundary. Figure 2.3. shows a typical photoluminescence (PL) emission peak of Alq3 film around 520 nm, producing green emission. The PL efficiently addresses any structural or chemical structural changes for Alq3 molecules during spin casting process. The PL spectrum can be disturbed by impurities, stress, or morphological deformations in the film during the deposition process. If the film undergoes stress during deposition, the PL emission peak blue shifts, while the formation of crystalline structures in the film causes the emission peak to red shift.[8] Thus, PL measurement provides a sensitive diagnostic of film properties. As shown in Figure 2.3, the emission spectra of spin-cast and thermally-evaporated Alq3 films are consistent, with stronger PL intensity from the spin-cast film.

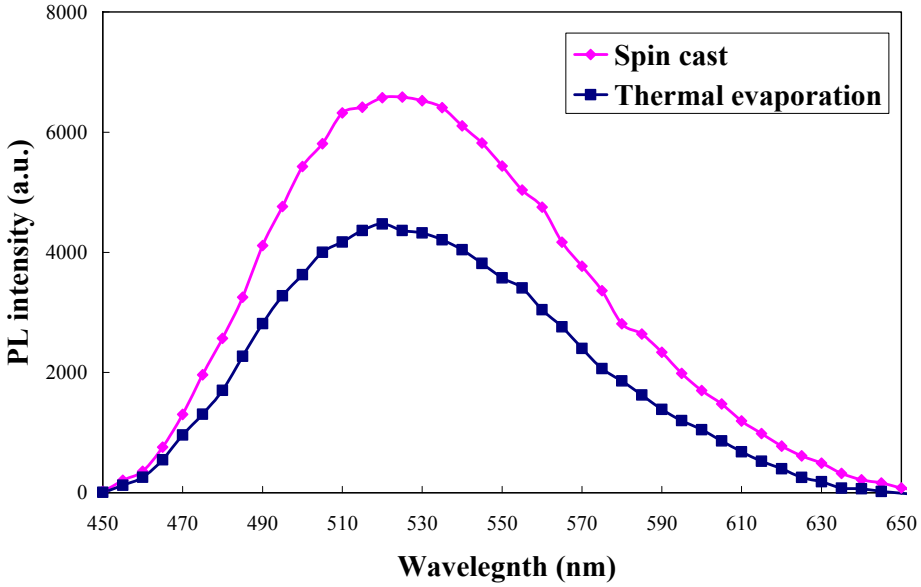

Figure 2.3. PL spectra of Alq3 film deposited by thermal evaporation (square, blue) and by spin-casting (circle, red). The excitation wavelength is 365 nm.

2.3.2. Pixel Patterning

Here, we demonstrate a pixel patterning method by spin-casting combined with a structured surface to achieve directed self-assembly of Alq3 pixels with well-defined pixel size and long-range order. Figure 2.4 describes the spin-on patterning processes of Alq3 on a prepatterned silicon substrate. The silicon substrate was wet-etched by KOH to obtain a smooth surface. The addition of hydrophobic octadecyltrichlorosilane (OTS) to the surface discourages the adsorption of Alq3/TPD, thereby resulting in selective deposition in the prepatterned microchannels or wells. Alq3 (or rubrene) solution in chloroform was dropped onto the spinning micropatterned substrates. The organic molecules on top are unstable and move toward the edges of the substrate during spinning, but the organic molecules on the bottom are trapped in the prepatterned microchannel or wells.

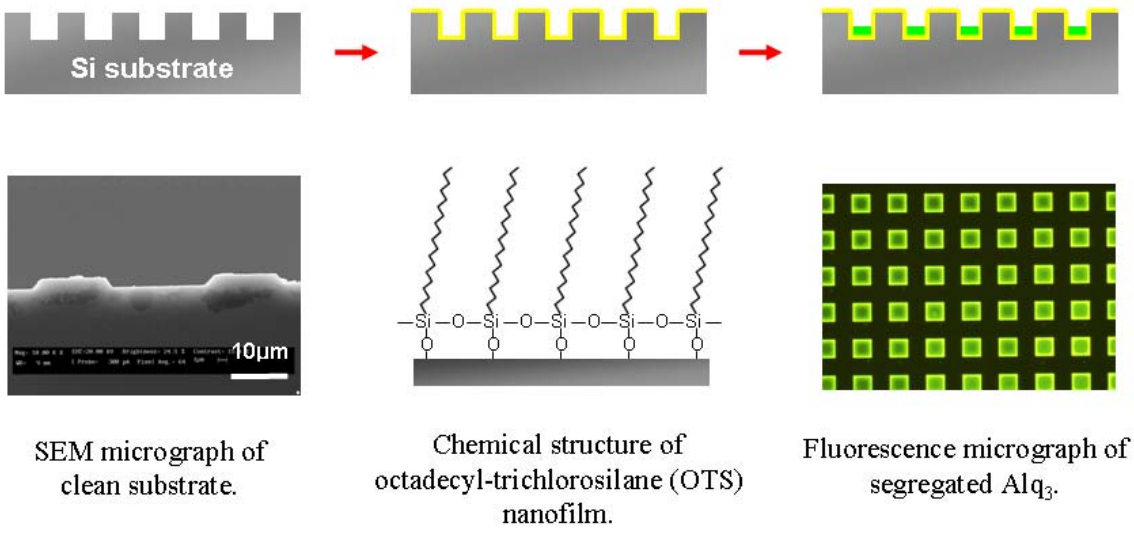

Figure 2.4. Schematics of the spin-on patterning process onto prepatterned substrates.

The organic films formed in the prepatterned channels and wells were observed by florescence microscopy with pixel sizes ranging from 10 μm to 100 μm, as shown in Figure 2.5. 5,6,11,12-tetraphenylnaphthacene (rubrene) is a p-type organic semiconductor material, yielding greenish-yellow emission at around 560nm. Rubrene is used to demonstrate that this technique can be used for various organic materials (Figure 2.5). Rubrene films were also formed precisely and uniformly within the pre-patterned channels. Without OTS treatment, a uniform organic film forms across the entire substrate. Figure 2.6 shows the florescence images of rubrene and the Alq3 on patterned substrates, but without OTS treatment, are presented in Figure 2.7.

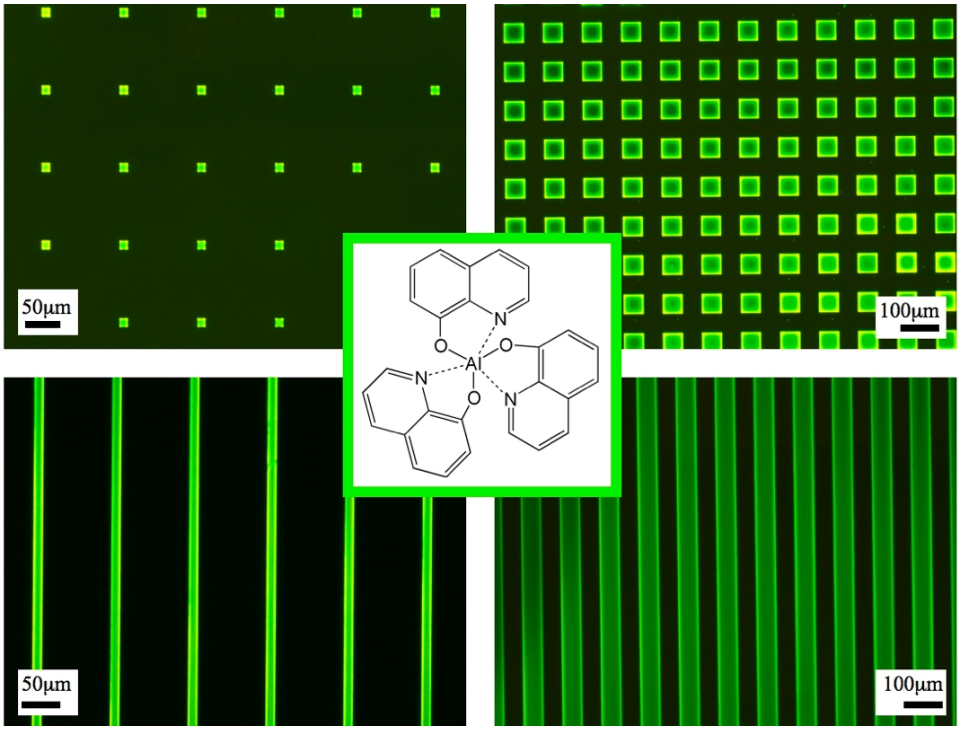

Figure 2.5. Photoluminescence images of patterned Alq3: the widths of square pixels (wells) are 10 μm (left on the top) and 50 μm (right on the top), and the widths of channel pixels are 10 μm (left on the bottom) and 50 μm (right on the bottom), respectively. Excitation is at 365nm.

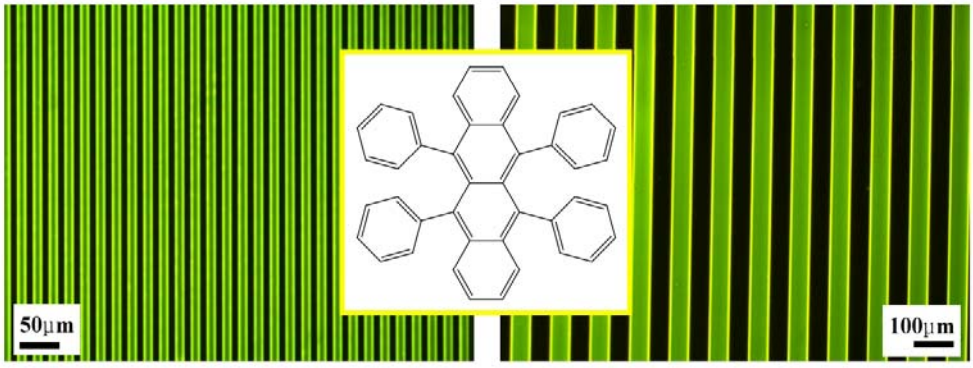

Figure 2.6. Photoluminescence images of patterned rubrene: the widths of channels are 10 μm (left) and 50 μm (right), respectively.

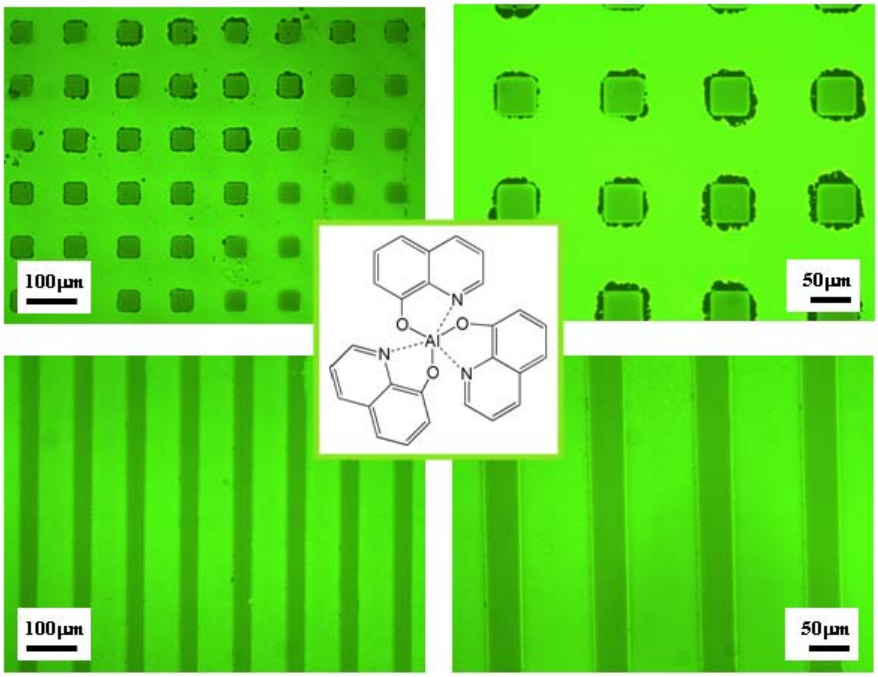

Figure 2.7. Photoluminescence images spun cast of Alq3 without OTS treatment: the widths of square pixels (wells) are 50 μm (left on the top) and 50 μm (right on the top), and the widths of channel pixels are 50 μm (left on the bottom) and 50 μm (right on the bottom), respectively. Excitation is at 365nm.

Pattern formation is described by four components: surface hydrophobicity, polarity of the solvent, solvent evaporation rate, and centrifugal force (rotational velocity). Initially, organic molecules in a nonpolar solvent spread out across a hydrophobic surface during spin-casting. However, a hydrophobic surface with high density OTS repels electrically nonpolarized organic molecules in a nonpolar solvent to decrease the contacting area. The organic molecules trapped in the prepatterned wells are immobilized due to the rapid evaporation rate of the solvent during spin-casting. This phenomenon indicates that the organic molecules are driven to the correct interfacial

energy during spin-casting, which leaves the organic molecules as a thin film by centrifugal force.

The spreading coefficient S determines the wettability of a liquid (Alq3 solution) on a solid surface (OTS-treated hydrophobic surface):

$$S = \gamma_{SV} - \gamma_{LV} - \gamma_{SL} \tag{2–1}$$

where γ_{SV} is the solid-vapor interfacial energy, γ_{LV} is the liquid-vapor interfacial energy, and γ_{SL} is the solid-liquid interfacial energy (Figure 2.8). If $S > 0$, the surface is considered wettable, and if $S < 0$, dewetting occurs.

When the interfacial energies are in equilibrium, we obtain the interfacial energy γ_{SL} from Young's equation:[74]

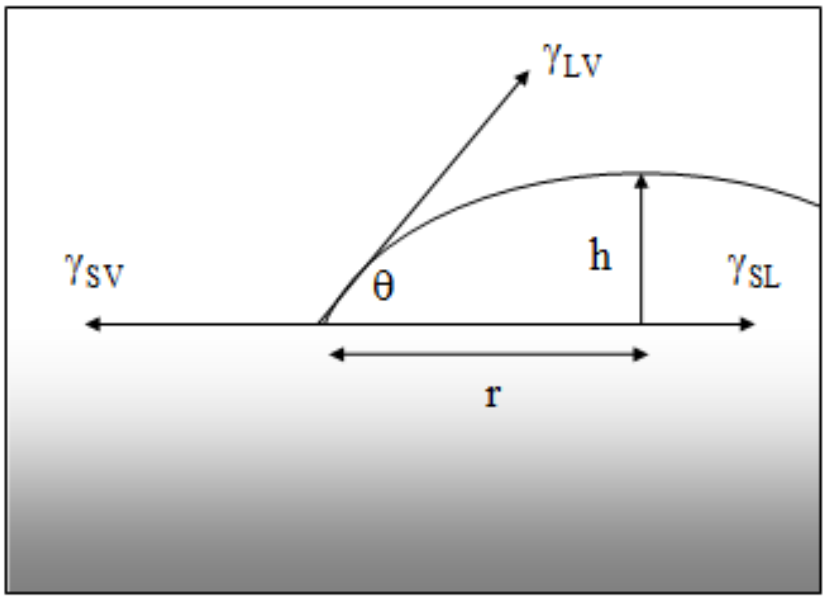

Figure 2.8. Schematics of interfacial energy in Young's equation

$$0 = \gamma_{SV} - \gamma_{SL} - \gamma_{LV} \cos\theta_0 \qquad (2\text{–}2)$$

where θ_0 is the equilibrium contact angle of the OTS nanolayer (~ 100°), and γ_{LV} (chloroform: 0.027 J/m^2 at 25 °C) and γ_{SV} (OTS: 0.024 J/m^2 at 25°C) are known values.[75] The resulting spreading coefficient is negative by equation (2-1). Thus, we can predict that the organic film is dewetting on the OTS nanolayer during spin-casting.

2.3.3. Reference OLED Characterization

OLED structures based upon Alq3/TPD have been studied widely since these materials typically produce efficient performance for green emitting displays.[76] The device structure in this research consists of stacks of PEDOT/TPD- Alq3/LiF/Al as the best performance for Alq3 based OLEDs has been obtained with this structure.[77] The effects of the electron injection layer (EIL) and hole injection layer (HIL) for device performance in Alq3 based OLEDs are summarized in Table 2.1.

The energy diagram and the structure of top- and bottom-emitting structures are described by using: 1) rubrene as luminescence and HTL layers, 2) Alq3 as luminescence and ETL layers in Figure 2.9. The design of stacking organic and metal layers is critical to device performance, since charge injection and transport are the limiting factors in determining operating voltage and quantum and luminance efficiencies. Besides organic materials, the selection of proper hole and electron-injecting electrode materials can also improve device efficiencies. A LiF/Al bilayer is chosen for the cathode because LiF is thermodynamically stable and results in lower turn-on voltage, and the stack of LiF/Al provides higher EL efficiencies than a Mg:Ag cathode.

Table 2.1. Device performances for Alq3 based OLEDs

Structures	Layers	Brightness (cd/m^2)	Turn on Voltage (V)	Max. EL efficiency, (cd/A)	Max. Ext. quantum efficiency (%)
Bottom	ITO/Diamine/ Alq3/Mg:Ag	1000 at 10V	–	–	1
Bottom	ITO/TPD: Alq3:PMMA/Mg:Ag[78]	300 at 15V	–	–	–
Bottom	ITO/TPD/ Alq3/Al	250 at 25V	12	1.4	0.34
Bottom	ITO/TPD/ Alq3/LiF/Al	828 at 25V	9	1.98	0.49
Bottom	ITO/Cupc/TPD/ Alq3/LiF/Al	1150 at 25V	9	4.51	1.1
Bottom	**ITO/PEDOT/TPD/Alq3/LiF/Al**	**1760 at 25V**	**3**	**8.2**	**2**
Top	Mg:Ag/ Alq3/TPD/PTCDA/ITO[79]	100	1.5	–	0.3
Top	Ag/Ag_2O/m-MTDATA /NPB/Alq/LiF/Al/Ag[80]	1400 at 13V	–	1.4	–
Top	**Ag/Ag_2O/m-MTDATA /α-NPD/Alq3/LiF/Al/Ag/TeO_2[81]**	**1700 at 10V**	**2**	**6**	**–**
Trans.	ITO/TPD/ Alq3/Mg:Ag/ITO[82]	500 at 10V	3	–	0.1
Trans	ITO/TPD/ Alq3/LiF/Mg:Ag/Alq_3[83]	–	2.8	3.4	–

Test devices were fabricated by spin casting uniform Alq3/TPD layers prior to making pixel patterned devices. The structure with a PEDOT hole injection layer is ITO/PEDOT/TPD/Alq3/LiF/Al. Figure 2.10 shows the bottom emitting structure and corresponding energy band diagram. The single emissive layer is a mixture of tris (8-hydroxyquinoline) aluminum (Alq3) as the electron transport and emissive material and N,N′-Bis(3-methylphenyl)-N,N′-diphenylbenzidine (TPD) as the hole transport material, yielding typical green Alq3 electroluminescence.

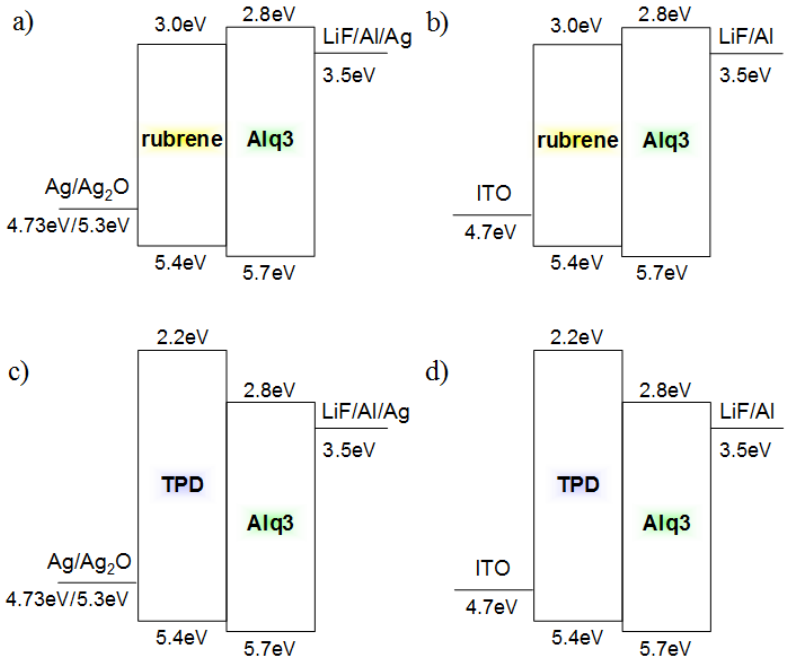

Figure 2.9. HOMO and LUMO level of the materials with respect to vacuum level, a) top emitting rubrene OLED, b) bottom emitting rubrene OLED, c) top emitting Alq3 OLED, d) bottom emitting Alq3 OLED.

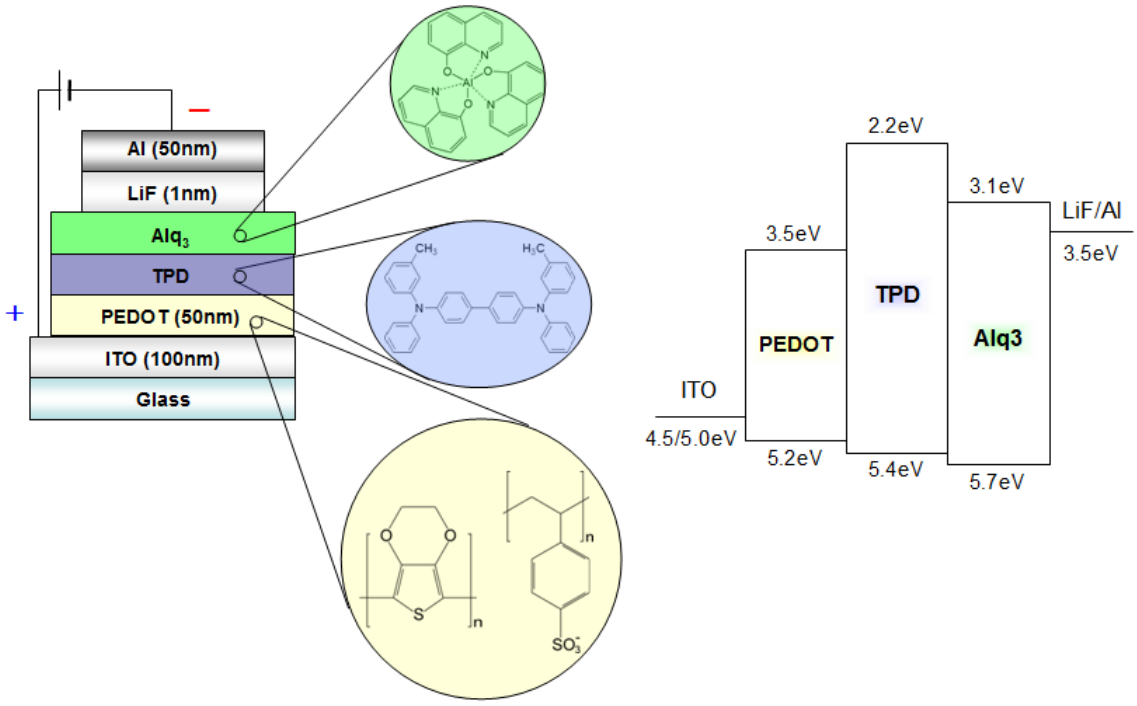

Figure 2.10. Bottom-emitting structure and energy band diagram of Alq3 based OLED.

Despite the advantage of solution-based techniques of high-speed deposition rate, the solvent used in the technique can chemically destroy any predeposited layers, which would limit the device performance significantly. Hence, the ETL (Alq3) and HTL (TPD) materials are blended into one solution, which enables a single layer device.

It has been noticed that spin casting provides a smoother surface than that prepared by thermal evaporation. We tested the possibility to improve the affinity of the Alq3/TPD organic layer with the ITO interface by spin casting a hole injection layer, poly(3,4-ethylenedioxythiophene)–poly(styrene) (PEDOT/PSS). A smooth organic interface results in reduction of electrical shorts and in the threshold voltage.[84] The roughness test by AFM shows that PEDOT smoothes the rough ITO layer (RMS roughness: 8.4 Å) by twofold (RMS roughness: 4.1 Å), but subsequent deposition of Alq3/TPD increases roughness (RMS roughness: 7.5 Å) as shown by AFM images in Figure 2.11. However, the Alq3/TPD layer on PEDOT is smoother than if directly spin cast on ITO (RMS roughness: 1.7 nm).[73] The initial PEDOT roughness on ITO/glass is comparable to other published reports which is about 1 – 3 nm because the polished ITO/glass provides a smoother surface than normal ITO/glass.[85,86]

Figure 2.12 shows the L-I-V characteristics of non-PEDOT and PEDOT devices. The Alq3 based OLED prepared by spin casting has a turn on voltage around 6V to 8V. The use of PEDOT reduces the turn on voltage closer to 6V from ~7.5V and provides linear current injection because PEDOT reduces the energy barrier by about 0.2 eV between the anode (ITO) and HTL (TPD) layers, which improves hole injection and transport.[86]

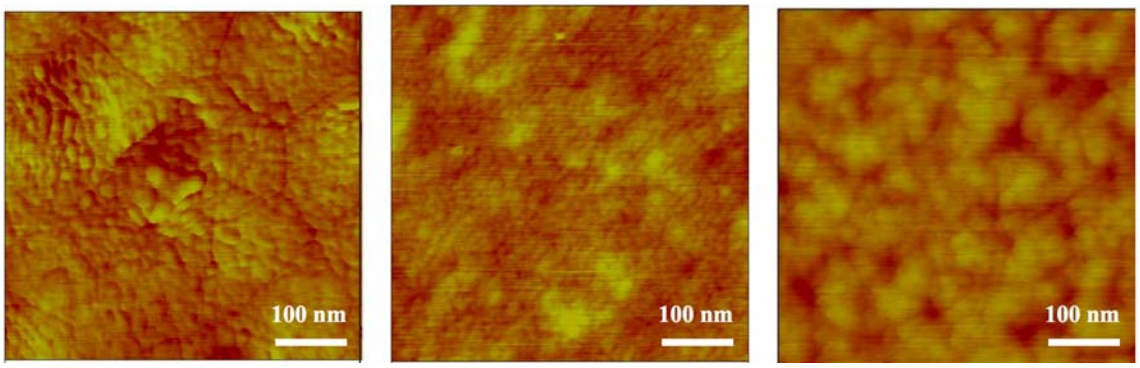

Figure 2.11. AFM topographic images scanned by intermittent-contact mode. Scan size is 500 nm × 500 nm: 1) ITO (RMS roughness: 8.4 Å) 2) ITO/PEDOT (RMS roughness: 4.1 Å), 3) ITO/PEDOT/ Alq3-TPD (RMS roughness: 7.5 Å).

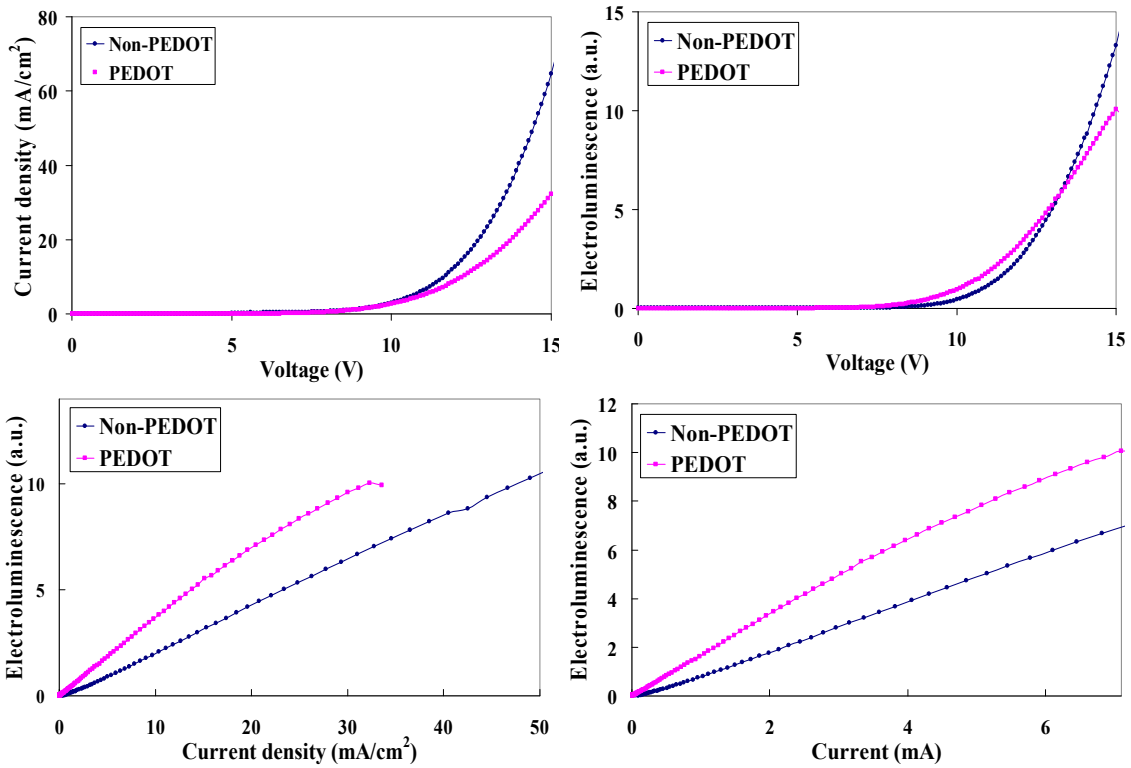

Figure 2.12. Forward-biased current – voltage characteristics, light output – voltage and light output – current characteristics of test device prepared by spin casting with PEDOT and non-PEDOT, a pixel area is 0.22 cm^2.

Charge injection and transport are primarily responsible for operating voltage and luminance efficiency. We do not expect to obtain higher efficiency than a single heterojunction device prepared by thermal evaporation since we use mixed HTL/ETL layer to achieve a one step patterning process. Charge balance is an important factor in OLED efficiency and the heterojunction is an effective structure by reducing non-radiative exciton recombination pathways by inducing hole and electrons in an emissive host layer. The PEDOT device shows lower current density above 11V and lower electroluminescence intensity above 13V as compared to the non-PEDOT device. However, the electroluminescence as a function of both current and the current density exhibited by the PEDOT device shows that it operates more efficiently than the non-PEDOT device. This is because the hole current is limited by injection and PEDOT increases hole injection to TPD, which drives an increase in the electron/hole recombination rate.

2.3.4. Fabrication of Micropatterned OLEDs

This solution-based spin-on patterning technique can resolve the problems of local pixel array and size through the use of photolithography, which allows higher resolution patterning of OLED pixels compared to shadow masking; here, we demonstrate pixels as small as 10 μm. This single step solution-based approach to forming precise patterns of amorphous Alq3 is ideal for large area OLED pixel arrays. The process of fabricating a bottom-emitting structure using the spin-on patterning technique is presented in Figure 2.13. Insulating microchannels and wells are fabricated in SiO_2 using microfabrication techniques. SiO_2 is deposited onto glass/ITO by plasma enhanced chemical vapor deposition (PECVD). The wells range in width from 50 μm down to 10 μm, and in

depth from 150 nm to 300 nm. Prior to spin-casting the organic layers, substrates are treated with OTS in order to inhibit adsorption of organic molecules on the top surface, yielding selective deposition in the wells. PEDOT is spin-cast on the substrate before spin casting of the Alq3/TPD layer. The ideal thickness of the active organic layer is 100 nm, and the ideal thickness is 50nm for PEDOT. After patterning the Alq3/TPD pixels, LiF and Al are deposited by thermal evaporation as the electron injection layer and cathode, respectively, in sequence and packaged to prevent from the degradation of the organic film in air. The fabrication process is described in Figure 2.13.

In this technique, obtaining an amorphous film with uniform surface coverage in the prepatterned regions is the main objective, because the local current density with applied voltage strongly depends on film qualities. Figure 2.14 shows scanning electron microscopy (SEM) and photoluminescence images of the patterned OLED pixels. The SEM images (a) and (b) were taken after dry-etching the SiO_2 layer. The photoluminescence images were taken after deposition of the OTS nanolayer and spin-casting of the Alq3/TPD layer. One limitation of this spin-on patterning technique is that the solution is driven into the edges of the prepatterned channels or wells. Sample (c) is prepared by spin-casting Alq3/TPD on an OTS treated substrate without the PEDOT layer. The image clearly shows accumulation of organic at the edges, which will eventually drop the device efficiency. Uniform thickness is important since the operating voltage required for light emission is strongly dependent on the thickness of the organic materials. PEDOT can be deposited on the OTS treated prepatterned substrate as a hole injection layer. In addition, the PEDOT layer prevents edge accumulation as shown in photoluminescence image (d) through the increased affinity of Alq3/TPD to PEDOT.

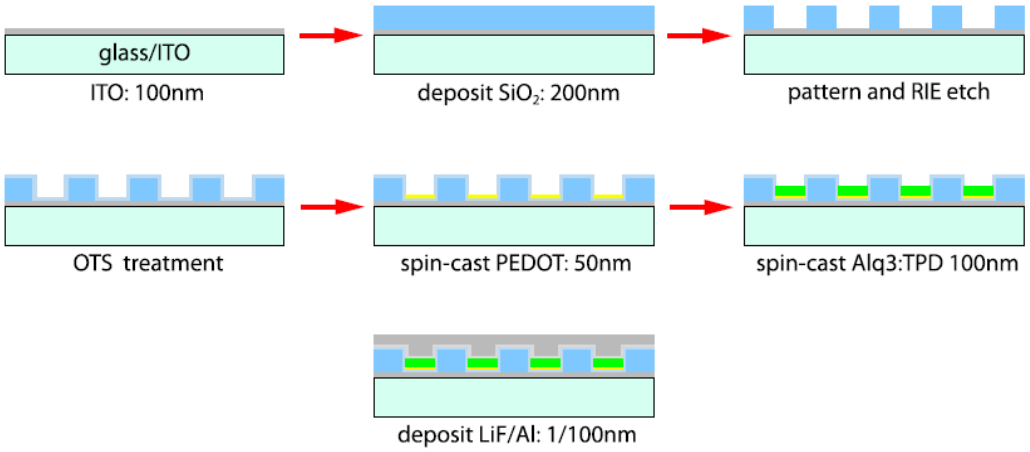

Figure 2.13. Process flows of fabrication of bottom emitting OLED by using spin-on method.

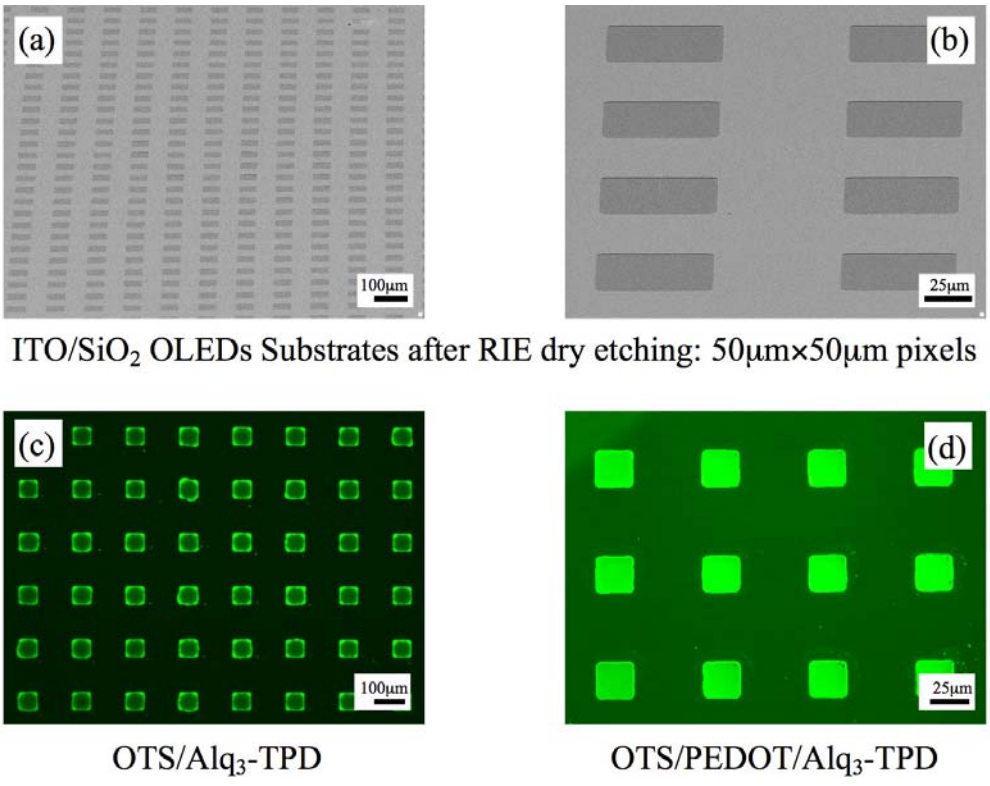

Figure 2.14. Scanning electron microscopy images: a) width 50 μm, b) 50 μm, and photoluminescence images of practical OLED pixels: c) without PEDOT, width 50 μm, d) with PEDOT, 50 μm. Excitation is at 365 nm.

2.3.5. Characterization of Micropatterned OLEDs

Figure 2.15 shows the electroluminescence emission spectrum of the patterned Alq3 based OLED, which shows the expected broad peak starting from 450nm through 800nm and maximum EL intensity at 542nm. This spectrum is close to that of typical Alq3 based OLEDs but slightly red-shifted compared with the PL of spin-cast Alq3 film. The small offset may be the result of slight change in the film morphology, which causes higher density of reside molecules in the film due to typical characteristics of the spin casting method. In addition, the shifting could be the result of mixing of Alq3 and TPD, where TPD affects the emission wavelength in a mixed state.

The micropatterned device without the OTS layer operates without current leakage and at a lower threshold voltage and higher current density as compared to the test device, as shown in the L-I-V curves of Figure 2.16. The difference between the two devices is-

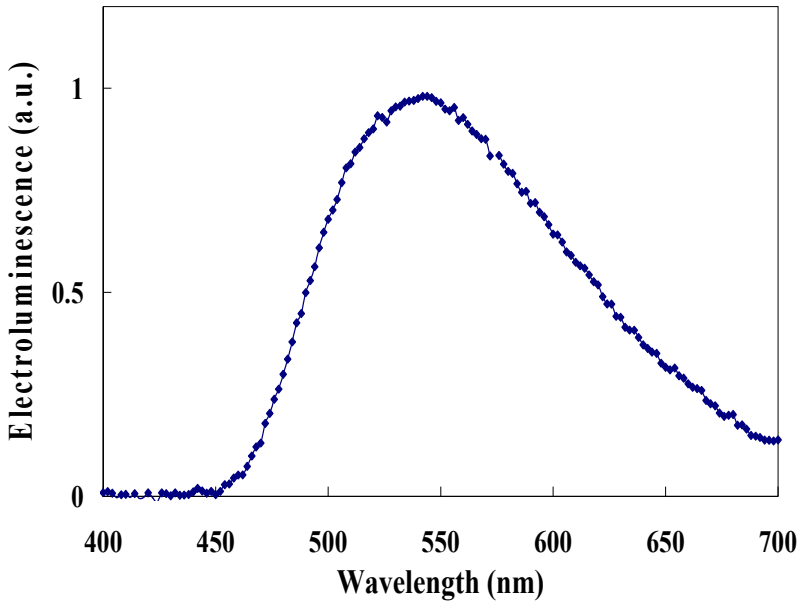

Figure 2.15. Electroluminescence spectrum of micropatterned device.

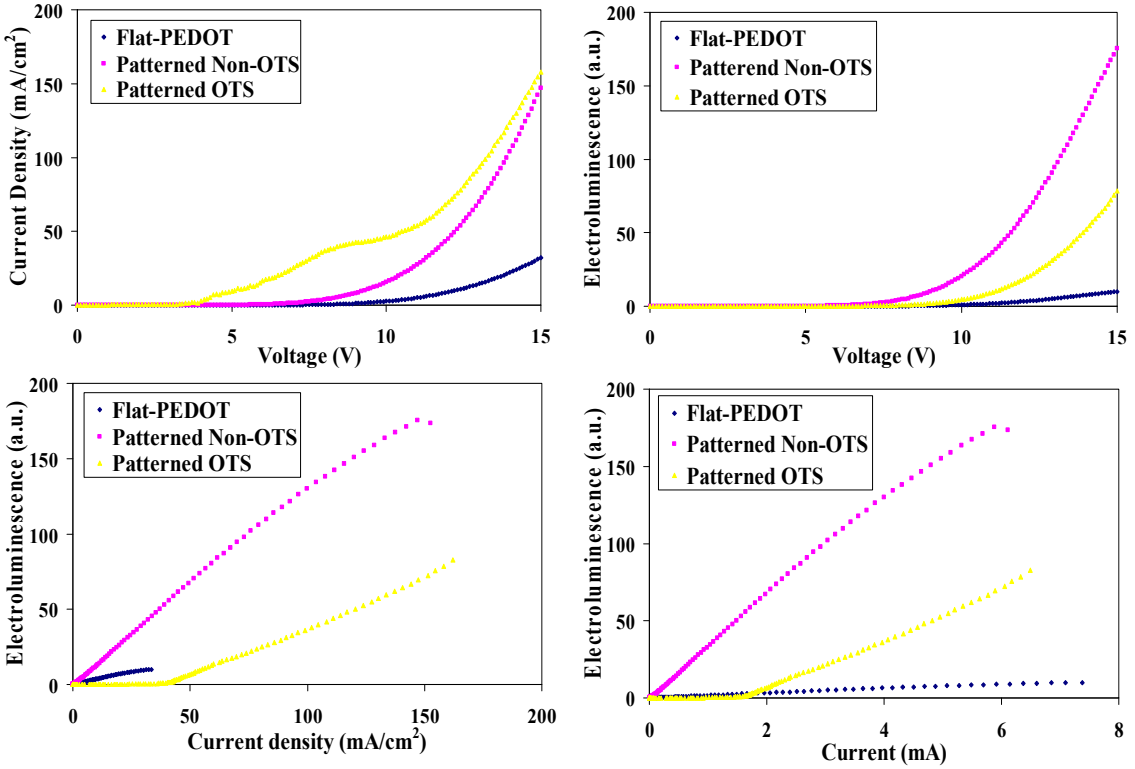

Figure 2.16. Electroluminescence – Current density – voltage (L – J – V) forward-biased characteristics of test device, patterned non-OTS and patterned OTS devices prepared by spin-casting.

geometrical structure. The test device consists of a flat organic layer on the ITO/glass substrate, while organic layers are deposited into wells with 150 nm to 300nm depths in the patterned device. This geometrical variation can induce an increase of density of chromophore due to centrifugal force during spin casting, which drives organic molecules to cluster in a closed area.

There are three factors to determine efficiency of OLED including charge carrier balance, radiative recombination, and light out coupling. If the injection of one charge carrier is unbalanced, the minor charge carrier will interact with excitons which result in

decay as nonradiative recombination. This higher density can reduce transport rate of hole to the recombination interface, which balances the number of electrons and holes and increases recombination rate because holes are the major charge carrier due to higher mobilities and small energy barrier than that of electrons. The EL efficiency depends on current density, which means higher charge injection and transport through organic layers and the device operates at lower applied voltages. This higher density drives higher current density that results in higher electroluminescence intensity by enhancing probability of recombination interface.

In micropatterned OTS devices, there is no current leakage observed at low voltages, but an abrupt change in current occurs in the I – V characteristics beyond 4V, which increases the current density, but leaves the threshold voltage around 5.8V, which is the same as the reference device. The EL intensity increases linearly and rises above the test device from 12V. A thinner organic layer provides a higher current density at the same applied voltage. However, this device operates with higher current density than the reference device and the micropatterned non-OTS device, and eventually generates higher EL intensity than the reference device. This could imply that the hole injection is improved or provides reduced resistance through OTS layer at inorganic-organic interface. The OTS device is not superior in operation than the non-OTS device, but the EL intensity versus current plot indicates that the OTS device works more efficiently than the reference device at high current. The OTS device shows lower efficiency at low current and passes over the test device beyond currents of 1.5 mA. This phenomenon can account for the abrupt current change at the low voltage. This change may generate Joule heating from the high current density rather than compensate in light emission. The role of OTS in OLED is not fully understood, whether the OTS

layer increases or interrupts hole injection, and if this high density of OTS nanolayer functions to prevent electrical shorts.

The data obtained from the tests can determine the quantum efficiency (η) and the luminous efficiency (η_P). The efficiency is estimated from the following equations:

$$\eta = \frac{\text{number of emitted quanta}}{\text{number of charge carriers}} = \frac{n_p}{n_e} = \frac{\iint \frac{2\pi E(\lambda,\theta)}{hc/\lambda} \sin\theta d\theta d\lambda}{I/e} \tag{2–3}$$

$$\eta_p = \frac{\text{number flux emitted}}{\text{consumed electric power}} = \frac{L_p}{IV} = \frac{\iint 2\pi E(\lambda,\theta) g(\lambda) \sin\theta d\theta d\lambda}{IV} = \eta \times \frac{\overline{hv}}{eV} \tag{2–4}$$

The quantum efficiency provides the comprehensive result of the EL processes (the injection of carriers, the formation of excitons, recombination of the electron and holes, and light emission), and the luminous efficiency gives more practical information. The internal quantum efficiency (η_{int}) and external quantum efficiency (η_{ext}) can be expressed as:

$$\eta_{\text{int}} = \gamma\eta_1\eta_2 \quad \text{and} \quad \eta_{ext} = \gamma\eta_1\eta_2\eta_3 \tag{2–5}$$

where γ is the fraction of excitons formed from the electrons, which is close to 1. η_1 is the luminance efficiency of the excitons, the ratio of singlet exciton and triplet exciton. From spin-statistics, only 25 % of excitons are in the siglet state, which relaxes to the ground state in order to conserve spin and generate fluorescence. Therefore, we lose

75% of the excitons to the triplet states. η_2 represents intrinsic quantum yield, the fraction of transitions from the singlet exciton to the ground state that are radiative. The variable η_3 is out-coupling efficiency defined as the fraction of the light emitted at the surface, ($1/2n^2$). The out-coupling efficiency, η_3 can be calculated by the equation:

$$\eta_3 = \frac{\text{surface emission}}{\text{all emitted light}} = 1-(1-(1/n_1^2))^{1/2} = \frac{1}{2n_1^2} \qquad (2\text{–}6)$$

This value is determined by the device structure and the refractive indices (n) of the composed layers because light is trapped in organic thin films by total internal reflection and finally absorbed in the devices, which loss is about 80%. Thus, maximum external quantum efficiency is about 2 ~3 %, as presented in Figure 2.17.

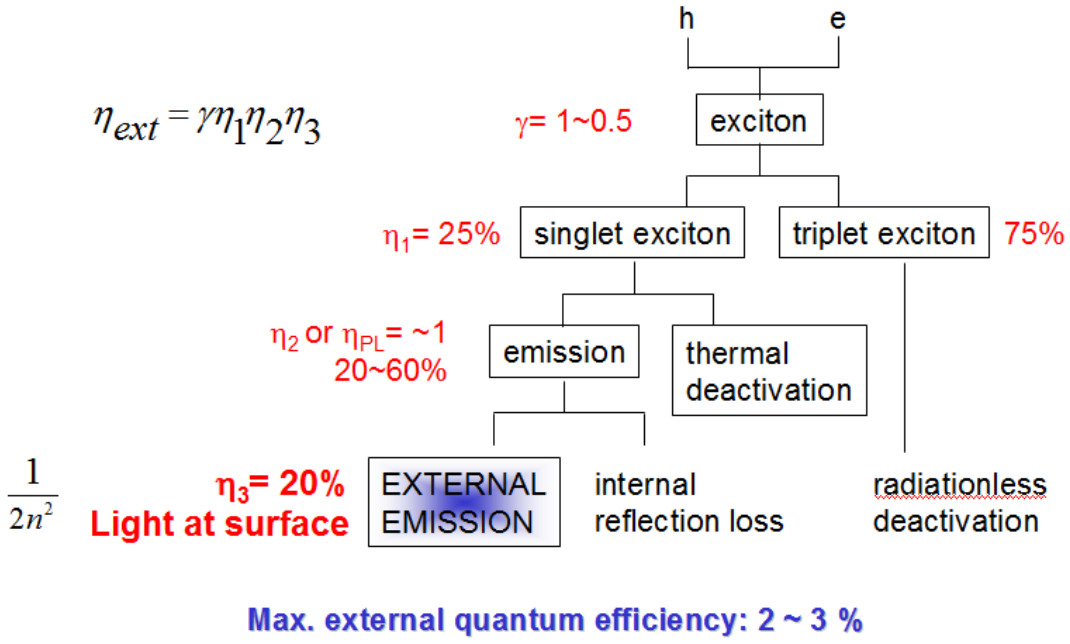

Figure 2.17. Roadmap of external quantum efficiency.

The micropatterned devices generated higher EL intensity with higher current density compared to nonpatterned flat devices. This phenomenon could be the result of the confined structure with low refractive index of silicon dioxide (n~1.46). In conventional OLEDs, the light out-coupling efficiency is limited to ~20% due to the relatively high refractive index of the organic active and surrounding layers, which results in optical confinement in the organic materials. This light is trapped as waveguided mode, which consequently decays nonradiatively (40~60%). Figure 2.18 describes ray diagram of bottom-emitting OLED and loss of light efficiency.[87]

Another mechanism of light trapping is total internal reflection (TIR) at the ITO/glass/air interface, which results in glass mode propagation (20~40%) by Snell's law (Figure 2.19).

The trapped light in the device can be extracted by embedding low index grid, which eventually improves out-coupling efficiency.[88] This is due to geometrical effect with low refractive index in that SiO_2 patterning changes the direction of trapped light by refraction toward free space. Figure 2.20 describes a possible ray direction in the patterned bottom emitting structure considering the geometrical effect.

Another way to improve light emission efficiency is to build up the periodic insulating wall with a photoresist which has higher refractive index (1.6~) rather than organic layer (1.5 – 1.8) or SiO_2 (1.5). This refractive index in the structure will improve light out coupling efficiency. The final external efficiency from current theoretical predictions is estimated as 2 – 3 %. Therefore, desired quantum efficiencies (η) and luminous efficiencies (η_P) in this research are close to 2 % and 8.2 %, which would be the highest efficiencies in Alq3 based OLEDs up to date.

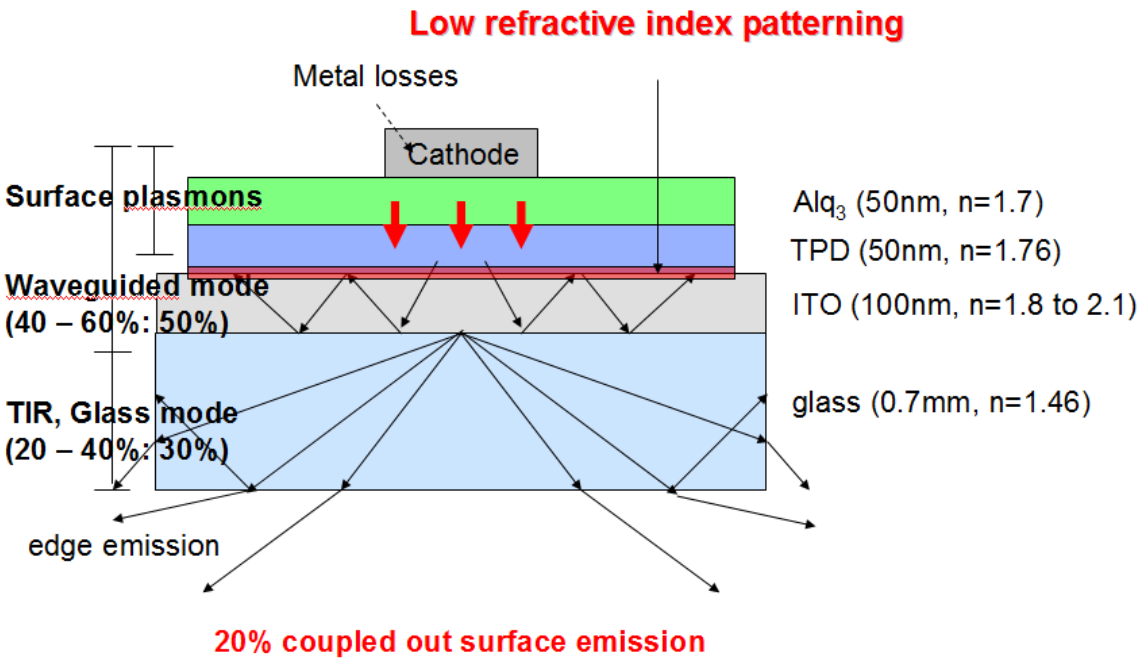

Figure 2.18. Ray diagram of bottom emitting organic light emitting device.[87]

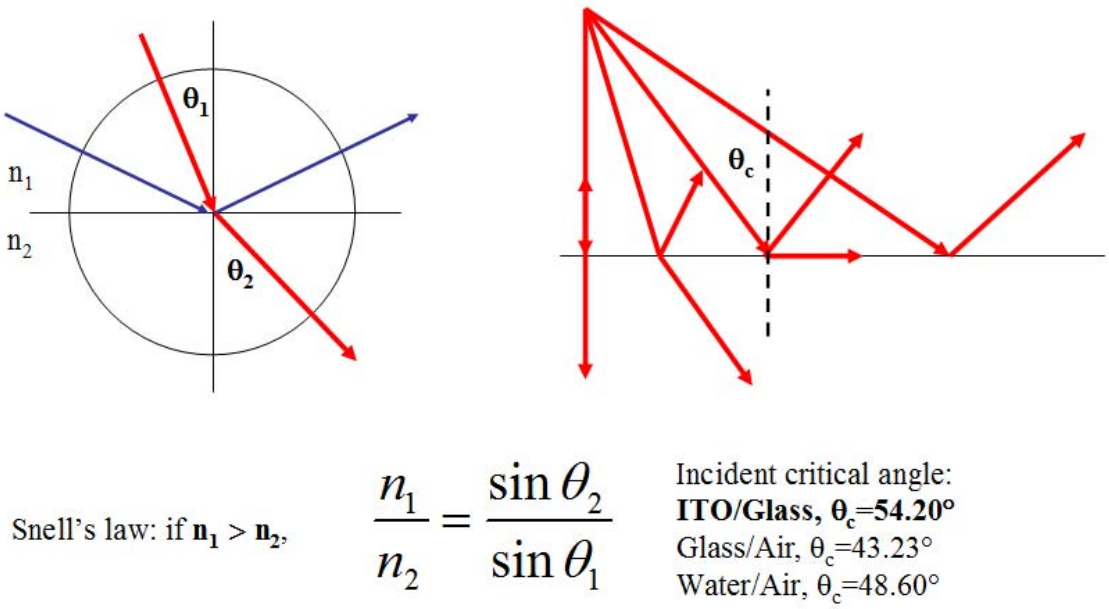

Figure 2.19. Total internal reflection and Snell's law.

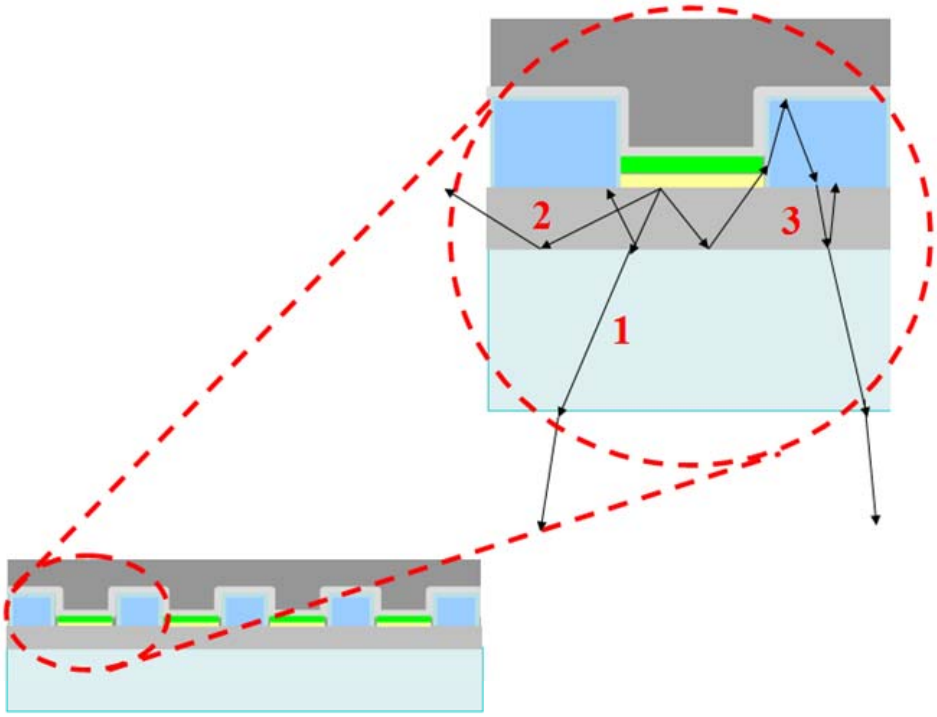

Figure 2.20. Schematic representation of ray diagram in the patterned bottom-emitting structure.

CHAPTER 3

OPTOELECTRONIC PROPERTIES OF N-TYPE Alq3 AND P-TYPE RUBRENE SINGLE CRYSTALS GROWN BY SOLVENT VAPOR RECRYSTALLIZATION

3.1 Hyphothesis and Specific Aims

The development of single crystallization technique for organic materials remains a significant research challenge. It is well known that OFETs require a crystalline morphology for high charge carrier mobility and efficient device operation. As such, the organic semiconductors commonly studied for OFET applications tend to form either large polycrystalline grains or large single crystals, and significant effort has been made to improve the crystallinity through various deposition and processing techniques.

In this research, we apply a novel crystallization technique to tris(8-hydroxyquinoline)aluminum (Alq_3) and 5,6,11,12-tetraphenylnaphthacene (rubrene). This solvent-vapor-assisted recystallization technique takes advantage of the tendency of organic semiconductor materials to transform from amorphous thin films into crystalline structures during exposure to solvent vapor. Crystalline Alq_3 will be investigated as a potential n-type semiconductor for OFETs. Rubrene is a p-type semiconductor, and has the highest reported hole mobility at room temperature for a single crystal OFET. The n- and p- type materials will be crystallized by using the solvent-vapor-assisted

recrystallization to achieve in-plane growth of Alq_3 and rubrene single crystals directly on a device substrate, with the crystals positioned in prepatterned transistor channels.

The purpose of this research is to implement a new crystallization technique for improving crystallinity and materials properties for optoelectronic applications. Here, we invented a novel crystallization technique using solution-based deposition for small molecules.

The goals of this research are to:

1) demonstrate the organic single crystal formation via solvent vapor recrystallization technique
2) improve the crystallinity via solvent-assisted-recrystallization technique
3) study optoelectronic properties of phase-shifted organic single crystals
4) utilize the recrystallization technique to fabricated n- and p- type transistor and characterize optimal transistor performance
5) develop crystal array technique by solvent vapor recrystallization without low resolution shadow mask
6) study electrical performance of the single crystal as OFET application

3.2 Experimental Procedures

3.2.1. Sample Preparation

Parylene substrate is prepared by chemical vapor deposition (CVD) for 3 μm which provides hydrophobic surface with contact angle > 90°. The reactor consists of a quartz tube with one closed end and three temperature zones. The dimer para-xylene is vaporized in the vaporization zone at ~ 100° C cleaves in the pyrolysis zone at ~ 700 °C, and polymerizes in the deposition zone at room temperature and pressure ~ 0.1 Torr.

Rubrene is highly soluble in aromatic or chlorine-based solvents. Rubrene solution is prepared with concentrations of 4 ~ 8 wt. % in ACS grade chloroform and toluene by sonification and heating the solutions until reaching saturated state. The solutions are prepared in fluorescent lighting filtered clean room in order to prevent from pre-photo-oxidation in solution state. The amorphous thin films were prepared by thermal evaporation and spin casting on the silicon substrate.

3.2.2 Physical Vapor Transport and Solvent Vapor Recrystallization

Phycical vapor deposition is used to deposit thin firm or growing crystal with condensation of vaporized form. The process includes high temperature vacuum evaporation with subsequent condensation in the glass tube as described in Figure 3.1. Orthorhombic rubrene crystals are grown in a horizontal glass tube by physical vapor transport in argon flow in an ambient pressure. The temperature of the tube was maintained between 310 °C and 240 °C. The crystals were grown on the surface of room temperature glass tube. Even though the physical vapor transport technique provides pure single crystals, the technique can offer only large bulk crystals on random places.

For the preparation of solvent vapor recrystallization, silicon substrate was placed in a glass jar equipped with a solvent beaker and then the jar was sealed to evaporate a desired solvent. The solvent was vaporized until vapor pressure was equilibrated in the entire volume. After the vapor filled in the jar, the vapor releasing needle was placed on top of the septum to lower vapor pressure since the surface of substrate is wet in the equilibrium state. The saturated solution was deposited on the substrates through -

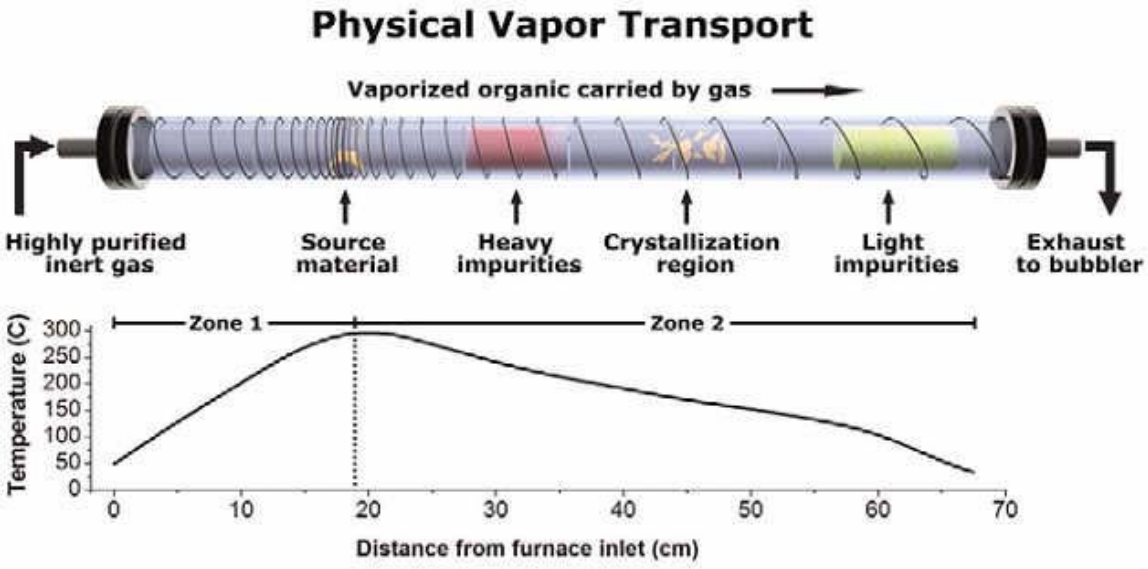

Figure 3.1. Schematics of crystal growth of physical vapor deposition.[89]

septum by using microneedle as described in Figure 3.2. The solvent evaporated slowly through the needle to nucleate the crystal. Alq3 crystals grown by solvent vapor recrystallization method are shown in Figure 3.3 and rubrene crystals are shown in result part.

Alq3 and rubrene crystal are grown in chloroform and methanol. Two different types of n and p type materials formed totally different crystalline structures. Figure 3.3 shows Alq3 crystals grown in chloroform, in air, and methanol solvent ambient after 24 hrs exposure time. Alq3 is an octahedrally coordinated chelate complex of the type MN3O3. There are three molecules of Alq3 in the asymmetric unit. This octahedrally coordinated complex crystallizes in the triclinic space group. Chloroform is nonpolar solvent with boiling point 61°C and polarity 4.8, and methanol is polar solvent with boiling point 65°C and polarity 33.

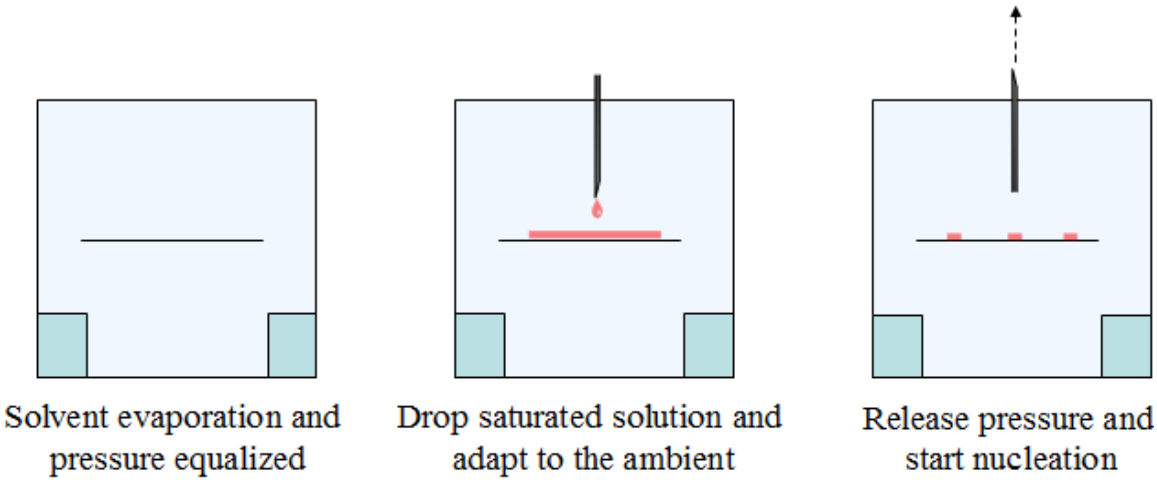

Figure 3.2. Schematics of solvent vapor recrystallization (SVR).

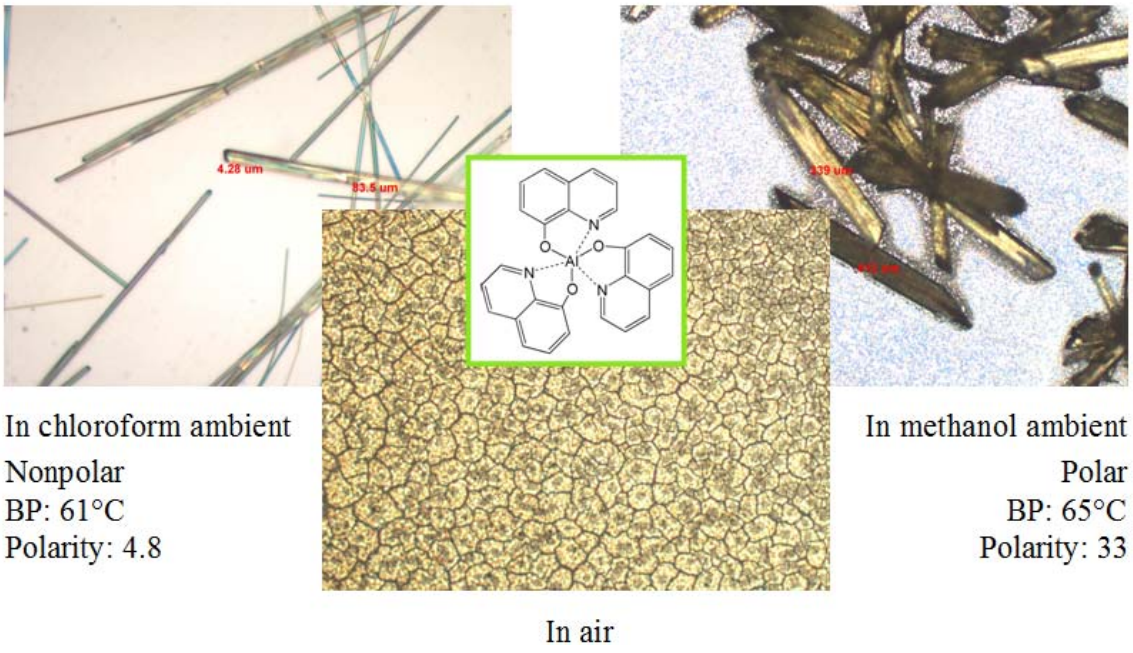

Figure 3.3. Alq3 crystal formation: left) in chloroform, center) in air, right) in methanol.

From here, we will focus on rubrene crystal because the molecule showed exceptional transition of crystalline structure and optical properties. The result will be discussed in Chapter 3 results.

3.2.3. Crystal Characterization

The PL intensity vs. wavelength was measured by SPEX fluorolog (HORIBA Jobin Yvon Inc.) at excitation wavelength from 370 to 470nm. The excitation source is a xenon lamp which is sent through a monochromator. The excitation bandwidth is approximately 15 nm (-5/+10). Collection is done with a second monochromator and detection with a photomultiplier tube. XRD investigation was carried out with a Cu K-alpha standard radiation source (λ = 1.54060Å) with an acceleration voltage of 45 kV and a current flow of 40 mA. The high resolution XRD was done in fixed slits 1/2 degree 0.02 radian soller slits with X'Celerator detector in full 2.2 degree active mode scanning by rotating sample set at 2sec/revolution. X-ray crystallography was performed as the following description. An yellowish-orange prism shaped crystal 0.35 x 0.30 x 0.23 mm in size was mounted on a glass fiber with traces of viscous oil and then transferred to a Nonius KappaCCD diffractometer equipped with Mo Kα radiation (λ = 0.71073 Å). Ten frames of data were collected at 150(1)K with an oscillation range of *1* deg/frame and an exposure time of 20 sec/frame with COLLECT Data Collection Software. Indexing and unit cell refinement based on all observed reflection from those 10 frames, indicated a monoclinic P lattice. A total of 14210 reflections (Θ_{max} = 27.5°) were indexed, integrated and corrected for Lorentz, polarization and absorption effects using DENZO-SMN and SCALEPAC.[90] Postrefinement of the unit cell gave *a* = 11.1686(2) Å, b = 21.7199(4) Å, c = 13.6222(3) Å, β =103.2309(10), and V = 3216.77(11) Å^3. Axial photographs and systematic absences were consistent with the compound having crystallized in the monoclinic space group $P2_1/c$. The structure was solved by a combination of direct methods and heavy atom using SIR 97.[91] All of the nonhydrogen atoms were refined with anisotropic displacement coefficients. Hydrogen atoms were

located and refined isotropically using SHELXL97.[92] There is a disordered solvent molecule (chloroform) in the asymmetric unit. The weighting scheme employed was w = $1/[\sigma^2(F_o^2) + (0.0637P)^2 + 0.8712P]$ where P = $(F_o^2 + 2F_c^2)/3$. The refinement converged to R1 = 0.0462, wR2 = 0.1102, and S = 1.025 for 5222 reflections with $1> 2\sigma$ (I), and R1 = 0.0759, wR2 = 0.1258, and S = 1.025 for 7376 unique reflections and 578 parameters.[93] The maximum Δ/σ in the final cycle of the least-squares was 0.001, and the residual peaks on the final difference-Fourier map ranged from -0.336 to 0.307 e/Å^3. Scattering factors were taken from the International Tables for Crystallography, Volume C.[94]

3.2.4 Fabrication of Organic Field Effect Transistors

The OFETs is fabricated with bottom contact structure, which enable deposition of solution directly onto channels and rotation of crystal in the desired direction. Both Alq_3 and rubrene are highly soluble in common organic solvents, and previous work has shown that amorphous films of these materials tend to crystallize when exposed to solvent vapor. In this technique, the device substrate is situated in solvent vapor ambient, and a solution of the organic semiconductor is drop-cast onto the source and drain electrodes. The crystal formation completes the fabrication of a transistor (gold gate, parylene gate insulator, gold source and drain electrodes, Alq_3 or rubrene semiconductor). The crystal morphology is controlled by the solution concentration, the vapor concentration, and the vapor exposure time. Also, the anisotropic mobility should be considered to fabricate organic semiconductor channel.

The fabrication process is described in Figure 3.4 for parylene based and 3.5 for silicon based devices. The 0.5 μm silicon dioxide layer is grown by thermal oxidation -

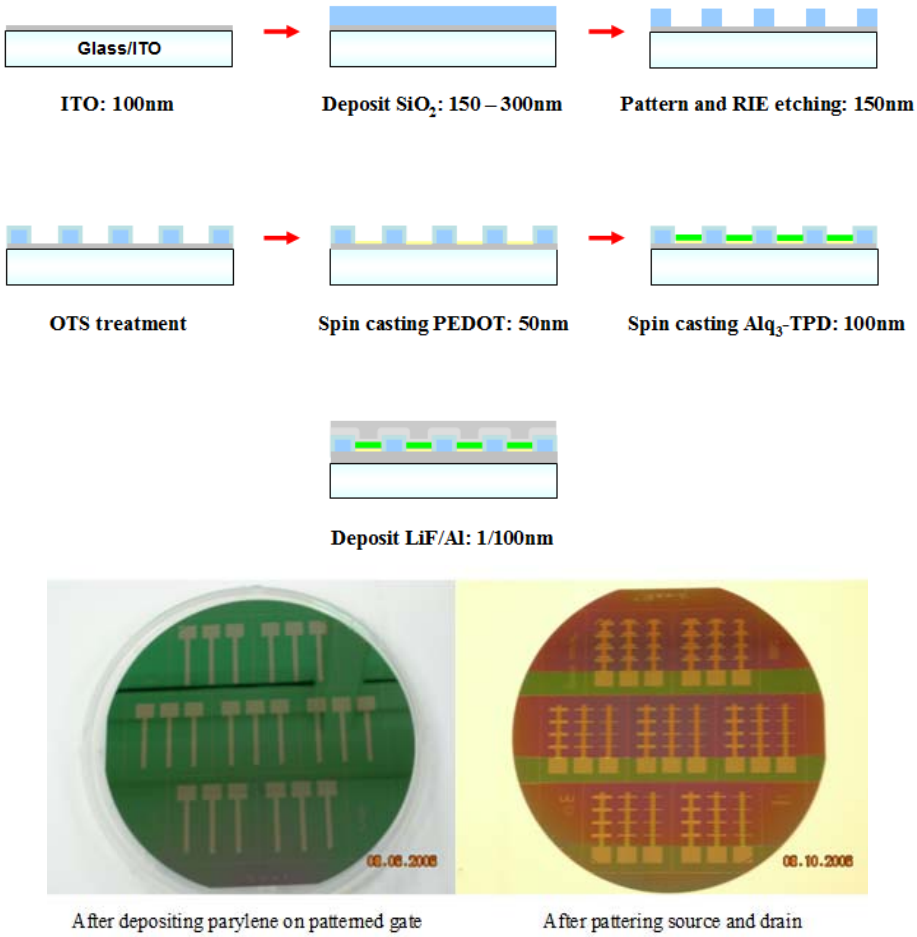

Figure 3.4. Process flow of bottom contact OFETs using parylene dielectric layer.

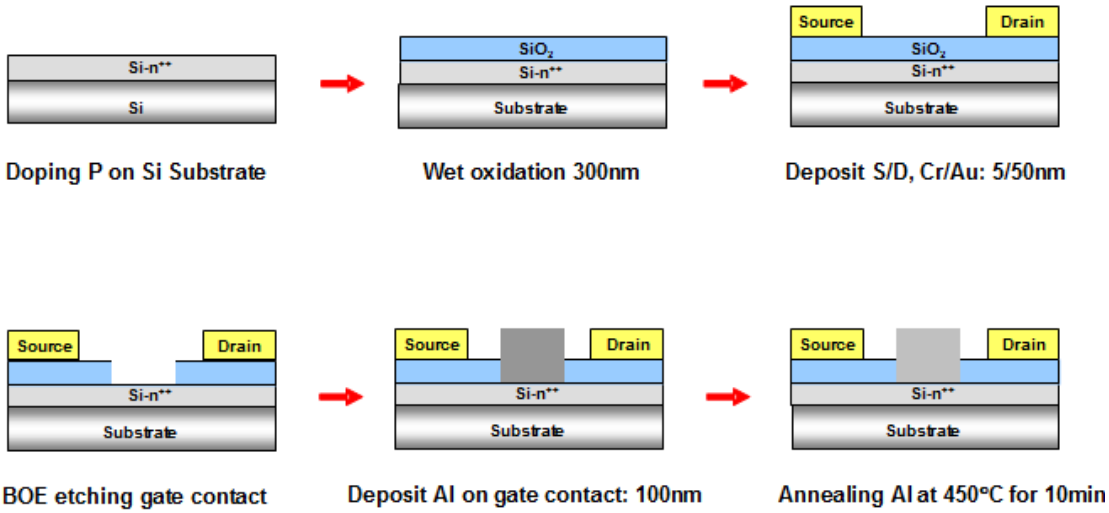

Figure 3.5. Process flow of bottom contact OFETs using SiO_2 dielectric layer.

as a bottom insulator. The SiO_2/Si wafers are cleaned via standard cleaning recipe as follows by sequential ultrasonic rinse in acetone, methanol, isopropyl alcohol, and DI water. A thin film of parylene C is chosen as the bottom insulator and the dielectric material. This material forms transparent pinhole-free conformal coatings as thin as 0.1 μm with excellent dielectric and mechanical properties.

The SiO_2 wafer is treated by oxygen plasma (Oxford plasmalab80) for 1 min to build up silanol group on the surface. The wafer is modified with silane A174 for 2 hrs to increase surface affinity with parylene layer. The parylene is deposited onto the SiO_2 wafer for 3μm as a bottom insulator and buffer layer. The source and drains are patterned by photolithography using Shipley 1813 positive photoresist and then developed with Shipley 352 developer. Cr/Au/Cr layers are evaporated (Temescal BDJ-1800 electron beam evaporator) on patterned substrate for 5 nm (0.5 nm/s), 20 nm (50 nm/s), 5 nm (0.5 nm/s), respectively, defining the gate electrode. The parylene is deposited onto the gate patterned SiO_2 wafer for 0.5 μm as a dielectric layer. The source and drains are patterned by photolithography. Source and drain layers are deposited onto patterned dielectric parylene layer (Cr/Au: 5 nm/20 nm, respectively) and then the layers are lift off to define the patterning area. The fabricated transistor is placed in the jar and then the solution is drop cast on the channel. The solution is crystallized by solvent vapor recrystallization.

3.2.5. Measurement of Electrical Properties

The charge carrier mobility can be estimated as follows. The capacitance of the gate electrode per unit area, C_i, is measured for test capacitors, $C_i = \pm 0.2$ nF/cm^2,

($C = \frac{A\varepsilon_0\varepsilon_r}{d}$), for parylene dielectric film (HP 4284A Precision LCR meter, 100 Hz, 2 V bias). Current-voltage measurements are performed using a semiconductor parameter analyzer (Agilent 4156C). These measurements show characteristic transistor behavior with resolved linear and saturation regimes. At low V_D, I_D increases linearly with V_D (linear regime) and is approximately determined from the following equation[95]:

$$I_D = \frac{WC_i\mu}{L}\left(V_G - V_T - \frac{V_D}{2}\right)V_D \tag{3-1}$$

where L is the channel length, W is the channel width, C_i is the capacitance per unit area of the insulating layer, VT is the threshold voltage, and μ is the field effect mobility, which can be calculated in the linear regime from the transconductance,

$$\mu = \frac{\partial^2 I_{SD}}{\partial V_{SD} V_G}\frac{L}{CW} \quad \text{or} \quad \mu = \left(\frac{L}{WC_i V_{SD}}\right)\left(\frac{dI_{SD}}{dV_G}\right) \tag{3-2}$$

for saturation regime, μ can be calculated from the slope of the plot of $\sqrt{|I_D|}$ versus V_G,

$$I_D = \frac{WC_i\mu}{2L}(V_G - V_T)^2 \tag{3-3}$$

3.3 Results and Discussion

5,6,11,12-tetraphenylnaphthacene (rubrene) has been studied widely in optical,[96] morphological,[97] and electrical properties[98] because the rubrene crystal provides efficient

ways to study intrinsic charge transport phenomenon. Rubrene has four twisting phenyl side groups on tetracene backbone. Although tetracene forms triclinic, one of tetracene derivative, the rubrene mostly forms orthorhombic crystalline structure. This phase shifting suggests that the crystalline structure of rubrene can be altered by controlling crystal growing methods and conditions.

3.3.1. Solvent Vapor Recrystallization

The crystallization technique is based on solvent vapor diffusion into organic material, reorienting molecular distance among neighbor molecules and surface interactions between solvent, organic molecule, and substrate.

In the SVR technique, an organic material (in saturated solution) is placed on a substrate and subsequently exposed to solvent vapor in a closed environment. Numerous conditions affect the morphology and form of the resulting in-plane crystals, including the polarity and concentration of the solvent, temperature and pressure, time of exposure, and hydrophilicity/hydrophobicity of the substrate. Rubrene is dissolved in chloroform and dropped onto the substrate by a microsyringe. Exposure to the polar solvent methanol or nonpolar solvents chloroform and toluene is carried out at room temperature and atmospheric pressure. Solvent vapor exposure times range from 1 hr to 1 week. Figure 3.6 shows the optical micrographs of polycrystalline morphology. The saturated rubrene solution was dropped on silicon substrate in air out of solvent vapor system.

Figure 3.7 shows optical micrographs of rubrene crystals grown in methanol and chloroform vapor ambients at different exposure times. Note that, in contrast, air ambient produces a polycrystalline structure. Rubrene forms small sapphire shaped -

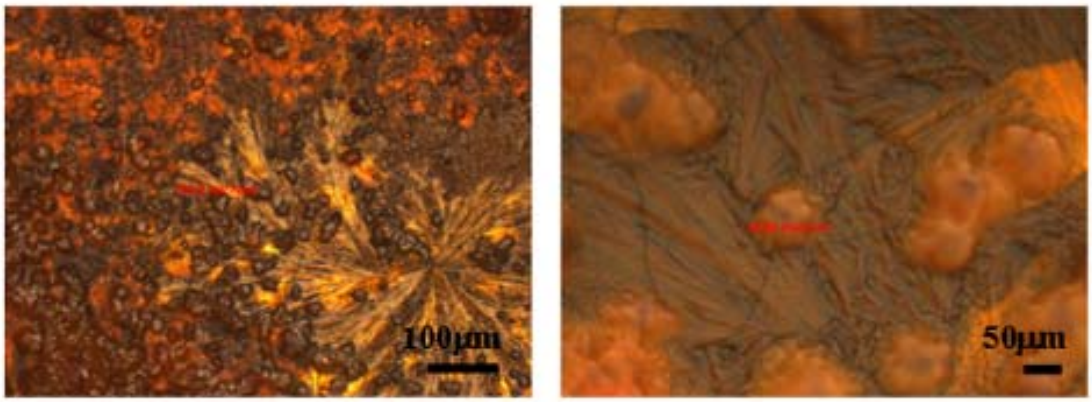

Figure 3.6. Optical microscopy images of rubrene polycrystalline structures grown by solvent vapor recrystallization in air.

crystals after 1 hr of solvent vapour exposure in both methanol and chloroform, with average size about 50-100 μm. These crystals begin to branch and form needle-shaped filaments. After this point, there is a significant difference between methanol and chloroform in that, after about 12 hrs exposure to chloroform, distinct rod-like crystals begin to form.

Toluene ambient showed similar behavior to grow decent single crystals. This ambient of toluene vapor produces formed yellowish-orange crystals on silicon wafer. The crystals were grown as big as 3 by 3mm crystals with distinct facets after 1 week (Figure 3.8). The crystals grown for 24 hrs and 1 week showed different crystalline facet, shown by optical microscopy.

Hydrophilic silicon and hydrophobic parylene coated silicon substrates were used. Hydrophobicity of substrate changes interfacial energy between the surface of substrate and organic materials, which result in extension of in-plane single crystals. Figure 3.9 shows decent enlongated crystal on the parylene coated substrate.

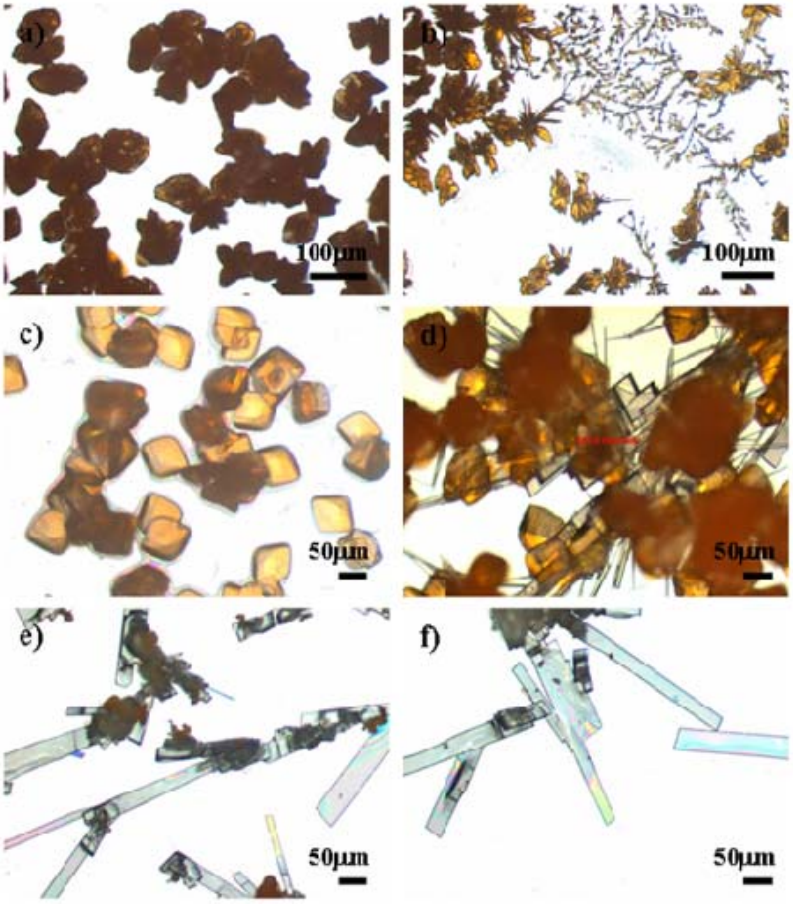

Figure 3.7. Optical microscopy images of rubrene crystals grown by solvent vapor recrystallization in methanol: a) 1hr b) 24 hrs and in chloroform: c) 1hr d) 6 hrs e), 12 hrs f) 24 hrs.

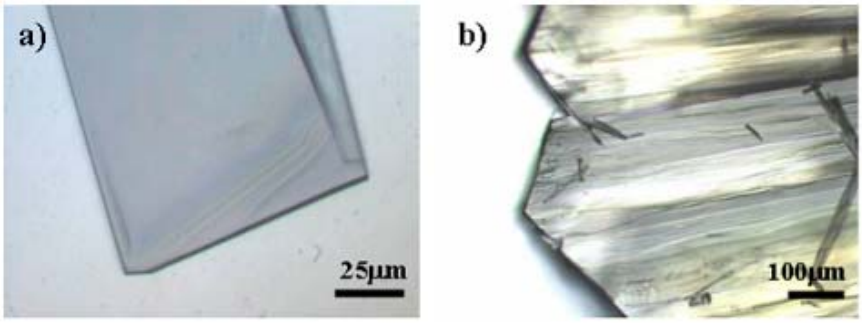

Figure 3.8. Optical microscopy images of rubrene crystals grown by solvent vapor recrystallization in chloroform: a) 24hrs and b) 1 week.

The surface properties of the substrate also offer a unique approach to controlling crystal growth in that a hydrophobic surface can promote formation of larger crystals. This preferential growth can be responsible for surface interactions and surface diffusivities.[99] Parylene is composed of a phenyl backbone, while rubrene has phenyl side groups in the tetracene backbone. These nonpolar chemical structures react favorably to drive nucleation on the surface. Further, the rougher surface of parylene film (with higher surface energy) promotes crystallization as compared to the smooth Si/SiO2 surface.[100]

The initial amorphous film is presumed as a stable fluidic layer with extremely high viscosity. The thin film contacting substrate has two kinds of interactions between molecules in the film and between the molecules and the surface of the substrate.

When the solvent vapor diffuses into the film, the film would start to change physical properties. The film would undergo dewetting in the initial diffusing stage. And then, the wet film would convert to a hydrodynamic stage. Finally, the molecules will begin to reorder molecular stacking and form the crystalline structure.

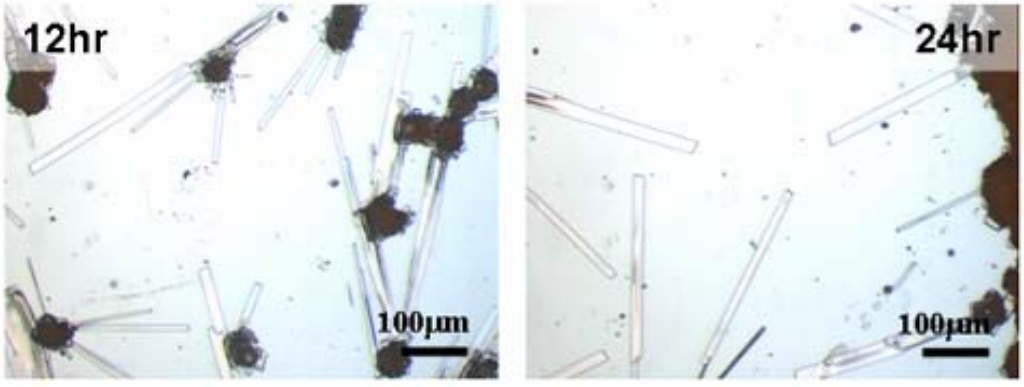

Figure 3.9. Optical microscopy images of rubrene crystals grown by solvent vapor recrystallization in chloroform on parylene substrate.

And then, the wet film would convert to a hydrodynamic stage. Finally, the molecules will begin to reorder molecular stacking and form the crystalline structure. The formation of crystals indicates transition of interfacial force in the three phases. The interfacial energy between rubrene film and SiO_2 hydrophilic substrate ($\gamma_{rubrene\text{-}substrate}$) has low energy. However, the interfacial energy increases as a solvent vapor diffuses into the molecules of the film, while $\gamma_{solvent\text{-}substrate}$ become lower to wet the entire substrate.

In the molecular notion, the static, stability, and dynamics of the thin film are caused by intermolecular forces. The intermolecular interactions are surface tension, van der Waals forces, electrostatic forces, structural forces, and elastic strains between molecule and molecule, and between molecule and surface. All of these interactions are responsible for complex crystallographic dynamics.

Figure 3.10 shows the 2θ X-ray intensity data collected on the rubrene crystals. The crystals grown in chloroform have decent peaks indicating single crystals compared to the crystals grown in methanol showing polycrystalline XRD patterns. We can see that the rubrene crystal grown in chloroform exhibits a structural phase-shifting from 1hr to 24 hrs. Figure 3.11 shows photoluminescence (PL) spectra of rubrene crystal grown in methanol and chloroform. Interestingly, the rubrene crysal grown in chloroform shows optical transition compare to the rubrene crystal grown in methanol. The molecular symmetry and orientation in crystalline structure are mostly responsible for this optical transition.

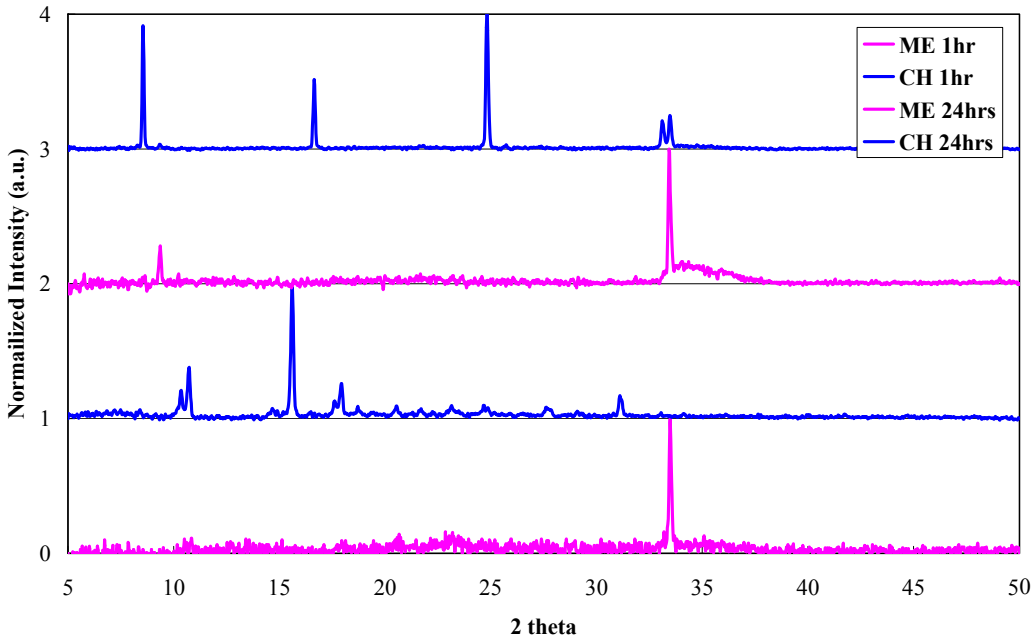

Figure 3.10. XRD 2θ plots of the rubrene crystals grown by solvent vapor recrystallization in chloroform: a) 1hr and b) 6hr, and methanol vapor: c) 1hr and d) 24hrs.

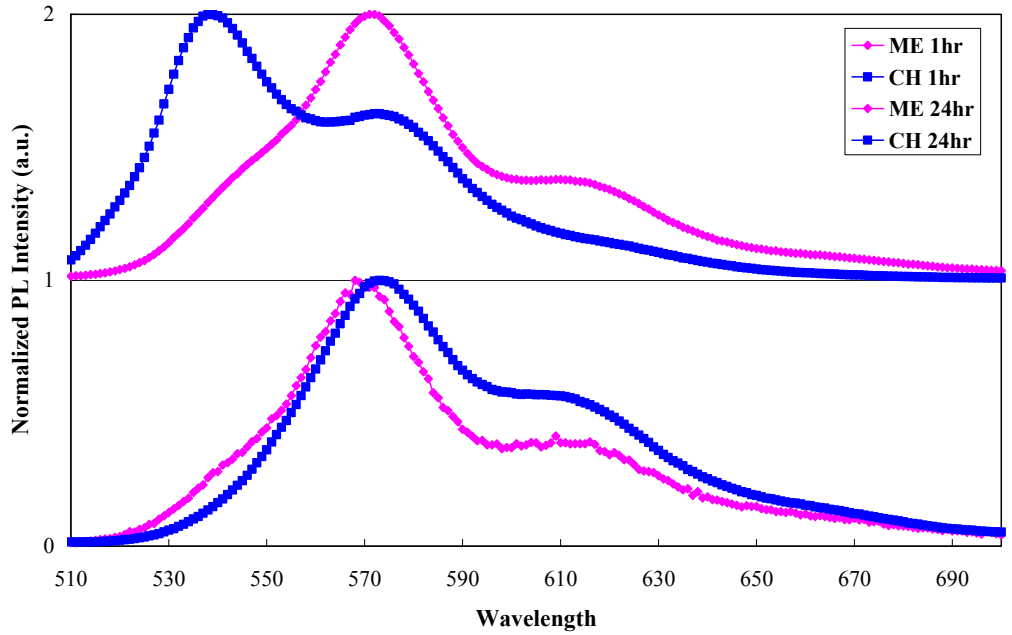

Figure 3.11. PL spectra of the rubrene crystals grown by solvent vapor recrystallization in methanol (Pink) and chloroform (blue) vapors: a) 1hr and b) 24hrs.

3.3.2. Crystal structure

Three polymorphic crystal phases for rubrene have been reported to date. Monoclinic was first reported in 1936,[101] and a triclinic phase was reported in 1962.[102] However, the growing methods were not described and the lattice parameters reported are not consistent with the Cambridge database. The most widely known crystal structure is orthorhombic, first reported in 1971 (a=14.44, b=7.18, c=26.97, α=90°, β=90°, γ=90°)[103], but also in 1983 (a= 7.18Å, b=14.43Å, c=26.89Å, α=90°, β=90°, γ=90°)[104] and 2006 (a= 26.86Å, b=7.19Å, c=14.43Å, α=90°, β=90°, γ=90°). [105] Figure 3.12 shows crystallographic structure of orthorhombic and monoclinic.

For comparison to our crystals grown by SVR, we tested a rubrene crystal grown by physical vapor transport (PVT) in the Optoelectronic Materials Laboratory at the University of Utah, which should take orthorhombic form (note that this crystal has been oxidized in air). The morphological and crystallographic properties of rubrene crystals -

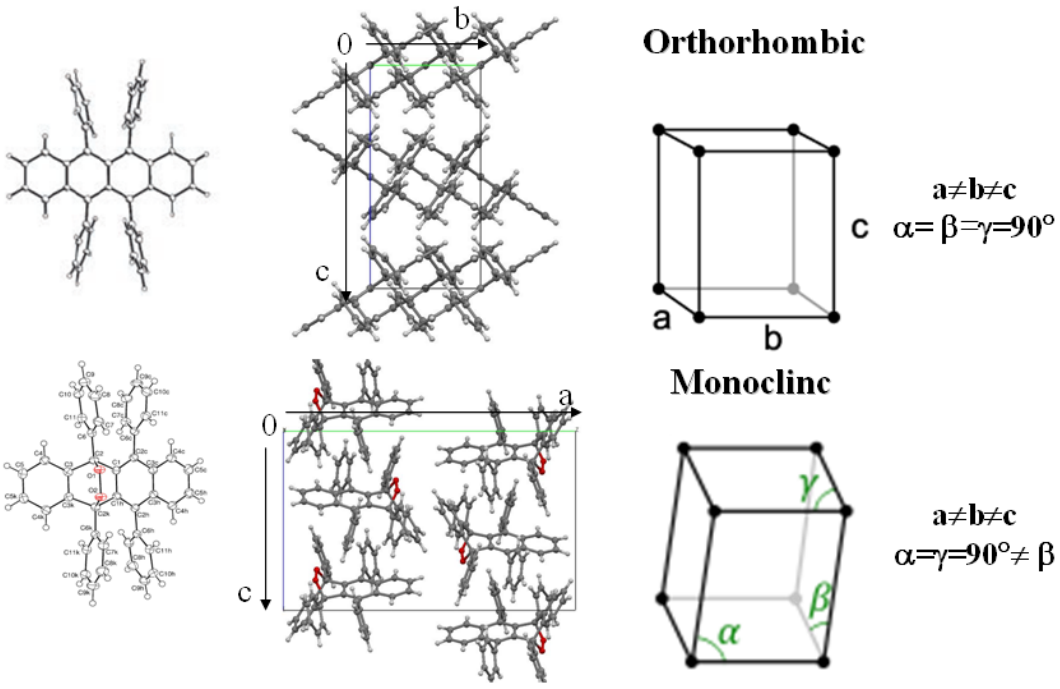

Figure 3.12. Crystallographic structure: top) orthorhombic, bottom) monoclinic.

were determined by X-ray diffraction (XRD); Figure 3.13 shows the 2θ versus X-ray intensity data collected. The SVR rubrene crystal grown in chloroform exhibits a distinct phase change from 1hr to 24 hrs of growth. Neverthless, the oxidized orthorhombic rubrene crystal matches with a previous reported XRD pattern with sharp peak, 7° representing (002) plane and including weak peaks of 12°, 20°, 26°, and 40°. The presence of rubrene peroxide in the orthorhombic crystal does not change the XRD patterns.[106] Also the shifting of photoluminescence implies that there is structural transition in the crystal system. We will discuss further the optical transition related with crystalline transition in the following section. The XRD pattern for the 1 week crystal exhibit totally different patterns compared to pattern of crystal grown by PVT, and has been determined through X-ray crystallography to be monoclinic form.

We rescanned these samples using high resolution XRD in order to obtain specific crystallographic parameters for the different phases (Figure 3.14). The crystallographic parameters for the 1hr crystal are a=21.06, b=17.99, c=14.72, α=90°, β=90°, γ=90° and for the 24 hrs crystal, a=16.86, b=16.86, c=23.64, α=90°, β=90°, γ=90°. The likely crystalline structures are orthorhombic and tetragonal, respectively; however, these crystal structures are likely not single phase because there are hidden small peaks found in high resolution XRD and different lattice parameters from a previous report.

The expected orthorhombic and tetragonal crystalline structures are as shown in Figure 3.15. The crystallographic parameters are summarized in Table 3.1. The monoclinc 1 represents the report in 1936 and monoclinc 2 for monoclinc crystal grown by SVR for 1 week and the orthorhombic 1 presents the report in 2006 and orthorhombic 2 for the crystal grown by PVT in Optoelectronics Lab. The crystallographic data of monoclinc 2 and orthorhombic 2 were obtained by X-ray crystallography.

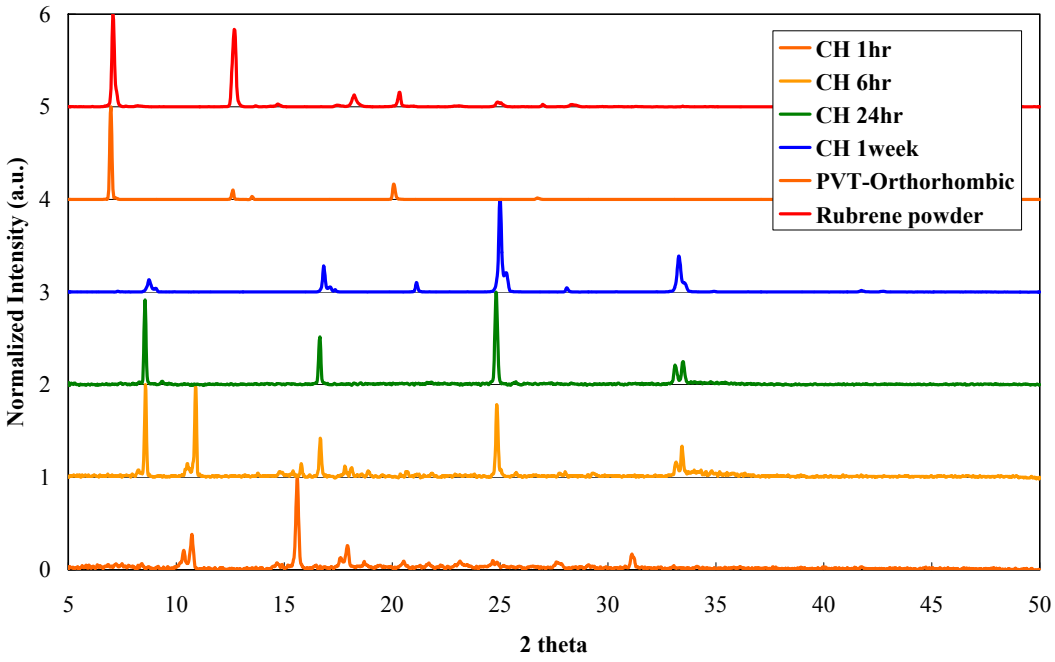

Figure 3.13. XRD 2θ plots of the rubrene crytals grown by solvent vapor recrystallization in chloroform vapor: a) 1hr, b) 6hr, c) 24hrs, d) 1week, and e) oxidized rubrene crysal grown by physical vapor transport, and f) sublimed rubrene power.

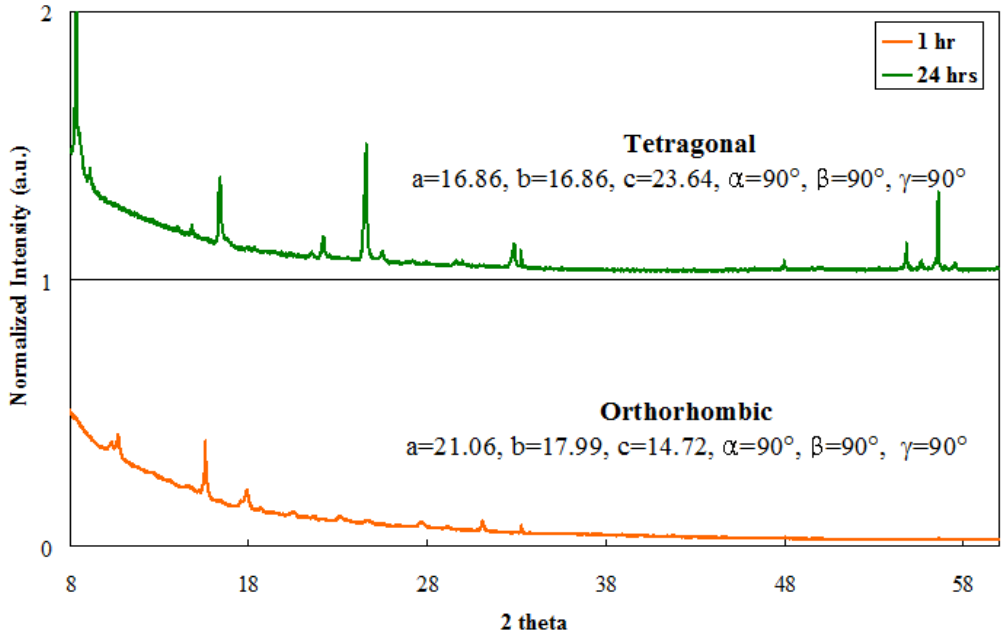

Figure 3.14. High resolution XRD pattern of rubrene crystals grown by SVR: a) 1hr, b) 24hrs.

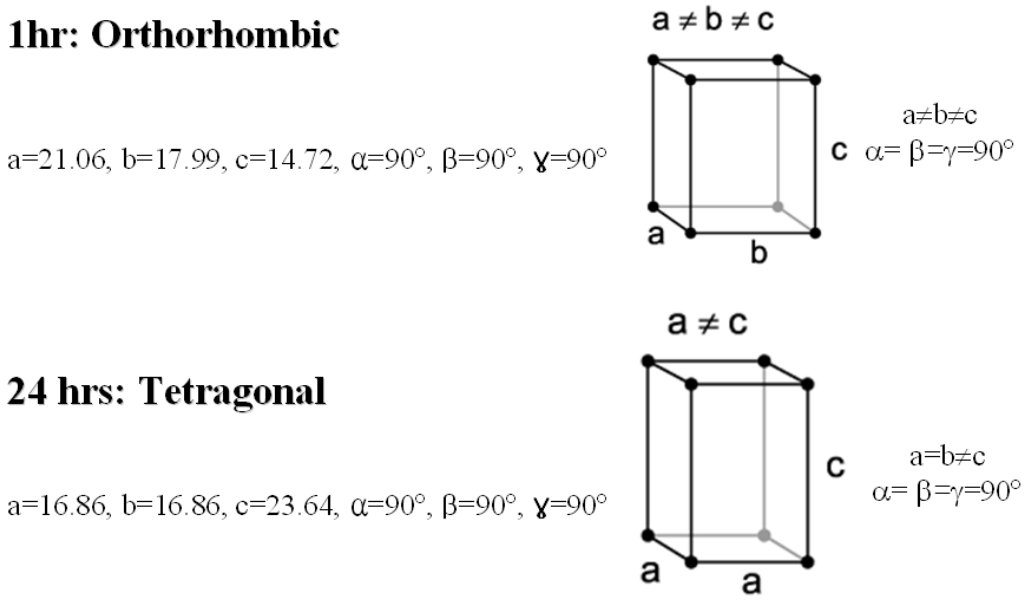

Figure 3.15. Crystallographic structure: top) orthorhombic, bottom) tetragonal.

Table 3.1. Crystallographic parameters for various rubrene polymorphic crystals.

	Monoclinic 1[101]	Triclinic[102]	Orthorhombic 1[105]	Orthorhombic 2	Monoclinic 2
a (Å)	15.5 (17.9)	11.60 (14.65)	26.86	27.74	21.71
b (Å)	10.1 (10.1)	9.15 (9.15)	7.19	7.16	11.16
c (Å)	8.8 (8.8)	7.16 (7.16)	14.43	14.26	13.62
α (°)	90 (90)	105.53 (112)	90	90	90
β (°)	90.55 (120)	112.97 (115)	90	90	103.23
γ (°)	90 (90)	90.98 (52)	90	90	90
V(Å3)	1377	675	2788.51	-	3216
ρ (Mg/m3)	1.284	1.31 (1.23)	1.269	-	1.412

* The crystallographic data of monoclinic, triclinic, and orthorhombic 1 are taken from Cambridge data base and the data in parentheses are taken from the reference paper.

3.3.3. Transition of Crystal Phase

The rubrene has interesting characteristic that absorbs oxygen on photo-irradiation or oxygen diffusion in solution and in solid state, which forms an oxy-rubrene or rubrene peroxide ($C_{42}H_{28}O_2$).[107] The characteristic of oxidation is utilized to create oxygen bond in the rubrene and this bonding can create three types of rubrene peroxide isomers with noticeably different molecular structures.[108] The major formation of rubrene peroxide by photo-oxidation is isomer 1 as shown in Figure 3.16. The rubrene crystal grown by PVT mostly form orthorhombic crystalline structure, and the diffusion of oxygen in orthorhombic crystal does not change crystalline structure, but adds oxygen on the surface of rubrene molecules.[109] The concentration of oxygen gradually decreases from the surface.[110] However, the introduction of oxygen in solution by photoirradiation creates oxygen bonding in tetracene backbone, and provides higher concentration of rubrene peroxide.[111] Figure 3.16 illustrates photooxidation process of rubrene molecule. The rubrene molecule loses electorons by photoexitation and reacts with oxygen under influence of radiant energy.

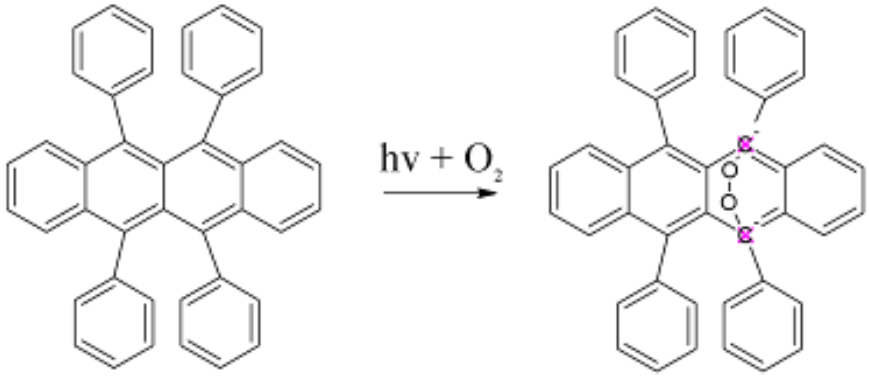

Figure 3.16. Schematic representation of photooxidation of rubrene isomer-1.

The photooxidation of rubrene to form rubreneperoxide follows the simple reaction scheme.[112]

$$R \xrightarrow{h\nu} R'$$

$$R' + O_2 \rightarrow RO_2 \text{ (stable)} + R$$

The detail of reaction scheme is presented as follows. [108,113]

$$\begin{aligned} &{}^1R + h\nu(UV - Vis) \rightarrow {}^1R^* \\ &{}^1R^* + O_2({}^3\textstyle\sum_g^-) \rightarrow {}^3R^* + O_2({}^1\Delta_g) \\ &{}^3R^* + O_2({}^3\textstyle\sum_g^-) \rightarrow {}^1R + O_2({}^1\Delta_g) \\ &{}^1R + O_2({}^1\Delta_g) \rightarrow RO_2(stable) \end{aligned} \qquad (3\text{-}4)$$

This crystallization of rubrene by photo-oxidation was also investigated by comparing two crystals grown in UV filtered room and light exposed room. The crystal grown in an UV filtered room formed a red color cluster, but the crystal grown in light crystallized to a decent single crystal formation with bleached color which proves that crystalline phase change is caused by photooxidation. Figure 3.17 shows chemical structure of pure and oxidized rubrene molecule and crystalline packing viewed from crystallographic down a, b, c-directions.

This rubrene peroxide isomer has two oxygen bondings in tetracene backbone, which is called isomer 1.[114] The addition of two oxygen single bonds in tetracene backbone, C2 and C2k, with dihedral angle 104.69° bends the tetracene backbone 70.43°-

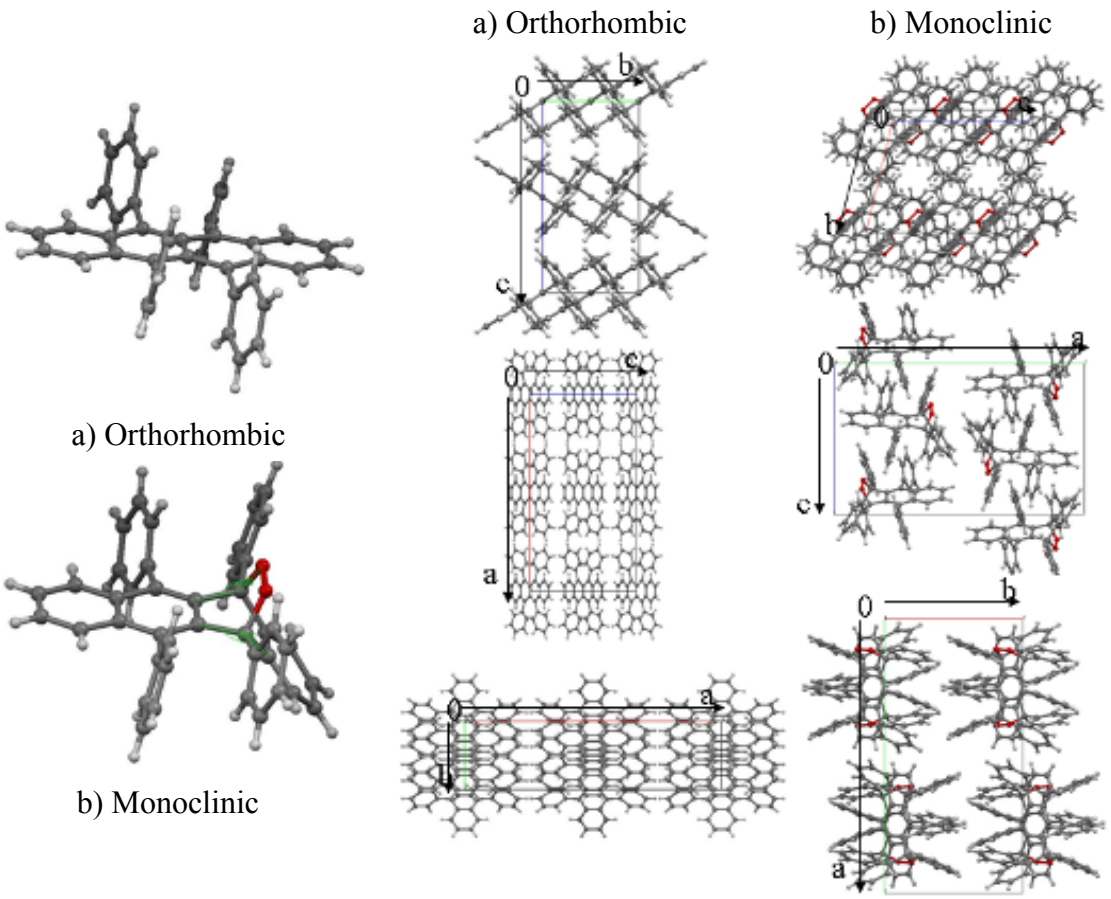

Figure 3.17. Chemical structure of orthorhombic rubrene and monoclinic rubrene peroxide (left); Rubrene crystalline packing structure viewed from crystallographic down a, b, c-directions (right).

and also changes the dihedral angle of 4 phenyl ring side groups. This shift of backbone and diffusion of solvent vapor provides a vacant space between molecules in order to rotate and twist molecules. This change of molecular structure alters molecular ordering and creates a new crystalline structure from orthorhombic to monoclinic. The packing structures of orthorhombic and monoclinc indicate that the orthorhombic structure is highly packed in b-direction and the monoclinic in c-direction. The oxidation of rubrene also shows optical transition of photo luminescence (Figure 3.18).

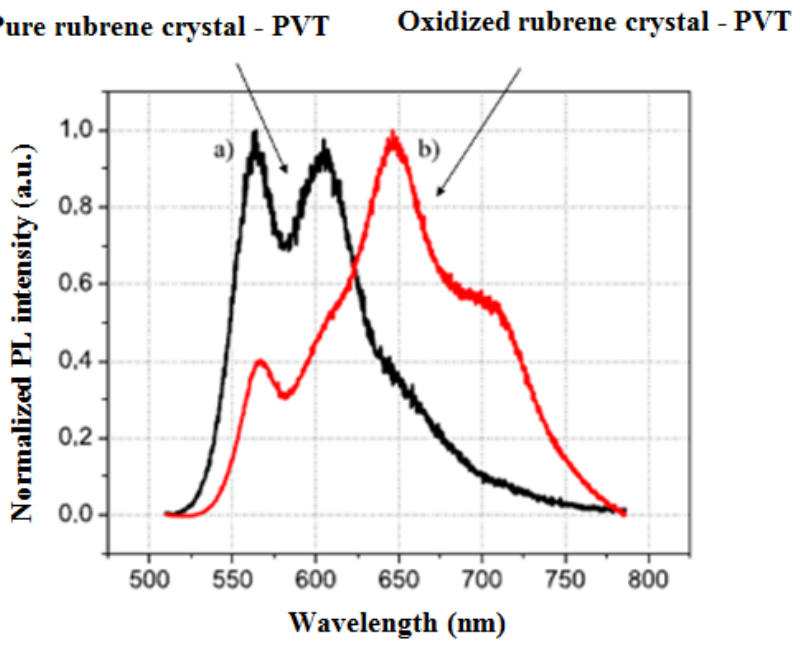

Figure 3.18. PL spectra of a) pure rubrene crystal, b) oxidized rubrene crystal.[115]

3.3.4. Optical Transition

Figure 3.19 shows the photoluminescence (PL) spectra of the rubrene crystals grown in chloroform. The excitation wavelengths are 370 nm for monoclinic, and 470 nm for orthorhombic and intermediate forms. As shown above, the rubrene crystals grown in chloroform vapor ambient exhibited interesting results, which shift crystalline structure and PL emission wavelength. The PL efficiently addresses any structural or chemical changes in ruburene molecules. These PL spectra imply that a change is progressing in the rubrene crystal with optical transition as a function of exposure time.

The orthorhombic rubrene crystal grown by PVT more red-shifts with weaker intensity at typical emission 560 nm than pure single crystal grown by PVT in a vacuum, and shows absence of a ridge.[107] This is because the surface of crystal is oxidized easily in air at room temperature and this oxidation changes an optical transition, generating a -

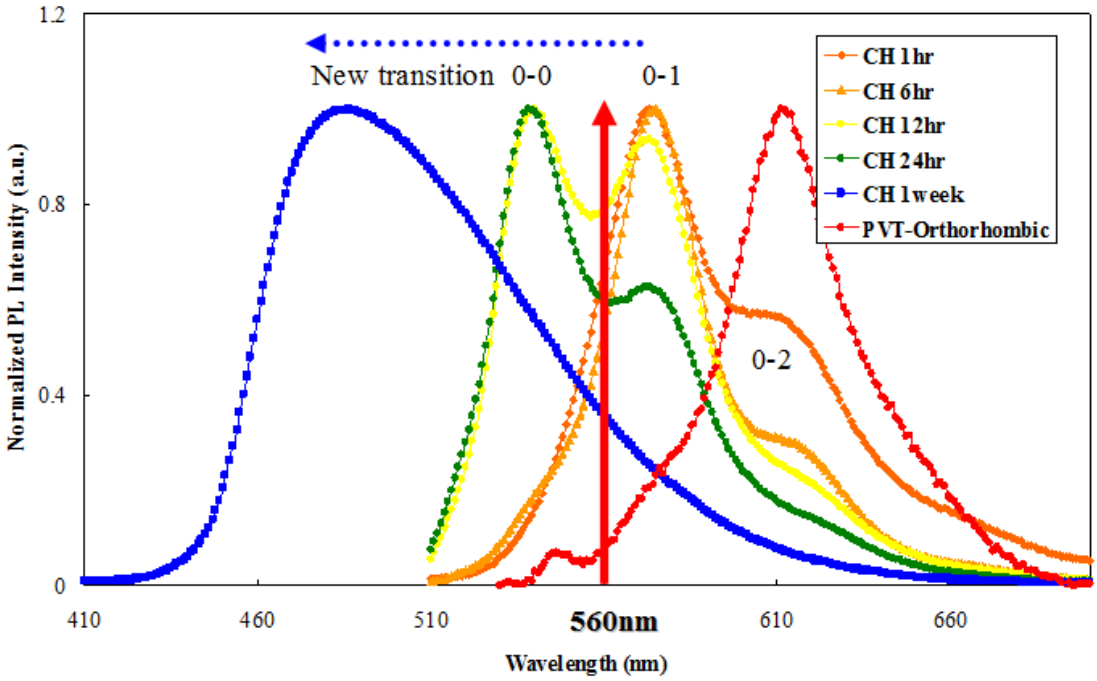

Figure 3.19. PL spectra of the rubrene crystals grown by solvent vapor recrystallization in chloroform vapor: a) 1hr, b) 6hr, c) 12hrs, d) 24hrs, e) 1week, and d) oxidized rubrene crystal grown by physical vapor transport.

new peak at 614, which is caused by the presence of rubreneperoxide on the surface. However, the oxygen related new peak is comparable to the previous report, 640nm because the shifting of the new peak strongly depends on the concentration of rubrene peroxide in the crystal and the exposure of the crystal in air is not sufficient to grow rubreperoxide.[116]

Despite the fact that the monoclinic crystal grown in solution includes much higher concentration of rubreneperoxide in the crystal reaching almost 100%, compared to oxidized rubrene crystal, the monoclinc rubrene crystal after 1 week shows blue shifting with two ridges whose maximum intensities are at 486 and 523 nm. The emission is shifted 128 nm from that of the orthorhombic crystal, whose maximum intensity is at 614

nm. The blue shifting was also observed at 380 nm by excitation 242 nm with rubreneperoxide in solution state.[108]

The transition from 1 hr and 24 hrs is considered as mixture between orthorhombic and monoclinic. We can predict that the 1 hr crystal has more portions of orthorhombic form with and PL spectra and a different lattice parameter that is shrunk in a-direction and stretched in b-direction compared to the orthorhombic crystal grown by PVT. The rough portion of orthorhombic form in 1 hr is estimated about 90% and monoclinc 10% with the peak strength. The PL of 1 hr crystal shows broad red-shifting peak which overlap maximum wavelength of orthorhombic crystal around 614 nm and new peaks around 574 nm. The intermediate form of 6 hrs and 12 hrs shows overlapping around 614nm and decreases gradually with evolution of new peaks around 574 nm which also -

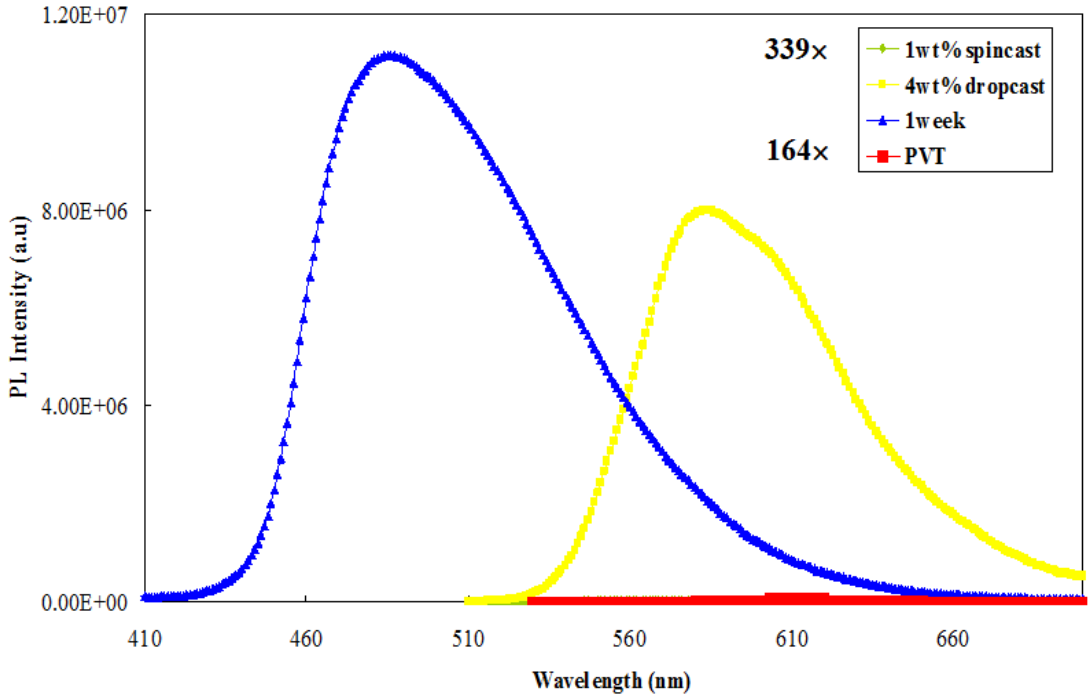

Figure 3.20. Photoluminescence intensity of rubrene crystals grown in different conditions.

gradually increase as the time increases. From 12 hrs, a new peak close to monoclinc 1 week crystal shows up and gradually increases the peak intensity, which enormously proves that the portion of monoclinc is increasing. The PL of 1 week crystal eventually shows complete blue-shifting peak which has broad extension with maximum peaks at 523 nm and 486 nm. The PL peak is broader than other PL spectra, which is cased because the molecular orientation changed the molecular interactions and thermal vibrations.

Another interesting optical behavior of rubrene crystal grown by solvent vapor recrystallizaiton is that the photoluminescence intensity is much higher than that of a crystal grown by physical vapor transport. Figure 3.20 shows PL intensity of thin film of 1wt%, 4wt%, monoclinic crystal (grown by solvent vapor recrystallization), and orthorhombic crystals (grown by physical vapor transport). The arbitary unit intersity is 3.3E4 (1wt%), 7.99E6 (4wt%), 1.12E7 (monoclinic), and 6.82E4 (orthorhombic), respectively.

3.3.5. Optical Properties Related to Crystal Structure and Defect

These PL changes can be explained by structural change or reorientation of molecules as well as molecular and orbital energy values in the growing conditions and any defects in the crystal system. The defects in the organic crystal system can be chemical or structural defects. We can consider that structural and chemical defects in lattice sites modify electronic properties, mostly energy level, and provides an additional pathway of radiative exciton recombination. The structural defect can be lattice deformation, which creates lattice vacancy. This vacancy decreases in its polarization energy and acts as antitrap, which will scatter the carrier without trapping. The

chemical impurities distort the host lattice to produce a vacant orbital in the forbidden energy bandgap to create trap site or act as carrier scattering centers. The presence of impurities is well known defect in organic semiconductor devices and the impurities in organic crystal can be solvent, isomer, or by-product.[117] The oxygen is a major impurity of rubrene and this oxygen diffusion as a dopant provides acceptor state in energy bandgap, and changes charge transport in rubrene crystal which increases hole concentration in the HOMO level. The oxygen impurity in stable state changed the shape of chemical structure and profile of energy bands, which result in formation or prevention of trap.[118] This oxygen bonding changes molecular structure as well as molecular and orbital energy values. The molecular energy bandgap (HOMO-LUMO) changes in α-orbital from 6.26 eV to 7.3 eV, in β-orbital from 6.19 eV to 7.17 eV, and dipole moment from 0.001 debye to 2.548 debye.[114] Even though the oxidation increases the molecular energy gap, the PL of oxidized orthorhombic rubrene shows red-shifting. The orthorhombic crystal is red-shifted because the crystallization mostly alters emission to longer wavelength by organized parallel molecular packing that provides increase of π-π overlapping and eventually produces increase of electronic delocalization. When molecules get closer, molecules form an excited state dimmer by the interaction between an excited singlet state and an unexcited molecule. This formation of excimer affects in emission, which results in broad and red shifting compared to disordered monomer or amorphous thin films. Moreover, the oxygen in the rubrene provides alternative pathways to quench the radiative recombination pathway in the orthorhombic crystal at 600 nm, and creates new more red-shift peak due to trapping of electron in acceptor state.[116]

From this optical transition of oxidized orthorhombic crystal, we should have more red-shifted PL of the monoclinc crystal with higher concentration of rubreneperoxide, but the PL is blue-shifting from 1hr to 1 week. This significant spectral difference between orthorhombic and monoclinc rubrene can be also interpreted by a new formation of crystal system and molecular symmetry and orientation. An intermediate form of the crystal from 6 hrs to 24 hrs exhibits an optical transition to the shorter wavelength. This is due to the allowed optical transition of lowest vibrational energy level that is otherwise disallowed in the single-crystal orthorhombic form. This transition is mostly not shown at room temperature in ambient pressure. In solid state, the intramolecular vibration is an important factor to determine emission wavelength by selection rules, oxcillator strength and energetic position which is governed by molecular packing or crystalline structure. This change is responsible for the interaction of adjacent molecules and crystal lattice parameter, which changes dipole moment. Also the oxygen defect increases molecular energy bandgap and dipole moments. The increase of energy bandgap influence on PL shifting, and the increase of dipole moments allow 0-0 molecular exciton transition to couple to molecular vibration. This phenomenon is described in Figure 3.21.

3.3.6. Charge Carrier Mobility

Rubrene has four twisting phenyl side groups on a tetracene backbone. It has been expected that the side groups reduce π-orbital overlapping, which weakens intermolecular interactions, and eventually drops charge carrier mobility. However, pure rubrene single crystal provided high charge carrier mobility up to 20 $cm^2/V \cdot S$[119] at -

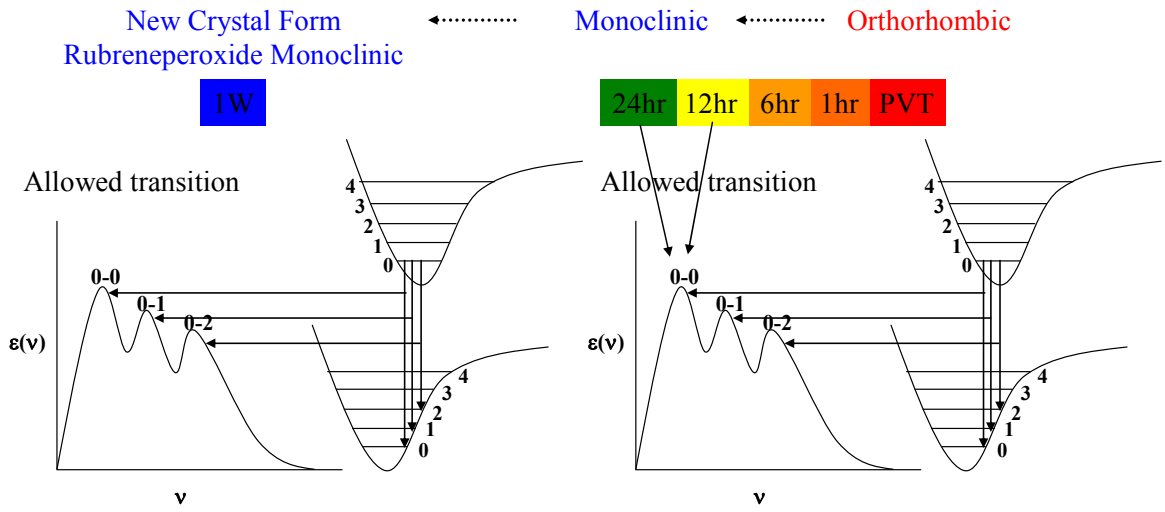

Figure 3.21. Schematic representation of transition to allowed lowest vibrational energy.

room temperature and contact-free intrinsic mobility up to 40 $cm^2/V{\cdot}S$.[120] This result reversed our understanding that conjugated polycyclic aromatic hydrocarbon without bulky side groups increase π-orbital overlap with neighboring molecules and this is a main factor in improving charge carrier mobility. The origin of this high hole mobility has been studied by calculating electronic structure and vibrational reorganization energy in crystallographic axes. The rubrene showed more efficient reorganization energy and electronic coupling compared to tetracene and pentacene due to low-frequency motions of the phenyl side groups. The efficient large electronic coupling was found in the crystallographic b-direction[121] (parallel packing with offset) with cofacial π-stacking interactions, which is in accord with the highest mobility in crystallographic b-direction.[122] Figure 3.22 describes the molecular packing and charge carrier mobility depending on packng structure. The orthorhombic structure (left) shows parallel with offset and 15.4 $cm^2/V.s$ for b axis and 4.4 $cm^2/V.s$ for c axis, while monoclinic structure (right) has more parallel and compact structure rather than orthorhombic structure.

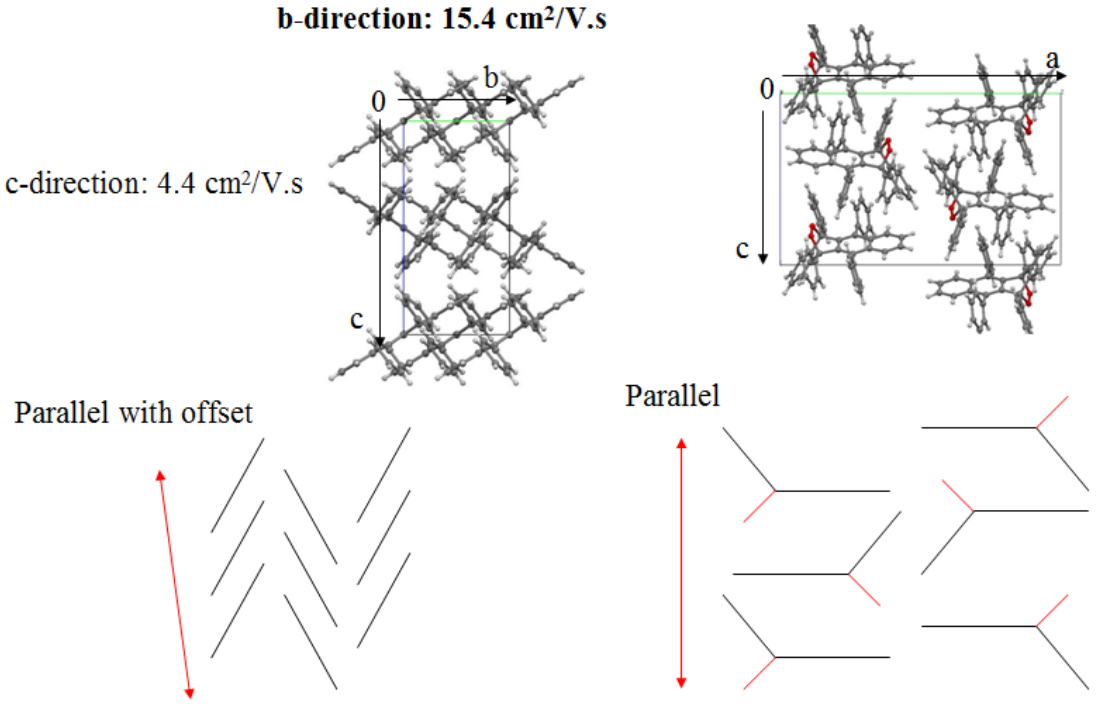

Figure 3.22. Schematics of molecular packing: left) orthorhombic, right) monoclinic.

Based on these results, the main factor to improve electronic properties would be to design a chemical structure, and control molecular packing mode that interact efficiently. A rubrene crystal grown by PVT forms an orthorhombic structure with higher π-π stacking in b-direction and a heringebone motif in c-direction. The phenyl rings form a balanced dihedral angle of 25° because of steric repulsion between the phenyl rings in planar tetracene backbone. A rubrene derivative with tert-butyl side groups in the two bulky phenyl groups, C50H44. 5,11-Bis(4-tert-butylphenyl)-6,12-diphenylnaphthacene formed monoclinic even though grown by PVT. The two side groups changed interplanar separation between two adjacent parallel molecules and twisted backbone, which result in decrease of π-π^* stacking (a=23.52Å, b=9.02Å, c=17.7Å, α=90° β=95.92° γ=90°). [123] The rubrene crystals were also grown by solvent evaporation

recrystallization with toluene, p-xylene, aniline solvents, and 1,2-dichloroethane (DCE) solvent. Those crystals are unlikely to interact with solvents during processes. Those crystals grown from toluene and p-xylene exhibited orthorhombic crystalline structure with the same XRD peaks with rubrene power crystals, and showed charge carrier mobilities up to 0.75 $cm^2V^{-1}s^{-1}$.[124]

The effective charge carrier mobility strongly depends on orientation of crystal on the transistor channel. A single crystal is a solid state in which atoms or molecules are packed in a regular and repeating order in all three spatial dimensions, but there is better packing direction according to crystallographic axes in terms of electronic properties. The strong π-π stacking creates higher electron and hole transport characteristics through channel. Moreover, the lattice constant along the a and b axes and the anisotropic character of inter - and intramolecular vibrational modes are responsible for the improved electronic properties. The p-type rubrene crystal is orthorhombic with herringbone molecular packing. The strong anisotropy of the field effect mobility occurs within the a-b plane of single crystals of rubrene. These excellent properties are derived from the wetting contact between laminated rubrene and paryelene dielectric interface, and high purity of rubrene crystal indicating the importance of crystalinity of organic semiconductor material and the crystal orientation.

The highest mobility would be obtained by molecular packing in the c axis of rubrene crystal due to compact packing in the direction. Figure 3.23 shows molecular packing in a different side of view. The c axis is clearly seen to have compact packing compared to a and b axis. Needle like crystal formed with chloroform solvent ambient for 12 hrs would offer higher mobility since the crystal was completely wet between source and drain.

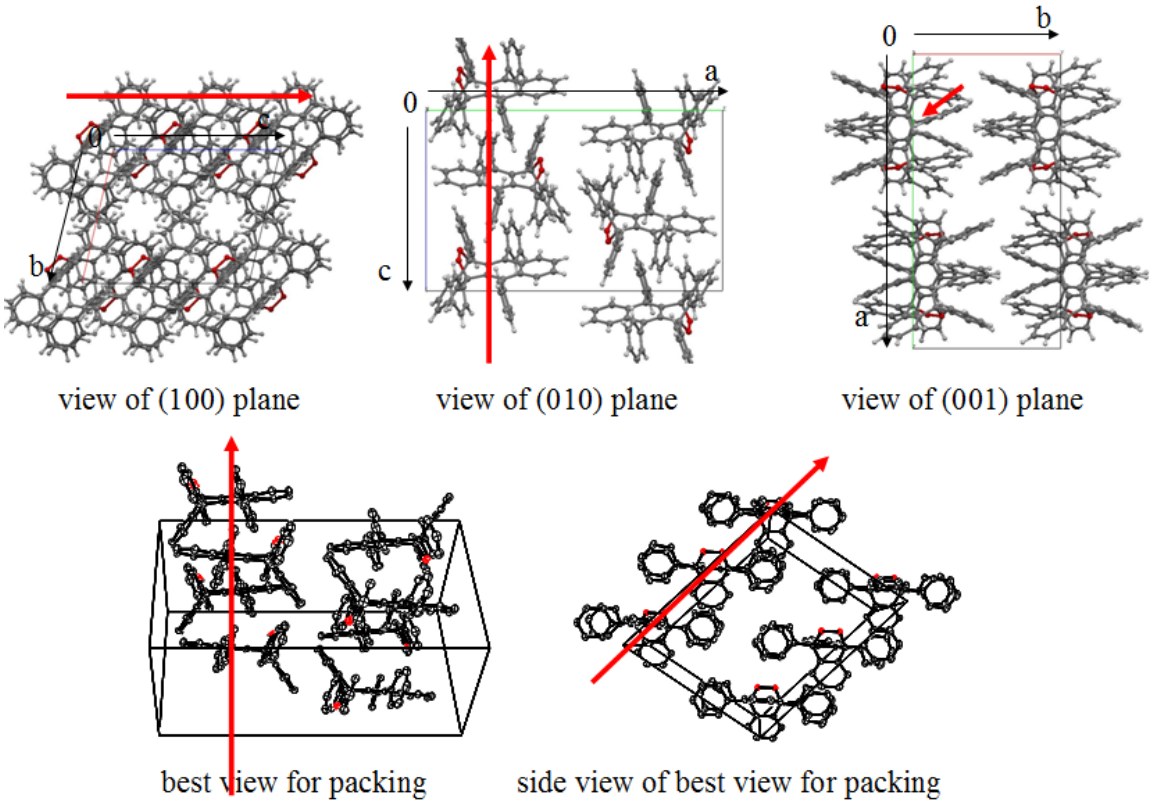

Figure 3.23. Rubrene monoclinic packing structure viewed from different angles.

The close packing is also dependent on the distance of molecules shows molecular distance and molecular distance of pentacene (left), rubrene (right, orthorhombic), and rubrene (down, monoclinic) are described in Figure 3.24. The monoclinic structure has molecular distance; 0.23Å, 0.56Å, and 6.8 Å in a, b, and c directions, which proves that the monoclinic structure is better packed than pentacene and orthorhombic rubrene crystals.

In addition, a high density of peroxide could modify transport characteristics and increase conductivity in oxygen related band. Despite the fact that the impurities in polymer increase the conductivity by improving high density of hopping states, the impurities in small molecular crystal have a negative effect in charge carrier mobility by -

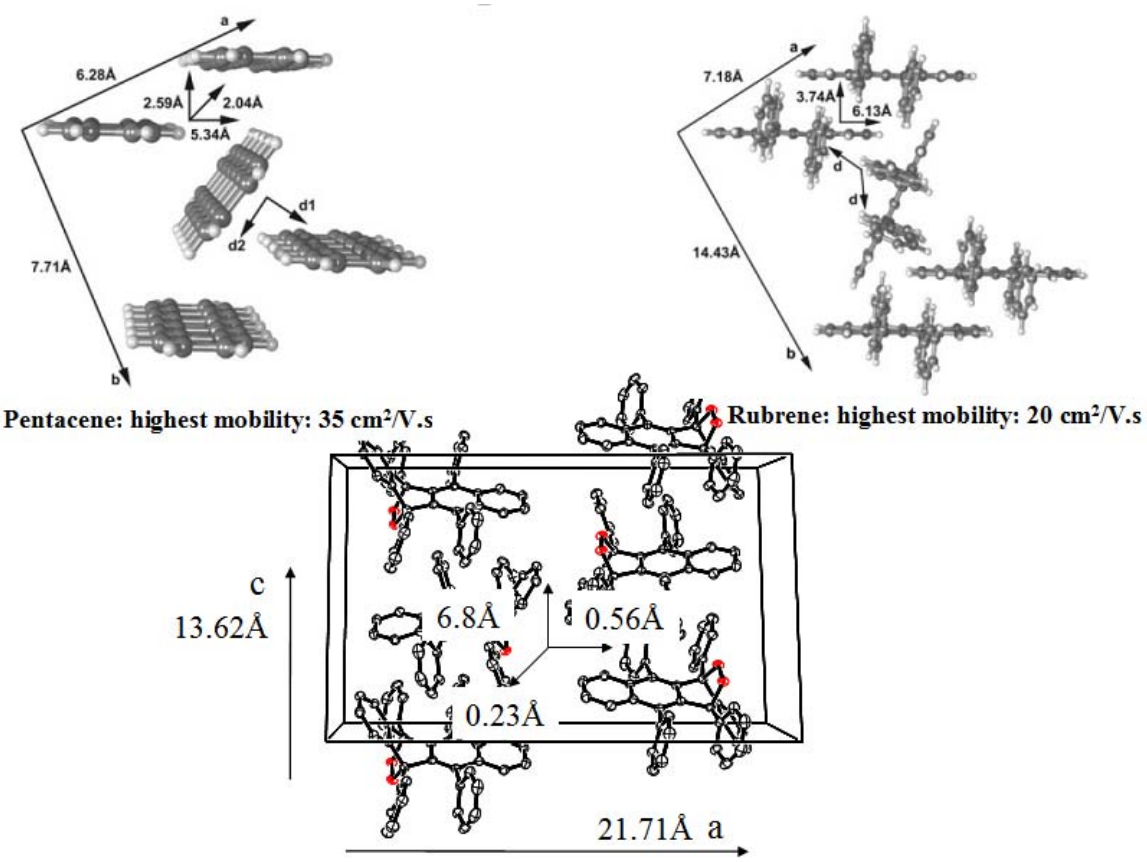

Figure 3.24. Molecular distance in a crystalline packing; left) pentacene, right) rubrene, orthorhombic, down) rubrene, monoclinic.

creating traps.[125] However, the oxygen was introduced by annealing in oxygen ambient to study doping effect, and the oxygen increased carrier density at equilibrium and reduced threshold voltages without mobility change in the on current state.

CHAPTER 4

CONCLUSIONS

As mentioned, the development of micro- and nanoscale patterning techniques for organic materials, especially for small molecules, remains a significant research challenge because advanced patterning techniques for submicron pixels may enable exceptional OLED performance in high resolution micro- and nanodisplays and decrease manufacturing cost.

In summary, in this research a solution-based patterning technique is demonstrated for fabricating high resolution Alq3 OLED pixels based upon spin-casting combined with a structured surface consisting of etched channels or wells. This method achieves precise pixel placement and geometry, and long-range order dictated by photolithographic methods. This patterning technique formed uniform amorphous films with small molecules, which is a critical condition for OLED performances. This result indicated that small molecules can be deposited by solution based spin-casting method rather than typical thermal evaporation, which is commonly used for depositing small molecule materials. The amorphous film property is proved by AFM, XRD, PL that the film shows good surface coverage and uniformity without crystallization.

Also, we discovered that this hydrophobic surface treatment changing interfacial energy can control molecular aggregation. The structured surface is modified with OTS, which serves to direct solution into the etched areas (pixel patterns).

The Alq3 based OLED with PEDOT layer as an hole injection layer reduced the turn on voltage and made linear current injection due to lower energy barrier as published previously.[86] This directed self-assembly technique is applied in the fabrication of active bottom-emitting OLED by spin-casting technique. The patterned OLEDs operated in a higher current density compared to flat thin film devices and performed higher electroluminescence intensity at lower applied voltages. This result implied that the geometrical change improved efficiency of light-output or hole injection is improved by embedding OTS layer. This low refractive index patterning with a combination of spin-casting method may result in higher current density and provide higher electroluminescence intensity and improvement of out-coupling efficiency.

In general, this result suggests that the patterning technique could produce submicron pixels, which would make it possible to manufacture nanodisplays in a simple patterning technique. Also this technique should also be compatible with conjugated polymers[73,126] and may offer a promising solution to front-end patterning of molecular organic semiconductors for high resolution large area, low cost display applications.

We demonstrated a solution-based novel growing technique of rubrene single crystal. The solvent vapor transport technique enables the rubrene molecule to form a desired crystalline structure by crystalline phase shifting by controlling the polarity of solvent vapor and exposure time. We also showed a new crystalline structure of rubrene peroxide crystals, which is not possible to grow with other known methods such as physical vapor transport. Interestingly, this new crystal formation occurred only in the chloroform vapor ambient. This new monoclinc crystal exhibited crystalline phase shifting as well as optical transition to the lowest vibrational energy level that is otherwise disallowed in the single crystal orthorhombic form. The transformation of

crystalline phase is proved by High resolution X-ray diffraction (XRD) and photoluminescence (PL). Also, the new crystal growing technique enables the growth of a high concentration of rubreneperoxide in the crystalline structure by photo-irradiation or oxygen diffusion. This optical transition is basically due to transformation of molecular symmetry and orientation, which changes molecular and orbital energy level, providing additional pathway of radiative exciton recombination. This new crystalline formation with high concentration of rubrene peroxide has a potential to be utilized in optoelectronic devices for higher mobility because the rubrene peroxide increases conductivity on built-in surface conduction channel. The structural symmetry simulation of XRD offered that the highest mobility would be obtained by molecular packing in the c axis due to compact packing in the direction. Moreover, this solution-based new crystallization technique enables a direct crystal growing method on a desired position of an optoelectronic device without any damage or deformation.

CHAPTER 5

FUTURE WORK

First of all, we need to better understand the role of OTS on the electrical device properties, and further efforts to improve device performance are needed. It should be noted that OTS is a well-known gate dielectric layer for OTFT's.[127] The functional role of OTS in this fabrication method is as a hydrophobic layer,[128] so organic monolayers with other terminal ends should be investigated for possible improvements in device performance.

As mentioned, spreading coefficient 'S' determines wettability of a organic film related interfacial energy and equilibrium contact angle, so the contact angle of chloroform on OTS layer should be further studied to investigate the physical mechanisms of surface interactions in the dewetting system, which drives the directed self-assembly of organic small molecules.

The EL showed red-shift compared to PL of spin-cast Alq3. This change of emission wavelength needs to be studied in order to determine whether the mixing of two molecules (Alq3 and TPD) or OTS layer affects this change and whether this effect has an influence on improved device performances. This can be studied by changing ratio of Alq3 and TPD in the mixed solution, which will form different concentrations of molecules in the active film.

The role of OTS in OLED is not fully understood, whether the OTS layer increases or interrupts hole injection, and if this high density of OTS nanolayer functions to prevent electrical shorts. Therefore, the improvement of current density with patterned device structure needs to be studied whether the higher density of molecules in the segregated film or OTS layer induced better charge injection and transport by modifying surface interface or reduction of resistance between organic and inorganic interface.

The outcomes of stronger EL intensity need to be further studied by investigating quantum efficiency to determine whether the patterning with low refractive index or higher density of molecules in the film or OTS layer improved this EL efficiency. We will further study EL efficiency by defining turn on voltage and calibrating luminance meter in an integrating sphere.

The nano- or submicron pixels could provide higher EL intensity due to optical confinement. The electrical efficiency caused by optical confinement effect will be investigated as the pixel sizes are reduced from micron to nanometer size. The ratio between total girth and area of 500 nm pixels will be much larger (8/1) than that of 100 micron pixels (1/25), and pixel density of nanometer pixels is much larger (6.5×10^{8}/inch^2) even though total pixel area are same for OLEDs of all pixel sizes ($2.5\times10^{7}\mu m^2$). If OLED pixel size reduces to smaller than the pixel size of microdisplays, OLEDs begin to show larger EL intensities caused by the optical confinement effect of photons in the submicron sized OLED array.[129] We hypothesize that nanometer size pixels will show unique emission properties (higher EL intensity) in a confined emitting area surrounded by an insulating wall due to the optical confinement effect of photons, caused by the interactions between the transition dipole moment of an

excited molecule in one dimension and its surroundings, leading to: 1) increase of localization and density of state, 2) decrease of luminescence life time due to nanoscale confinement, resulting in faster spontaneous emission.[130]

It is still now fully understood why the allowed transition is occurred with crystalline phase change. The study of molecular and orbital energy is needed to investigate optical transition. This study will prove whether this transition is caused by crystalline defect or molecular aggregate effect. This transition of physical mechanisms can be studied by investigating surface energy, interfacial energy, and glass transition temperature, while vapor annealing time increase gradually. The experiments will seek to verify the hypothesis by observing surface energy of the substrate by contact angle, glass transition temperature of organic semiconductors by thermo-gravimetry analysis (TGA), and by varying experimental conditions: solvent vapor exposure time and vapor annealing temperature.

This nondestructive and reversible crystallization technique enables further study of optical and electrical properties with different directions of plane and angles without processing defects. The crystal on the electrodes can be replaced and rotated into different axis onto dielectric layer between source and drain electrode. The flexibility of both dielectric and the substrate enables assembly of organic crystal and elastomeric stamp surface by van der Waals forces causing a wetting. Figure 5.1 describes the way to measure electrical performances as crystallographic direction. This fabrication technique enables nondestructive and reversible ways to organic layer to build up the OFET structure and to study anistropic charge transport.

The charge carrier mobility can be studied based on the XRD result of packing direction according to crystallographic axes. The photoluminescence with different -

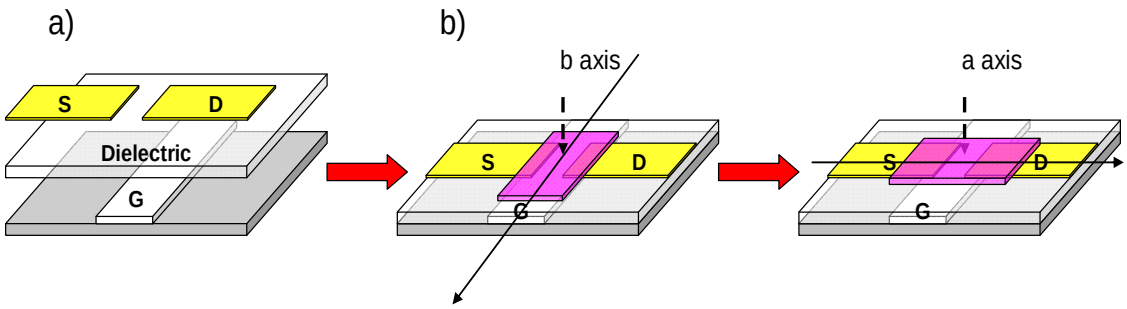

Figure 5.1. Schematic representation of soft lamination technique, a) Gate, dielectric, and source/drain electrodes deposition on parylene, b) transistor fabrications by lamination of an organic crystal onto source/drain electrodes as crystallographic directions.

plane and angles need to be studied to verify the molecular conduction in the crystal system and PL efficiency in different direction. This study will provide critical information on molecular and orbital energy for advanced optical applications such as lasers, photodetectors, and optical modulators and electronic applications such as OFET, RFID and sensors.

REFERENCES

1. 1) J. R. Sheats, H. Antoniadis, M. Hueshen, *Science* **1996**, *273*, 884.
   2) L. J. Rothberg, A. J. Lovinger, *J. Mater. Res.* **1996**, *11*, 3174.
   3) U. Mitschke, P. BaEuerle, *J. Mater. Chem.* **2000**, *10*, 1471.
   4) L. S. Hung, C. H. Chen, *Mater. Sci. and Eng.* **2002**, *39*, 143.
   5) N. K. Patel, S. Cina, J. H. Burroughes, *IEEE* **2002**, *8*, 346.
   6) J. Bardsley, *IEEE.* **2004**, *10*, 3.
   7) C. Wu, C. Chen, C. Lin, C. Yang, *J. DISP. Tech.* **2005**, *1*, 248.

2. 1) H.G.Lohmannsroben, *Appl. Phys. Lett. B.* **1998**, *47*, 195.
   2) G. Kranzelbinder, E. Toussaere, J. Zyss, A. Pogantsch, E. W. J. List, H. Tillmann, H. Horhold, *Appl. Phys. Lett.* **2002**, *80*, 716.
   3) W. Huan, X. ZengQi, M. YuGuang, S. JiaCong, *Sci China Ser B-Chem.* **2007**, *50*, 433.

3. P. Peumans, V. Bulovic, S.R. Forrest, *Appl. Phys. Lett.* **2000**, *76*, 2650.

4. S.R. Marder, J.W. perry, C.P. Yakymyshyn, *Chem. Mater.* **1994**, *6*, 1137.

5. 1) A. Tsumura, H. Koezuka, T. Ando, *Appl. Phys. Lett.* **1986**, *49*, 1210.
   2) Y.Y. Lin, D.J. Gundlach, S.F. Nelson, T.N. Jackson, *IEEE Trans. Electron Dev.* **1997**, *44*, 1325.
   3) H.E. Katz, Z. Bao, *J. Phys. Chem. B.* **2000**, *104*, 671.
   4) C.D. Dimitrakopoulos, P.R.L. Malenfant, *Adv. Mater.* **2002**, *14*, 99.

6. 1) K. Liao, *Tech. rep. DisplaySearch,* **2008**.
   2) M. Fihn, *USDC and Needham and Company Boston Display Investor's Conference* **2001**.

3) D. Hsieh, *Shanghai Intl. Industry Fair* **2005**.

7. H. Klauk, *Organic Electronics: Materials, Manufacturing and Applications*; Wiley-VCH, 2006.

8. 1) J. R. Sheats, H. Antoniadis, M. Hueshen, *Science* **1996**, *273*, 884.
   2) L. J. Rothberg, A. J. Lovinger, *J. Mater. Res.* **1996**, *11*, 3174.
   3) U. Mitschke, P. BaEuerle, *J. Mater. Chem.* **2000**, *10*, 1471.
   4) L. S. Hung, C. H. Chen, *Mater. Sci. and Eng.* **2002**, *39*, 143.
   5) N. K. Patel, S. Cina, J. H. Burroughes, *IEEE.* **2002**, *8*, 346.
   6) J. Bardsley, *IEEE.* **2004**, *10*, 3.
   7) C. Wu, C. Chen, C. Lin, C. Yang, *J. DISP. Tech.* **2005**, *1*, 248.

9. S. R. Forrest, *Nature* **2004**, *428*, 911.

10. 1) J. R. Sheats, H. Antoniadis, M. Hueshen, *Science* **1996**, *273*, 884.
    2) H. Aziz, Z. Popovic, N. X. Hu, C. Tripp, *Appl. Phys. Lett.* **1998**, *72*, 756.
    3) V. Bulovic, S. R. Forrest, *Electroluminescence* **2000**, *65*, 1.

11. R. Wisnieff, *Nature* **1998**, *394*, 225.

12. B. Crone, A. Dodabalapur, A. Gelperin, A. J. Lovinger, Z. Bao, *Appl. Phys. Lett.* **2001**, *78*, 2229.

13. C. J. Drury, C. M. J. Mutsaers, M. Matters, D. M. Leeuw, *Appl. Phys. Lett.* **1998**, 73, 108.

14. 1) Katz, H. E. and Bao, Z. *J. Phy. Chem B,* **2000**, *104*, 671.
    2) Lin, Y. Y., Gundlach, D. J., Nelson, S. F. and Jackson, T. N. *IEEE.* **1997**, ***44***, 1325.
    3) G. Horowitz, *Adv. Mater.* **1998**, *10*, 365.
    4) B. C. Shekar, J. Lee, S. Rhee , *Korean J. Chem. Eng*. **2004**, *21*, 267.

15. 1) J. Pflaum , J. Niemax, A.K. Tripathi, *Chem. Phys.* **2006**, *325*, 152.
    2) N. Karl, K. H. Kraft, J. Marktanner, M. Mu¨nch, F. Schatz, R. Stehle, H. M. Uhde, *J. Vac. Sci. Technol. A.* **1999**, *17*, 2318.

16. 1) T. Mori, K. Obata, K. Miyachi, T. Mizutani, Y. Kawakami, *Jpn. J. Appl. Phys.* **1997**, *36*, 7239.
2) G. Gu, P. E. Burrows, S. Vankatesh, S. R. Forrest, M. E. Thompson, *Opt. Lett.* **1997**, *22*, 172.
3) V. E. Chong, Y. Park, M. G. Mason, C. W. Tang, *J. Vac. Sci. Technol. A*. **1998**, *16*, 1838.
4) S.T. Lee, X.T. Hou, M.G. Mason, C.W. Tang, *Appl. Phys. Lett.* **1998**, *72*, 1593.

17. 1) V. Podzorov, V. M. Pudalov, M. E. Gershenson, *Appl. Phys. Lett.* **2003**, *82*, 1739.
2) R. A. Laudise, Ch. Kloc, P. G. Simpkins, T. Siegrist, *J. Cryst. Growth*, **1998**, *187*, 449.

18. A. L. Briseno, S. C. B. Mannsfeld, M. M. Ling, S. Liu, R. J. Tseng, C. Reese1, M. E. Roberts, Y. Yang, F. Wudl, Z. Bao, *Nature* **2006**, *444*, 913.

19. M. Mas-Torrent, M. Durkut, C. Rovira, *J. Am. Chem. Soc.* **2004**, *126*, 984.

20. K. C. Dickey, J. E. Anthony, Y. L. Loo, *Adv. Mater.* **2006**, *18*, 1721.

21. Courtesy of Samsung SDI.

22. A. Harkness, *Bright Ideas*, 2004.

23. J. Shinar, *Organic Light Emitting Devices: A Survey*; Springer, 2002.

24. Aldrich, retrieved from http://www.sigmaaldrich.com/chemistry.html.

25. K. Okumoto, H. Kanno, Y. Hamada, H. Takahashi, K. Shibata, *Appl.Phys.Lett.* **2006**, *89,* 013502.

26. 1) H. Choukri, A. Fischer, S. Forget, S. Chénais, M. Castex, D. Adès, A. Siove, B. Geffroy, *Appl.Phys.Lett.* **2006**, *89,* 183513.
2) J. Huang, G. Li, E. Wu, Q. Xu, Y. Yang, *Adv. Mater.* **2006**, *18*, 114–117.

27. 1) Y. Ohmori, H. Kajii, T. Taneda, M. Kaneko, T. Fujiki, K. Takahashi, *Mat. Res. Soc.*

Symp. Proc. **2003,** 736.
2) *J. Photopolym. Sci. Technol.* **2002**, *15*, 271.
3) Y. Ohmori, H. Kajii, M. Kaneko, K. Yoshino, M. Ozaki, A. Fujii, M. Hikita, H. Takenaka, T. Taneda, *IEEE.* **2004**, *10*, 70.
4) H. Kanno, Y. Hamada, H. Takahashi, *IEEE.* **2004**, *10*, 30.

28. H. Aziza, Z. D. Popovic, *Appl. Phys. Lett.* **2002**. *80*, 12.

29. T. Tsujioka, Y. Hamada, H. Takahashi, *Jpn. J. Appl. Phys.* **2000**, *39*, 3463.

30. F. Gutmann, L. E. Lyons, *Organic Semiconductors*; John Wiley & Sons, Inc, 1967.

31. H. Aziz, Z.D. Popovic, S. Xie, A.-M. Hor, N.-X. Hu, C. Tripp, G. Xu, *Appl. Phys. Lett.* **1998**, *72*, 756.

32. 1) S. Kim, K. Kim, Y. Tak, J. Leea, *Appl. Phys. Lett.* 2006, *89*, 132108.
2) E. M. Han, L. M. Do, N. Yamamoto, M. Fujihira, *Thin Solid Films* **1996**, *273*, 202.

33. L. S. Hung, C. H. Chen, *Mater. Sci. and Eng.* **2002**, *39*, 143.

34. S. Forrest, *Chem. Rev.* **1997**, *97*, 1793.

35. G. Burger, E. Smulders, J. Berenschot, T. Lammerink, J. Fluitman, S. Imai, *The 8th International Conference on Solid-State Sensors and Actuators, and Eurosensors IX.* **1995**, 573.

36. 1) J. Lee, S. Lee, *Adv. Mater.* **2004**, *16*, 51.
2) M. Kröger, M. Hüske, T. Dobbertin, J. Meyer, W. Kowalsky, *Mater. Res. Soc. Symp. Proc.* **2005**, *870E*, H3.4.1.

37. Retrieved from a lecture, C. Lee, Seoul National University.

38. 1) T. Hebner, C. Wu, D. Marcy, M. Lu, J. Sturum, *Appl. Phys. Lett.* **1998**, *72*, 519.
2) H. Sirringhaus, T. Kawase, R. H. Friend, T. Shimoda, , W. Wu, E. P. Woo, *Science* **2000**, *290*, 2123.

3) T. Shimoda, K. Morii, S. Seki, H. Kiguchi, *Mater. Res. Soc. Bull.* **2003**, *28*, 821.

39. P. Kao, S. Chu, C. Zhan, L. Hsu, W. Liao, *J. Vac. Sci. Techno.l* **2006**, *24*, 1278.

40. 1) Z. Bao, Y. Feng, A. Dodabalapur, B. R. Raju, A. Lovinger, *Chem. Mater.* **1997**, *9*, 1299.
2) K. Mori, T. Ning, M. Ichikawa, T. Koyama, Y. Taniguchi, *Jpn. J. Appl. Phys.* **2000**, *39*, 942.
3) G. E. Jabbour, R. Radspinner, N. Peyghambarian, *IEEE.* **2001**, *7*, 769.

41. Retrieved from a lecture, C. Lee, Seoul National University, Samsung SDI, 3M, Kodak, Philips.

42. 1) A. Fiore, J. X. Chen, M. Ilegems, *Appl. Phys. Lett.* **2002**, *81*, 1756.
2) N. Iyengar, B. Harrison,l R. S. Duran, J. R. Reynolds, *Macromolecules* **2003**, *36*, 8978.
3) L. S. C. Pingree, M. T. Russell, B. J. Scott, M. C. Hersam, *Org. Elec.* **2007**, *8*, 465.
4) F. Boroumand, P. Fry, D. Lidzey, *Nano Lett.* **2005,** *5*, 67.
5) H. Yamamoto, J. Wilkinson, J. Long, K. Bussman, Z. Kafafi, *Nano Lett.* **2005**, *5*, 2485.
6) S. Price, J. Henzie, T. Odom, *Small* **2007**, *3*, 372.
7) J. Veinot, H. Yan, S.M.Smith, J.Cui, Q.L.Huang, T.J.Marks, *Nano Lett.* **2002**, *2*, 333.
8) N. Suganuman, C. Adachi, T. Koyama, Y. Yaniguchi, *Appl. Phys. Lett.* **1999**, *74*, 1206.

43. 1) C. Cheng, F. Hong, *J. J of Appl. Phys.* **2006**, *45*, 8915.
2) Y. Koide, Q. Wang, J. Cui, D. Benson, T. Marks, *J. Am. Chem. Soc.* **2000**, *122*, 11266.
3) X. Cheng, Y. Hong, J. Kanicki, L. Guo, *J. Vac. Sci. Technol. B* 2002, *20*, 2877.
4) C. Kim, P. Burrows, S. Forrest, *Science* **2000**, *288*, 831.
5) Y. Koide, Q. Wang, J. Cui, D.Benson, T.Marks, *J. Am. Chem. Soc.* **2000,** *122,* 11266.
6) C. Kim, S. Forrest, *Adv. Mater.* **2003**, *15*, 541.
7) P. Kao, S. Chu, W. Liao, M. Hon, *IEEE.* **2005**, *52*, 1722.

44. 1) Graham P. Collins, *Sci. American,* **2004**, 76.
2) W. Brutting, *Physics of Organic Semiconductors*; Wiley-VCH, 2005.

45. 1) J. Jacobsen, J. C. Fan, S. Pombo, M. Zavracky, R, Bumgardner, *US Patent 6545654*, 2003.
2) W. E. Howard, O. F. Prache, *IBM J. RES. & DEV.* **2001**, *45*, 115.
3) I. Underwood, G. Kelly, R. Woodburn, *IEEE*. **2006**, 438.

46. W. E. Howard, O. F. Prache, IBM *J. Res. Dev.* **2001**, *45*, 115.

47. Retrieved from Kaiser Electro-Optics, US Army, Philips Research, Minority report.

48. 1) W. E. Howard, O. F. Prache, *IBM J. Res.Dev.* **2001**, *45*, 115.
2) A. Lee, P. J. B. Burke, J. P. Brody, *Proc. SPIE-Int. Soc. Opt. Eng.* **2004**, *13*, 5331.

49. 1) A. Fiore, J. X. Chen, M. Ilegems, *Appl. Phys. Lett.* **2002**, *81*, 1756.
2) N. Iyengar, B. Harrison,l R. S. Duran, J. R. Reynolds, *Macromolecules* **2003**, *36*, 8978.
3) L. S. C. Pingree, M. T. Russell, B. J. Scott, M. C. Hersam, *Org. Elec.* **2007**, *8*, 465.

50. 1) Z. Yuan, B. E. Kardynal, R. M. Stevenson, A. J. Shields, M. Pepper, *Science* **2002**, *295*, 102.
2) A. D. Sheehan, J. Quinn, S. Daly, P. Dillon, R. Kennedy, *Anal. Lett.* **2003**, *36*, 511.
3) B. D. Terris, H. J. Mamin, D. Rugar, *Appl. Phys. Lett.* **1996**, *68*, 141.
4) M. Ohtsu, K. Kobayashi, T. Yatsui, *IEEE, J. Select. Top. Quantum Electron.* **2002**, *8*, 839.

51. 1) X. H. Qiu, G. V. Nazin, W. Ho *Science* **2003**, *299*, 542.
2) Z.C. Dong, X.-L. Guo, A. S. Trifonov, P. S. Dorozhkin, S. Yokoyama, S. Mashiko, *Phys. Re*V. *Lett*. **2004**, *92*, 086801.

52. 1) A.Fiore, J.X.Chen, M.Ilegems, *Appl. Phys. Lett.* **2002**, *81*, 1756.
2) N.Iyengar, B. Harrison,l R.S. Duran, J.R.Reynolds, *Macromolecules* **2003**, *36*, 8978.
3) L.S.C.Pingree, M.T.Russell, B.J.Scott, M.C.Hersam, *Org. Elec.* **2007**, *8*, 465.

53. 1) T. Mori, K. Obata, K. Miyachi, T. Mizutani, Y. Kawakami, *Jpn. J. Appl. Phys.* **1997**, *36*, 7239.
2) G. Gu, P. E. Burrows, S. Vankatesh, S. R. Forrest, M. E. Thompson, *Opt. Lett.* **1997**, *22*, 172.
3) V. E. Chong, Y. Park, M. G. Mason, C. W. Tang, *J. Vac. Sci. Technol. A.* **1998**, *16*, 1838.
4) S.T. Lee, X.T. Hou, M.G. Mason, C.W. Tang, *Appl. Phys. Lett.* **1998**, *72*, 1593.

54. 1) I. Kymissis, S. Purushothaman, *IEEE Trans. Electron Devices* **2001**, *48*, 1060.
2) D. J. Gundlach, L. L. Jia, T. N. Jackson, *IEEE Electron Device Lett.* **2001**, *22*, 571.

55. Z. Bao, Y. Feng, A. Dodabalapur, B. R. Raju, A. Lovinger, *Chem. Mater.* **1997**, *9*, 1299.

56. A. C. Arias, S. E. Ready, R. Lujan, Y. Wu, P. Liu, B. ong, *Appl. Phys. Lett.* **2004**, *85*, 3304.

57. 1) Y. Xia, M. Mrksich, E. Kim, G. M. Whitesides, *J. Am Chem, Soc.* **1995**, *117*, 9576.
2) N. Jeon, K. Finnie, K. Branshaw, R. G. Nuzzo, *Langmuir* **1997**, *13*, 3382.
3) Y. Xia, G. M. Whitesides, *Angew. Chem. Int. Ed.* **1998**, *37*, 550.
4) S. K. Park, Y. H. Kim, D. G. Moon, W. K. Kim, *IEEE Trans. Electron Dev.* **2002**, *49*, 2008.
5) M. Geissler, A. Bernard, B. Michel, E. Delamarche, *J. Am. Chem. Soc.* **2000**, *122*, 6303.
6) H. Ko, S. Peleshanko, V. Tsukruk, *J. Phys. Chem. B* **2004**, *108*, 4385.
7) H. Ko, C. Jiang, V. Tsukruk, *Chem. Mater.* **2005**, *17*, 5489.

58. 1) E. Kim, Y. Xia, G. M. Whitesides, *J. Am. Chem. Soc.* **1996**, *118*, 5722.
2) Y. Xia, E. Kim, G. M. Whitesides, *Chem. Mater.* **1996**, *8*, 1558.
3) A. Salleo, W. S. Wong, K. E. Paul, R. A. Street, *Adv. Funct. Mater.* **2005**, *15*, 1105.

59. 1) X. M. Zhao, S. P. Smith, S. J. Waldman, G. M. Whitesides, *Appl. Phys. Lett.* **1997**, *71*, 1017.
2) R. Parashkov, E. Becker, T. Riedl, W. Kowalsky, *Adv. Mater.* **2005**, *17*, 1523.

60. S. Y. Chou, P. R. Krauss, P. J. Renstrom, *J. Vac. Sci. Technol. B*, **1996**, *14*, 4129.

61. C. A. Bulthaup, E. J. Wilhelm, B. A. Ridley, J. M Jacobson, *Appl. Phys. Lett.* **2001**, *79*, 1525.

62. J. A. Rogers, Z. Bao, A. Makhija, P. Braun, *Adv. Mater.* **1999**, *11*, 741.

63. 1) J. Collet, O. Tharaud, A. Chapoton, D. Vuillaume, *Appl. Phys. Lett.* **2000**, *767*, 1941.
2) A. D. Austin, S. Y. Chou, *Appl. Phys. Lett.* **2002**, *81*, 4431.
3) J. A. Rogers, A. Dodabalapur, Z. Bao, H. E. Katz, *Appl. Phys. Lett.* **1999**, *75*, 1010.

64. G. Horowitz, *Adv. Mater.* **1998**, *10*, 365.

65. C.D. Dimitrakopoulos, P.R.L. Malenfant, *Adv. Mater.* **2002**, *14*, 99.

66. D. Fichou, *J. Mater. Chem.* **2000**, *10*, 571.

67. C.D. Dimitrakopoulos, P.R.L. Malenfant, *Adv. Mater.* **2002**, *14*, 99.

68. C. R. Newman, C. D. Frisbie, D. A. Filho, J. Bre´das, P. C. Ewbank, K. R. Mann, *Chem. Mater.* **2004,** *16,* 4436.

69. R. B. Campbell, J. M. Robertson, J. Trotter, *Acta Cryst.* **1962**, *15*, 289.

70. M. Pope, C. Swenberg, *Electronic Processes in Organic Crystals*; Oxford: Clarendon Press, 1982.

71. D. Holmes, S. Kumaraswamy, A. Matzger, P. Vollhardt, *Chem. Eur. J.* **1999**, *5*, 3399.

72. C. Mattheus, *Polymorphism and electronic properties of pentacene*, Ph.D. Thesis, University of Groningen, 2002.

73. H. Mu, H. Shen, D. Klotzkin, *Solid State Elec.* **2004**, *48*, 2085.

74. 1) P. Gennes, F. Brochard-Wyart, D. Quéré. *Capillary and Wetting Phenomena- Drops, Bubbles, Pearls, Waves*; Springer, 2002.
2) J. J. Bikerman, *Physical Surfaces*; Academic press, 1970.
3) M. J. Jaycock, G. D. Parfitt, *Chemistry of Interfaces*; John Wiley & Sons INC. 1981.
4) K. S. Birdi, D. T. Vu, A. Winter, *Colloid & Polymer Sci.***1988**, *266*, 9.

75. 1) N. K. Adam, *The Physics and Chemistry of Surfaces*; Eotvos. 1886.
2) G. J. Janz, *NSRDS-NBS 28, report, Natl. Bur. Standards*; Washington, 1969.
3) J. J. Jasper, *J. Phys. Chem. Ref. Data.* **1972**, *4*, 841.
4) L. J. Chen, Y. H. Tsai, C. Liu, D. Chiou, M. Yeh, *Chem. Phy. Lett.* **2001**, *5*, 241.

76. 1) V. Bulovic, P.Tian, P. E. Burrows, S. R. Forrest, M. E. Thompson, *Appl. Phys. Lett.* **1997**, *70*, 2954.
2) P. Shakya1, P. Desai1, R. Curry, W. Gillin1, *Appl. Phys. Lett.* **2008**, *41*, 085108.
3) C. W. Tang, S. A. VanSlyke, *Appl. Phys. Lett,* **1987**, *51*, 913.
4) G. Gu, V. Bulovic´, P. E. Burrows, and S. R. Forrest, *Appl. Phys. Lett.* **1996**, *68*, 2606.
5) K. Yamada, K. Tamano, T. Mori, T. Mimtani, M. Sugiyama, *Proceedings of the 7th lntemational Conference on Properties and Applications of Dielectric Materials*, 2003.
6) W. Li, R. A. Jones, S. C. Allen, J. C. Heikenfeld, A. J. Steckl, *J. Disp. Tech.* **2006**, *2*, 143.
7) W. H. Kim, A. J. Ma¨kinen, N. Nikolov, R. Shashidhar, H. Kim, Z. H. Kafafi, *Appl. Phys. Lett.* **2002**, *80*, 3844.
8) S. K. Kim, D. H. Chun, H. S. Oh, H. D. Lee, K. U. Jang, M. J. Song, T. W. Kim, *Proceedings of the 7th Intemational Conference on Properties and Applications of Dielectric Materials*, 2003, 733.

77. 1) H. Mu, W. Li, R. Jones, A. Steckl, D. Klotzkin, *J. Luminescence* **2006**, 1.
2) L. S. Hung, C. W. Tang, M. G. Mason, *Appl. Phys. Lett.* **1997**, *70*, 152.
3) G. E. Jabbour, Y. Kawabe, S. E. Shaheen, J. F. Wang, M. M. Morrell, B. Kippelen, N. Peyghambarian, *Appl. Phys. Lett.* **1997**, *71***,** 1762.
4) S. Kim, D. Chung, H. Oh, H. Lee, K. Jang, M. Song, T. Kim, *Proceedings of the 7th International Conference*, 2003, 733.

5) G. Wang, X. Tao, W. Chen, Mater. *Res. Soc. Symp. Proc.* **2006**, *916*, 913.
6) D. H. Chung, S. W. Hur, S. K. Kim, J. U. Lee, C. H. Kim, J. W. Hong, T. W. Kim, *Current Applied Physics* **2004**, *4*, 667.
7) I. Huang, Z. Xie, K. Yang, C. Li, S. Liu, Y. Li, Y. Wang, J. Shen, *Opt. Quant. Elec.* **1999**, *31*, 1227.

78. N. Suganuman, C. Adachi, T. Koyama, Y. Yaniguchi, *Appl. Phys. Lett.* **1999**, *74*, 1206.

79. V. Bulovic, P. Tian, P. E. Burrows, M. R. Gokhale, S. R. Forrest, *Appl. Phys. Lett.* **1997**, *70*, 2954.

80. Z. Wu, S. Chen, H. Yang, Y. Zhao, J. Hou, S. Liu, *Semicond. Sci. Technol.* **2004**, *19*, 1138.

81. C. Chen, P. Hsieh, H. Chiang, C. Lin, H. Wu, C. Wu, *Appl. Phys. Lett.* **2003**, *83*, 5127.

82. G. Gu, V. Bulovic, P. E. Burrows, S. R. Forrest, *Appl. Phys. Lett.* **1996**, *68*, 2606.

83. B. J. Chen, X. W. Sun, S. C. Tan, *Opt. Exp.* **2005**, *13*, 937.

84. T. M. Brown, J. S. Kim, R. H. Friend, and F. Cacialli, R. Daik and W. J. Feast, *Appl. Phys. Lett.* **1999**, *75*, 1679.

85. 1) E. Garnett, D. Ginley, U.S. *Department of Energy Journal of Undergraduate Research*, 24.
2) L.A.A. Pettersson, F. Carlsson, O. Inganas, H. Arwin, *Thin Solid Films* **1998**, *313,* 356.

86. T. Yang, F. Juang, Y. Tsai, W. Kuo, M. Yokoyama, *Jpn. J. Appl. Phys.* **2006**, *45*, 3729.

87. G. Gu, D. Z. Garbuzov, P. E. Burrows, S. Venkatesh, S.R. Forrest, M. E. Thompson, *Opt. Lett.* **1997**, *22*, 396.

88. Y. Sun, S.R. Forrest, *nature photonic,* **2008**, *2*, 483.

89. C. Reese, Z. Bao, *Materials Today* **2007**, *10*, 20.

90. Z. Otwinowski, W. Minor, *Methods Enzymol.* **1997**, *276*, 307.

91. SIR97 (Release 1.02) - A program for automatic solution and refinement of crystal structure. A. Altomare, M.C. Burla, M. Camalli, G. Cascarano, C. Giacovazzo, A. Guagliardi, A.G. G. Moliteni, G. Polidori, and R. Spagna.

92. SHELX97 [Includes SHELXS97, SHELXL97, CIFTAB] - Sheldrick, G. M. (1997). Programs for Crystal Structure Analysis (Release 97-2). University of Göttingen, Germany.

93. R1 = $\Sigma(\| F_o | - |F_c \|) / \Sigma |F_o|$, wR2 = $[\Sigma(w(F_o^2 - F_c^2)2) / \Sigma(F_o^2)^2]^{1/2}$, and S = Goodness-of-fit on $F^2 = [\Sigma(w(F_o^2 - F_c^2)^2 / (n-p)]^{1/2}$, where n is the number of reflections and p is the number of parameters refined.

94. 1) E. Maslen, A. Fox, M. O'Keefe, *International Tables for Crystallography: Mathemetical, Physical and* Chemical Tables; Wilson, A. J. C., Ed.; Kluwer, Dordrecht, The Netherlands, Vol. C, Chapter 6, 1992; pp 476-516.
2) D. Creagh, W. McAuley, *International Tables for Crystallography: mathematical, Physical and Chemical tables*; Wilson, A. J. C., Ed.; Kluwer, Dordrecht, The Netherlands, Vol. C, Chapter 4, 1992; pp 206-222.

95. S. M. Sze, *Semiconductor Devices: Physics and Technology*, 2nd ed.; John Wiley & Sons, INC. 2002.

96. 1) T. Petrenko, O. Krylova, F. Neese1, M. Sokolowski1, *New Journal of Physics* **2009***, 11*, 015001.
2) S. Tavazzi, A. Borghesi, A. Papagni, P. Spearman, L. Silvestri, A. Yassar, A. Camposeo, M. Polo, D. Pisignano, *Phy. Rev. B* **2007**, *75*, 245416.
3) N. Sai, M. Tiago, J. Chelikowsky, F. Reboredo, *Phy Rev. B.* **2008**, *77*, 161306.

97. T. Djuric, A. Thierry, W. Grogger, Sh.M.A. Al-Baqi, H. Sitter, R. Resel, *Physica E.* **2009**, *41*, 1718.

98. 1) S. Ono, K. Miwa, S. Seki, J. Takey, *App. Phy. Lett.* **2009**, *94*, 063301.
2) T. Takahashi, T. Takenobua, J. Takeya, Y. Iwasa, *App. Phy. Lett.* **2006**, 88, 033505.
3) S. Seo, B. Park, P. G. Evansa, *App. Phy. Lett.* **2006**, *88*, 232114.

99. H.Y. Choi, S. H. Kim, J. Jang, *Adv. Mater.* **2004**, *16*, 732.

100. 1) J.A. Venables, G.D.T. Spiller, M. Hanbucken*Rep. Prog. Phys.* **1984**, *47*, 399.
2) Granasy, L., Borzsonyi, T. & Pusztai, T. *Phys. Rev. Lett.* **2002**, *88*, 206105.
3) L. Gránásy, T. Pusztai, T. Börzsönyi, G. Tóth, G. Tegze, J.A. Warren, J.F. Douglas, *J. Mater. Res*. **2006**, *21*, 309.

101. W.H. Taylor, *Z. Kristallogr.* **1936**, *93*, 151.
* Cambridge crystallographic data

102. Z.A. Akopyan, R.L. Avoyan and Yu.T. Struchkov, *Zh. Strukt. Khim.* **1962**, *3***,** 602.
* Cambridge crystallographic data

103. D. E. Henn, W. G. Williams and D. J. Gibbons, *J. Appl. Cryst.* **1971**, *4*, 256.

104. I. Bulgarovskaya, V. Vozzhennikov, S. Aleksandrov, V. Belsky *Latv.PSR Zinat. Akad. Vestis, Khim.Ser.* **1983**, 53.

105. O.D.Jurchescu, A.Meetsma, T.T.M.Palstra, *Acta Crystallogr.,Sect.B:Struct.Sci.* **2006**, *62*, 330.

106. 1) J. Lee, K. Kim, D. Park, M. Cho, Y. Lee, J. Jung, D. Kim, J. Kim, J. Joo, *Adv. Funct. Mater.* **2009**, *19*, 1.
2) E. Menard, A. Marchenko, V. Podzorov, M. E. Gershenson, D. Fichou, J. A. Rogers, *Adv. Mater.* **2006**, *18*, 1552.
3) C. H. Hsu, J. Deng, C. R. Staddon and P. H. Beton, *Appl. Phys. Lett.* **2007**, *91*, 193505.

107. C. Kloc, K.J. Tan, M.L. Toh, K.K. Zhang, Y.P. Xu, *Appl Phys A.* **2009**, *95*, 219.

108. 1) F. Bayrakceken, *J. Luminescence* **1984**, 29, 111.
2) F. Bayrakceken, B. Bans, *Spectroscopy Letters*, **1996**, *29*, 151.

109. R.M. Hochstrasser, M. Ritchie, *Trans. Faraday Soc.* **1956**, *52*, 1363.

110. 1) V. Ramamurthy, K. Venkatesan, Chem. Rev. **1987**, *87*, 433.
2) D. Ka¨ fer and G. Witte, *Phys . Chem. Chem. Phys.* **2005**, *7*, 2850.

111. 1) C. Moureu, C. Dufraisse, P.M. Dean, C. R. *Acad. Sci.* **1926**, *182*, 1440.
2) R.M. Hochstrasser, *Can. J. Chem.* **1959**, *37*, 1123.
3) R. Schmidt, H.D. Brauer, *J. Photochemistry* **1981**, *15*, 85.
4) M. Yamada, I. Ikemoto, H. Kuroda, *Bull. Chem. Soc. Jpn.* **1988**, *61*, 1057.

112. E.J. Bowen, F. Steadman, *J. Chem. Soc. London* **1934**, 1098.

113. W.G. Herkstroeter, P.B. Merkel, *J. Photochem.* **1981**, *16*, 331.

114. S. Erkoc, *J. Molecular Structure (Theochem)* **2002**, *578*, 99.

115. C. Kloc, K.J. Tan, M.L. Toh, K.K. Zhang, Y.P. Xu, *Appl Phys A.* **2009**, *95*, 219.

116. 1) O. Mitrofanov, D. V. Lang, C. Kloc, J. M. Wikberg, T. Siegrist, W. So, M. A. Sergent, A. P. Ramirez1, *Phys. Rev. Lett.* **2006**, *97*, 166601.
2) O. Mitrofaniv, C. Kloc, T. ZSiegrist, D.V. Lang, W. So, A.P. Ramirez, *Appl. Phys. Lett*. **2007**, *91*, 212106.

117. 1) M. Petty, *Molecular electronics : from principles to practice*; Wiley-Interscience, 2007.
2) M. Pope, C.E. Swenberg, *Electronic Processees in Organic Crystals and Polymers*; Oxford University Press, 1999.

118. L. Tsetseris, S.T. Pantelides, Organic Electronics **2009**, *10*, 333.

119. V. Podzorov, E. Menard, A. Borissov, V. Kiryukhin, J.A. Rogers, M.E. Gershenson, *Phys. Rev. Lett.* **2004**, *93*, 086602.

120. J. Takeya, M. Yamagishi, Y. Tominari, R. Hirahara, Y. Nakazawa, T. Nishikawa, T. Kawase, T. Shimoda, S. Ogawa, Appl. Phys. Lett. **2007**, *90*, 102120.

121. D. A. Filho, E. Kim, J. Bredas, *Adv. Mater.* **2005**, *17*, 1072.

122. 1) V. C. Sundar, J. Zaumseil, V. Podzorov, E. Menard, R. L. Willett, T. Someya, M. E. Gershenson, J. A. Rogers, *Science* **2004**, *303*, 1644.
2) R. Zeis, C. Besnard, T. Siegrist, C. Schlockermann, X. Chi, C. Kloc, *Chem. Mater.* **2006,** *18,* 244.

123. G. Schuck, S. Haas, A. Stassen, U. Berensc, B. Batloggb, *Acta Cryst.* **2007**, *E63*, 2894.

124. T. Matsukawa, Y. Takahashi, T. Tokiyama, K. Sasai, Y. Murai, N. Hirota, Y. Tominari, N. Mino, M. Yoshimura, M. Abe, J. Takeya, Y. Kitaoka, Y. Mori, S. Morita, T. Sasaki, *Jpn. J. Appl. Phys.* **2008**, *47*, 8950.

125. O. D. Jurchescu, J. Baas, T. T. M. Palstra, *Appl. Phys. Lett.,* **2004**, *84*, 3062.

126. Z. Zhang, Z. Wang, R. Xing, Y. Han, *Surface Science* **2003**, *539*, 129.

127. Y. Lin, D. Gundlach, S. Nelson, T. Jackson, *Device Letters, IEEE.* **1997**, *18*, 606.

128. L. Xue, Y. Han, *Progress in Polymer Science* **2011**, *36,* 269.

129. N. Suganuman, C. Adachi, T. Koyama, Y. Yaniguchi, *Appl. Phys. Lett.* **1999**, *74*, 1206.

130. H. Kuhn, *J. Chem. Phys.* **1970**, *53*, 101.